ELECTROWETTING-BASED MICROACTUATION OF DROPLETS FOR DIGITAL MICROFLUIDICS

by

Michael George Pollack

Department of Electrical and Computer Engineering
Duke University

Date: ______________________
Approved:

____
Richard B. Fair, Supervisor

____
Hisham Z. Massoud

____
Edward J. Shaughnessy

____
Gary A. Ybarra

____

Dissertation submitted in partial fulfillment of the
requirements for the degree of Doctor of Philosophy
in the Department of Electrical and Computer Engineering
in the Graduate School of
Duke University

2001

ABSTRACT

(Engineering—Electrical and Computer)

ELECTROWETTING-BASED MICROACTUATION OF DROPLETS FOR DIGITAL MICROFLUIDICS

by

Michael George Pollack

Department of Electrical and Computer Engineering
Duke University

Date: ______________________________
Approved:

____
Richard B. Fair, Supervisor

____
Hisham Z. Massoud

____
Edward J. Shaughnessy

____
Gary A. Ybarra

____

An abstract of a dissertation submitted in partial
fulfillment of the requirements for the degree
of Doctor of Philosophy in the Department of
Electrical and Computer Engineering in the Graduate School of
Duke University

2001

Abstract

The miniaturization and automation of chemical and biochemical laboratory instrumentation and processes has emerged as an important research topic in recent years. While numerous microfabricated fluid handling components to enable chip-based laboratories have been reported, the integration and reconfiguration of these diverse components remains a very challenging problem. Drawing upon analogies from microelectronics, this dissertation proposes an alternative organizational principle for the design, implementation and operation of complex and reconfigurable microfluidic systems. "Digital microfluidics," based upon independent manipulation of discrete units of fluid (droplets) under a set of simple and well-defined operations, offers significant advantages over conventional continuous-flow microfluidics. In order to demonstrate the feasibility of digital microfluidics, this work describes the design, fabrication and testing of a planar microactuator structure for droplet manipulation based upon the electrowetting effect. Manipulation of droplets under direct electrical control without the use of pumps, valves, or fixed channels was demonstrated for electrolyte droplets ranging in size from 3 nl – 3 μl. Average droplet velocities in excess of 10 cm/s were obtained at voltages as low as 60 V. The effect of various geometrical parameters and liquid properties on droplet transport rates was measured and analyzed. Other droplet-based operations including mixing, splitting, merging, and formation of droplets from a continuous source were also demonstrated. Thus, this technology permits monolithic integration of multiple microfluidic functions within a single chip. Important practical systems issues including droplet detection, solvent compatibility and droplet stability were also experimentally addressed in this work.

Acknowledgements

I would like to acknowledge the contributions of several persons who made this work possible. First, I would like to express my appreciation to Dr. Richard Fair for his guidance, support and vision throughout this project. I would also like to thank the other members of my committee, Dr. Hisham Massoud, Dr. Gary Ybarra, and in particular, Dr. Edward Shaughnessy for his support and encouragement. Special thanks and recognition is owed to Dr. Alex Shenderov for his fundamental and highly original contributions to this work. His involvement and collaboration was a central factor in the success of this project and a tremendous enrichment to my education. I am also grateful for the participation of Stefan Ufer and the Biomedical Microsensors Laboratory at North Carolina State University. I would also like to thank Dr. Hugh Crenshaw, Brian Dodge, Pramod Kolar, Junhua Wu, Jason Tsao and Ray Woo, all of whom contributed to aspects of this research. Finally, but not least, I would like to thank my family and friends for their patience and encouragement throughout this process.

Contents

List of Tables

List of Figures

Chapter 1

Background and Motivation

1.1 Introduction

Recent years have seen the emergence of an interdisciplinary research effort to develop miniaturized integrated chemical and biological analysis systems. Also known as microlabs, labs-on-a-chip or μ-TAS (micro total analysis systems), the ultimate goal of these systems is to reduce most common (bio)chemical laboratory procedures and equipment to miniaturized, automated chip-based formats, thereby enabling rapid, portable, inexpensive and reliable (bio)chemical instrumentation with applications in medical diagnostics, environmental monitoring, and basic scientific research. The high-throughput and dramatically reduced reagent consumption and labor requirements of microlabs also enable certain techniques which would normally be prohibitively expensive or time consuming by conventional methods. Thus, microlabs have the potential not only to enhance, but to transform many areas of science and medicine.

Microlabs crucially depend on rapid automatic manipulation of minute quantities of liquids. Micromachining technology, originally adapted from semiconductor processing techniques, has provided the means to (batch) fabricate the miniature channels and other microfluidic components required by microlabs. Numerous microfluidic components including pumps, valves, channels, flow sensors, micromixers, reaction chambers, detectors and dispensers have been demonstrated in recent years [1][2][3][4]. However, because of the diverse technologies and materials involved, integration of these components has been an extremely challenging task. Consequently, only relatively simple systems have thus far been realized, and microlabs have yet to attain their full promise.

The few successful integrated systems have been devoted to fairly simple and specialized applications. For example, Burns, Burke and Mastrangelo [4][5][6][7] developed an integrated DNA analysis device in which droplets were propelled down a single channel through a thermal reaction chamber and into an electrophoresis channel for analysis. However, the most successful integrated devices have been the capillary electrophoresis chips [8], now sold commercially by companies like Caliper Technologies. These chips use high voltages to electrokinetically transport liquid "plugs" through a network of microchannels with mixing and separations occuring at predefined points along the pathway. This technology has succeeded largely because the fabrication and integration requirements are so minimal. But as we will see, this technology is only suitable for a narrow class of applications.

Since it appears that there are no monolithic integrated solutions for microlabs on the horizon, attention has been largely focused on technologies for interconnecting discrete microfabricated fluidic components. Thus, some have proposed a vertically stacked assembly with components on each level communicating through a set of common manifolds [9]. Others have proposed a planar breadboard or circuit-board concept where functional modules are "plugged in" to a planar substrate that provides electrical and fluidic connections between the components [10][11]. Another alternative, conceptionally similar to a multichip module, involves direct connections between sets of discrete components [12][13]. However, none of these approaches has yet produced a flexible and workable system capable of addressing a reasonably wide range of problems.

We propose a new system integration and organization concept for the realization of more complex, flexible, and powerful microfluidic systems. Recognizing the advantages of the digital design approach in microelectronics, we propose to implement a microfluidic technology based upon the manipulation and control of discrete fluid units. In the remainder of this chapter we hope to demonstrate that "digital microfluidic" systems potentially possess many of the same advantages that make the design and operation of digital electronic systems so flexible, robust and powerful. However, after examining the state-of-the-art in microfluidic technologies we will find that new microactuation principles are needed for the implementation of these systems. Surface tension based methods, in particular, are favored as they exploit both micro-domain scaling laws and unique characteristics of digital microfluidic systems. Direct electrical control of surface tension, a phenomenon known as electrowetting, provides the actuation force for our proposed technology.

In Chapter 2 we consider the design and operation of microactuators based upon the electrowetting effect. We consider several alternative microactuators and establish basic guidelines for their design and implementation. In Chapter 3 we describe the fabrication processes and materials design issues associated with this technology. These issues were found to be more challenging than we had initially anticipated. Chapter 4 presents an experimental study of droplet transport which is the fundamental operation of the digital microfluidic architecture. We arrive at an understanding of the factors affecting droplet transport speeds and the scaling behavior of the transport phenomenon. However, practical systems cannot be built upon droplet transport alone. Thus, in Chapter 5 we experimentally address the most important problems for the design and implementation of simple functional architectures. These issues include dropet generation (fluid discretization) and detection as well as droplet stability and solvent compatibility issues. In Chapter 6 we consider possible directions for future work in both digital microfluidics and electrowetting-based microactuation. Although we do not attempt to implement or demonstrate any particular architecture or application we hope that this work provides a foundation for the development of such systems in the future.

1.2 Digital Microfluidics

At present, most microfluidic technologies are based upon continuous flow of liquid through microfabricated glass or plastic channels. Pumping is performed either by external pressure sources, integrated mechanical micropumps or by electrokinetic mechanisms. These systems are often operated in a serial mode where sample reagents are loaded into one end, and then move together towards an output at the other end with mixing, sample injection, and separations occuring at (structurally) predetermined points along the path. These systems are adequate for many well-defined and simple applications, but are unsuited for more complex tasks requiring a high degree of flexibility or complicated fluid manipulations.

Continuous-flow systems are inherently difficult to integrate because the parameters which govern the flow field (e.g. pressure, fluid resistance, electric field) vary along the flow-path making the flow at any one location dependent upon the properties of the entire system. As liquids mix and react in the system their electrical and hydrodynamic properties change, resulting in even more complicated behavior. Consequently, the design and analysis of even moderately complex systems can be very challenging. Furthermore, since structure and function are so tightly coupled, each system is only appropriate for a narrow class of applications.

The division of fluid into discrete, independently controllable packets or droplets for manipulation, provides several important advantages over continuous-flow. The reduction of microfluidics to a set of basic repeated operations (i.e. “move one unit of fluid one distance unit”) allows a hierarchical and cell-based design approach to be utilized. Large systems may be constructed out of repeated instances of a single well-characterized device in the same way that complex microelectronic circuits may be built upon a single well-characterized transistor. Thus, the design and analysis of arbitrarily complex microfluidic systems becomes tractable. The constituent cells may be reorganized at different hierarchical levels, either through hardware or software, to provide new functionality on demand. Digital microfluidic systems, therefore, are not only flexible and scalable, but *reconfigurable* as well.

1.2.1 Digital Microfluidic Architecture

We consider first some aspects of a simple example digital microfluidic architecture and compare the implementation of certain functions to conventional continuous-flow microfluidic systems. A simple digital microfluidic architecture is illustrated in Figure 1.1. At the core of the architecture is an array of identical "transport" cells each capable of storing a single unit of fluid or transferring it to any adjacent cell. We assume that liquid may be transferred between any two adjacent transport cells at a rate which is independent of the location of the cells as well as the direction of fluid movement. At the periphery are "functional" cells which perform specialized operations such as input/output, mixing, thermocycling or separation/detection. Pathways or "virtual channels" between functional cells are established through real-time reconfiguration of transport cells, thus allowing highly flexible and efficient use of system resources.

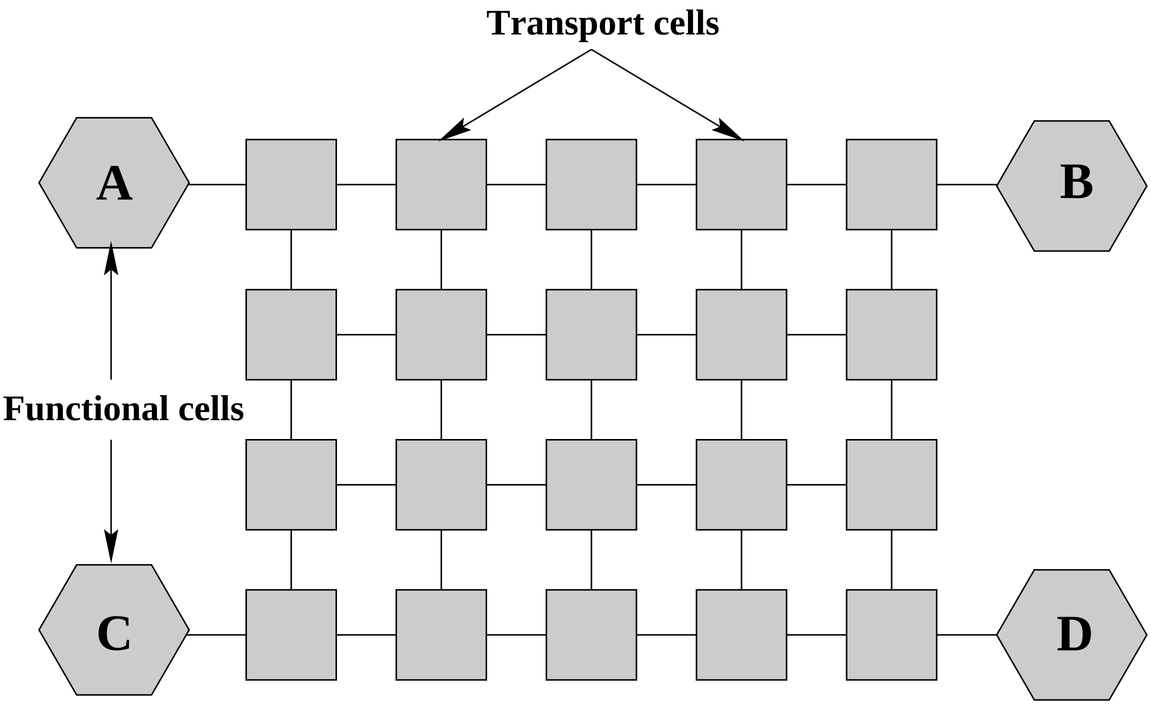

Figure 1.1: Simple digital microfluidic system architecture

Consider the simple case of fluid transport between two functional cells in Figure 1.1. Fluid transport requires successive discrete transfers between adjacent cells and the average flow-rate Φ (assuming perfect transfer efficiency) is

$$\Phi = V_D f \tag{1.1}$$

where V_D is the discrete fluid volume and f is the transfer frequency. Thus, the average flow-rate is linearly proportional to the clock frequency and can be precisely controlled over a large dynamic range.[1] The flow-rate is also independent of the properties of the fluid so long as f is slower than the maximum transfer rate of the "slowest" liquid in the system.

For comparison, simulated continuous flow-rate versus frequency curves for an electrostatically-actuated membrane micropump are shown in Figure 1.2. It can be seen that the relationship between actuation frequency and flow-rate is nonlinear and highly dependent upon the fluid

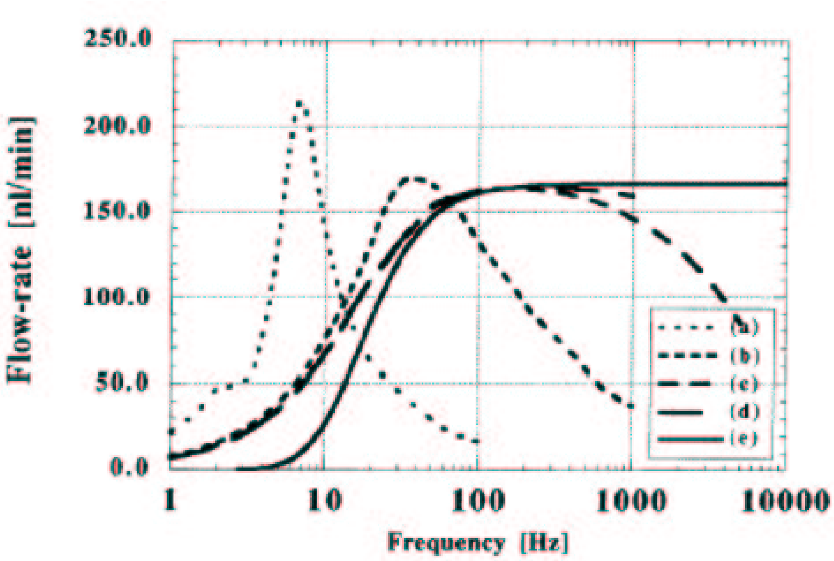

Figure 1.2: Simulated flow-rate versus actuation frequency of an electrostatic membrane micropump. Each curve represents a different value of fluid density: (a) 72 g/cm^3 (b) 3 g/cm^3 (c) 0.1 g/cm^3 (d) 0.001 g/cm^3. From [14]

---

[1] Subject to "discretization" error or noise, the consequences of which are system and application specific.

properties. The flow is also unidirectional and controllable only over a fairly narrow dynamic range. Additionally, the flow-rate of the micropump depends on the back-pressure at the micropump inlet which in turn depends on the other pumps, valves and channels within the network making the design and analysis of these systems quite complex. Similarly, in electrokinetic systems, the flow-rate depends on the shape and length of the individual channels as well as the voltage and conductivity of the liquid. Because the flow-rate in continuous-flow systems depends on the length and geometry (hydraulic resistance) of the flow-path, reconfiguation requires recalibration and possibly redesign of multiple system components.

In addition to controlling the rate of flow, microfluidic systems must also be able to switch liquid flows. In continuous-flow systems switching is accomplished either by integrated microvalves or by control of an external sources (pressure or voltage). Since an uninterrupted flow path must be established between the source and destination, the topography imposes severe constraints on the number of fluids that can be simultaneously handled without intersection or mixing occurring. In electrokinetic systems, current must pass throughout the length of the flow-path resulting in substantial Ohmic heating of the solution. Continuous-flow systems also require that the entire flow-path be filled with liquid and energized regardless of how little volume is to be transferred.

By contrast, digital microfluidic systems perform switching at the fluid packet level. Small discrete volumes of fluid can be transferred between any two points regardless of their relative position or separation and multiple fluids can be simultaneously transported in a single flow channel. Intersecting flow paths (e.g. from A to D and from C to B in Figure 1.1) can easily be implemented through proper control of timing, and transport capacity can be instantaneously reallocated depending on flow requirements. Portions of channels may also serve as temporary buffers or reservoirs for liquid while other portions remain free for transport. Thus, the movement of fluid resembles not so much a plumbing system as perhaps the flow of data across a digital network.

1.2.2 Implementation of Digital Microfluidics

Having considered some features and potential advantages of digital microfluidic systems, we now consider how such systems might by physically implemented. Conceivably, such architectures could be realized using the same components as are used in conventional continuous-flow systems. However, as we previously noted, the problem of integrating or interconnecting these diverse components has not been satisfactorily resolved. Mechanical microvalves in particular pose a problem due to their large size, large power requirements, large dead volumes, expensive and complex fabrication, and poor performance and reliability. Thus a digital microfluidic architecture requiring as many as four valves per cell, probably cannot be realized in this manner. Electrokinetic systems operate without mechanical valves, but are fundamentally unsuited for digital microfluidics because they provide only limited capability for *independent* control of multiple fluid volumes. The ideal technology for digital microfluidics would allow fluid pumping to be distributed throughout the network. In this manner pressure could be applied only where and when it is needed to permit independent control of multiple fluid units.

One such technology employs *in situ* generation of air bubbles by electrolysis or thermal heating for pumping and valving [15][16][17]. This technology is promising for digital microfluidics because it requires no moving parts and is relatively easy to integrate, the actuators being simple metal electrodes or polysilicon heaters. A sample bubble microfluidic system employing 37 bubble pumps and 48 bubble valves is shown in Figure 1.3. Since pressure can be generated locally at the site of bubble generation, distributed pumping and independent control of fluid is a possibility. However, the requirement to electrolyze or vaporize the fluid may lead to contamination or loss of sample and be incompatible especially with biological solutions.

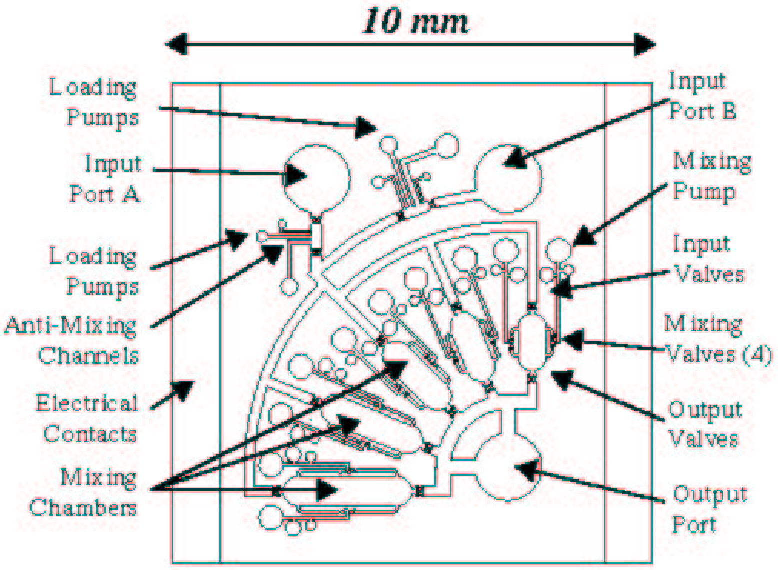

Figure 1.3: Chip layout of a microfluidic system utilizing thermally generated bubbles for pumping and valving. From [16]

An alternative implementation strategy is suggested by the discretized nature of the liquid itself. Discretization of the liquid permits the existence of free surfaces constrained by surface tension. Digital microfluidics, therefore, may involve forces which are not normally relevant to continuous-flow technologies. Where it exists, surface tension is often the dominant force acting in systems at these length scales. It has been speculated that “if human beings were creatures of sub-millimeter in size, the main force of interest to us would have been surface tension, many machines would be driven by surface-tension-based motors, while inertia would be just an interesting but unimportant force” [18]. In continuous-flow systems surface tension usually appears as an unwelcome force which resists the filling of channels or dislodgement of air bubbles. However, given its relative strength and favorable scaling properties, surface tension should also be viewed as a target for microactuation at these length scales. We propose to use active control or modulation of surface tension as a microactuation and fluid control principle for digital microfluidic systems.

1.3 Surface Tension Driven Flow

It has long been known that surface tension gradients are capable of producing bulk flow of liquid films or droplets. Perhaps the oldest and and most often cited example is the “tears of wine” effect where wine droplets are spontaneously driven along the surface of a wineglass due to surface tension instabilities arising from the evaporation of alcohol [19]. Such flows arising from chemically or thermally induced surface tension gradients within a liquid meniscus are known as Marangoni flows and are important in many industrial processes [20]. The Marangoni effect is principally a surface flow with bulk flow being a secondary consequence. However, it is also possible to use surface tension gradients to directly drive the bulk flow of liquid droplets on solid surfaces and within channels.

1.3.1 Actuation Principles

We first consider the forces acting on a liquid droplet resting on a non-wetting solid surface in the absence of gravity. The forces at the solid-liquid-vapor interface are described by *Young’s equation* in which the surface energies of each of the three interfaces are represented by surface tensions acting along their associated surfaces (Figure 1.4). At equilibrium the forces are balanced and the contact angle θ between the droplet and solid is determined by the three interfacial tensions

$$\gamma_{LV} \cos\theta = \gamma_{SV} - \gamma_{SL} \tag{1.2}$$

where γ_{LV}, γ_{SV} and γ_{SL} are the liquid-vapor, solid-vapor and solid-liquid surface energies respectively.[2]

---

[2] The vapor phase could just as well be a second immiscible liquid phase, even if this fact is not always reflected in our choice of subscripts.

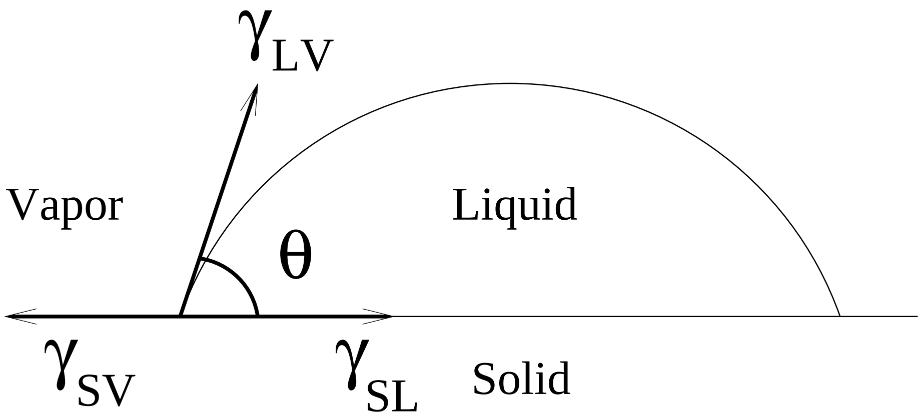

Figure 1.4: Cross-section of equilibrium forces acting on one side of a non-wetting droplet in contact with a horizontal solid surface

If we now consider the case where $\cos\theta$ is positive and a small capillary of radius r, open at both ends, is placed in a pool of liquid exposed to the atmosphere, we see the phenomenon of capillary rise. The liquid rises up the capillary reducing the lower energy solid-vapor interfacial area while increasing the higher energy solid-liquid interfacial area. If the liquid rises a distance h, then the total energy reduction is $(\gamma_{SV} - \gamma_{SL})2\pi rh$. This is balanced by the work done to raise the column of liquid which is $\Delta P \pi r^2 h$, where ΔP is the pressure difference between the ends of the column. Equating the energies gives

$$\Delta P = \frac{2(\gamma_{SV} - \gamma_{SL})}{r} = \frac{2\gamma_{LV}\cos\theta}{r} \tag{1.3}$$

which is an important special form of the *Young-Laplace equation*.[3] The general form gives the fluid pressure across an arbitrarily curved surface

$$\Delta P = \gamma \left(\frac{1}{R_1} + \frac{1}{R_2} \right) \tag{1.4}$$

where γ is the surface tension, and R_1 and R_2 are the principal radii of curvature of the surface. Together, *Young's equation* and the *Young-Laplace equation* constitute the basic equations of surface tension and capillary phenomena.

---

[3] Also called *Laplace's Law*.

When a droplet is in contact with a surface having a gradient of surface energy as shown in Figure 1.5a, a net force arises between the ends of the droplet due to the out-of-balance surface tension forces acting along the contact line. This net force may induce bulk flow of the droplet. One of the earliest and most straightforward demonstrations of this principle was provided by Chaudhury and Whitesides [19]. They exposed a silicon wafer to a diffusing front of decyltrichlorosilane vapor to produce a smooth gradient of surface energy. When droplets of water were placed at the more hydrophobic end of the wafer inclined 15° from horizontal, they moved uphill towards the hydrophilic end at a

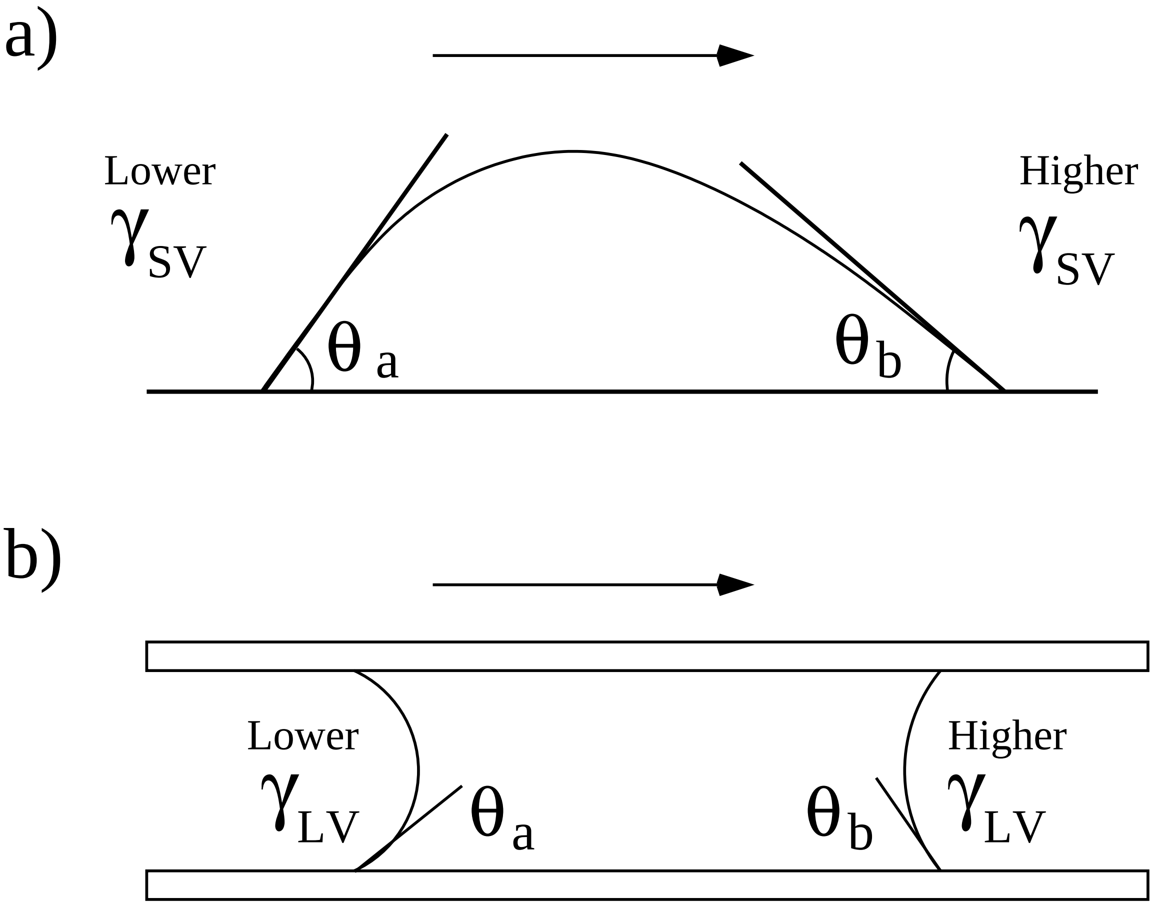

Figure 1.5: (a) Cross-section of a droplet resting on a surface having a gradient of surface energy (b) cross-section of a droplet in a capillary with menisci of different surface energies. Both droplet shapes are exaggerated to show the equilibrium contact angles on each side. The arrows indicates the direction of motion.

rate of 1 – 2 mm/s. Similarly, when droplets are confined within a capillary or channel as shown in Figure 1.5b a gradient of liquid-vapor interfacial energy may produce a net force on the droplet. For a circular capillary, the net force is easily calculated by application of Equation 1.3 to both ends of the droplet.

However, the presence of a surface tension gradient alone is not sufficient to induce motion of the droplets if significant hysteresis in contact angles is present. Contact angle hysteresis is essentially the observation that real contact lines are characterized not by a single equilibrium contact angle, but by a range of values [21][22]. A recently advanced contact line exhibits a higher contact angle θ_A than a recently receded one with contact angle θ_R. At equilibrium the contact angle may assume any value between these limits without disturbing the position of the contact line. Thus, some additional force is required to initiate and sustain the motion of the droplet. An everyday example of this phenomenon is a raindrop attached to a vertical window, where the difference in angles between the ends of the droplet creates a force that opposes the downward motion due to gravity. At present, the origins of contact angle hysteresis are poorly understood, but it is clearly associated with roughness and heterogeneity of the surface.

1.3.2 Active Control of Interfacial Tension

Actuation of droplets by surface tension force requires a means to actively control at least one of the interfacial energies in the system. Ideally, manipulation of interfacial energy should be performed rapidly and reversibly through an easily controlled physical variable. This variable may be chemical, thermal or electrical in nature (see [23] for a recent review).

Chemical Methods

An electrochemical method has been demonstrated by Gallardo *et al.* [24]. They employed redox-active surfactants to generate a surface tension gradient along a channel. Surfactant was oxidized at one electrode and reduced at another to produce a concentration gradient capable of driving liquid droplets through a simple fluidic network. Moderate velocities of 2.5 mm/s were obtained at low voltages (< 1 V). However, the technique appears to be limited to non-aqueous liquids which are insoluble in the electrolyte bathing solution. Since the electrochemical gradient must be established along the full length of the channel, this technique, like electrokinetic methods, does not provide a convenient means for independent control of multiple droplets.

Ichimura *et al.* [25] have demonstrated a photochemical method relying on asymmetrical irradiation of a photoisomerizable azobenzene surface to generate surface-energy gradients for driving the motion of liquid droplets. The use of light is attractive as it provides a convenient means to control two-dimensional movement of multiple droplets without microfabricated structures on the chip. However, the reported velocities of 50 μm/s are very slow and due to contact angle hysteresis many liquids (including water) could not be transported at all.

Thermal Methods

Methods relying on thermal effects have thus far seemed more promising than chemical-based methods. The surface tension of a liquid meniscus decreases linearly with increasing temperature. Thus differentially heating the ends of a droplet in a capillary produces a surface tension imbalance which drives droplet motion. Thermocapillary-based systems for droplet transport have been studied in detail [26][27] and have even been incorporated into a simple microfluidic DNA analysis device [5][6]. These thermocapillary systems incorporate multiple independently controlled micromachined heaters into a single microchannel bed and are thus capable of independent droplet control. The design and analysis of thermocapillary systems, however, is complex because it requires a complete heat-transfer analysis which is dependent upon many factors including substrate type, channel geometry, and fluid type and velocity [27]. Relatively high velocities of up to 20 mm/s have been obtained for certain liquids, but the required temperature gradients can be substantial. For example, it was reported that a differential of 20 – 40 °C was required simply to initiate movement of water droplets in one particular device [5]. Such temperature variations are clearly unacceptable for many potential biological applications where temperature control to 1 °C or better is often desired.

Electrical Methods

Electrical control of the interfacial tension between two liquids was first systematically studied over 125 years ago by Lippman [21]. He described the electrocapillary effect whereby the height of a mercury column in contact with an electrolyte could be controlled by a voltage applied between the two phases. However, the classical electrocapillary effect is unsuited for digital microfluidics because it requires electrification of both the droplet and surrounding medium and thus lacks the capacity for independent control of multiple droplets. The effect also requires two immiscible conductive liquid phases and thus appears to be experimentally limited to systems containing a liquid metal phase. Furthermore, the effect strongly depends on the state of the electrical double-layer at the interface which is sensitive to both the type and concentration of electrolyte in the aqueous phase.

More recently, an electrocapillary phenomenon known as continuous electrowetting (CEW) has been described [28]. In CEW a droplet of liquid metal is driven along an electrolyte filled capillary by an electric potential applied across the length of the channel. The resistance of the electrolyte in the thin gap between the droplet and capillary wall produces an electrostatic gradient which in turn establishes a surface tension gradient resulting in droplet motion. High speeds of up to 10 cm/s have been achieved in these systems and a number of interesting gadgets have been demonstrated [18][29][30]. However, for digital microfluidics CEW possesses all of the same disadvantages as classical electrocapillarity.

An electrostatic method of transporting liquid droplets on a solid surface was demonstrated by Washizu [31]. His system consisted of a series of narrow electrodes coated with a hydrophobic insulator. Electrostatic attraction between a droplet of electrolyte and an electrode just in advance of the droplet resulted in incremental droplet motion. By controlling the voltage phase of multiple electrodes continuous droplet motion was achieved. A microreactor capable of transporting, sorting and fusing 0.5 – 5.0 μl droplets of various compositions was demonstrated, although the reported velocity of 400 μm/s was relatively slow. Although this method does not appear to strictly depend on electrical control of surface tension it does share many similarities with electrowetting and may, in fact, be formally equivalent to it. Another electrostatic method was demonstrated by Sandre *et al.* [32], in which electric fields were used to deform droplets resting on asymmetrically structured (sawtoothlike) surfaces. Relaxation of the droplet following activation resulted in incremental movement of the droplet due to the local asymmetry of the surface (similar to a ratcheting effect). However, this technology seems to allow only unidirectional transport and the reported velocity of 150 μm/s is slow.

1.4 Electrowetting

Electrowetting is another electrical method, similar to, but distinct from classical electrocapillarity and CEW, which uses electric fields to directly control the interfacial energy between a solid and liquid phase. Since the polarized interface contains a solid phase rather than two liquid phases, the energy may be controlled in a more precise manner through fixed solid structures rather than through an energized liquid medium. The ability to spatially define and localize (i.e. by photolithography of electrodes) the energy gradient provides a means to independently address and manipulate multiple droplets simultaneously. This, coupled with the universal advantages of an electrically-based method, makes electrowetting a very attractive microactuation concept for digital microfluidics.

The Electrowetting Effect

Consider a conducting droplet resting on a non-wetting solid insulator of thickness d and relative dielectric constant ϵ_r as shown in Figure 1.6. If a voltage V is now applied between a wire electrode inside the droplet and a counterelectrode underneath, charge will become stored in the effective capacitor formed by the droplet and electrode. We assume that the interface is uncharged in the absence of an applied potential and that the electrostatic energy E stored in the capacitor is directly proportional to the area A of the base of the droplet. By the parallel-plate capacitor approximation we have

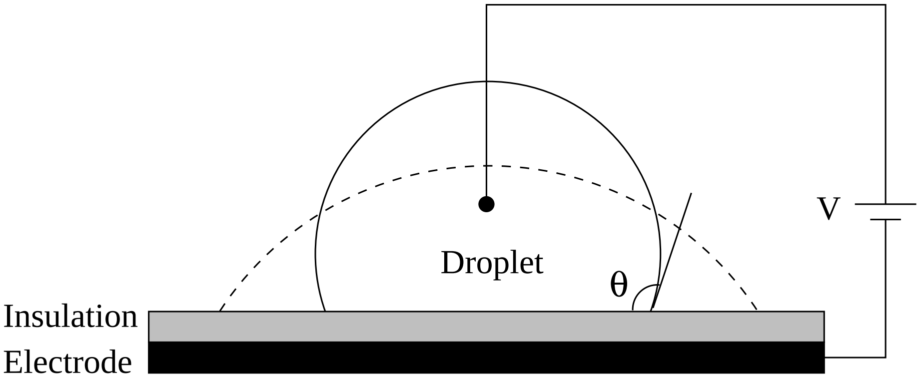

Figure 1.6: The electrowetting effect

$$E = \frac{\epsilon_0 \epsilon_r A}{2d} V^2 \tag{1.5}$$

This electrostatic energy directly modifies the solid-liquid interfacial tension γ_{SL}, so that

$$\gamma_{SL}(V) = \gamma_{SL}(0) - \frac{\epsilon_0 \epsilon_r}{2d} V^2 \tag{1.6}$$

which is essentially Lippman's equation originally derived for a mercury-electrolyte interface with charge separation across a diffuse region in the liquid rather than a solid insulator. The contact angle of the liquid with the solid is modified according to Equation 1.2 giving

$$\cos\theta(V) = \cos\theta(0) + \frac{\epsilon_0 \epsilon_r}{2d\gamma_{LV}} V^2 \tag{1.7}$$

Thus, the voltage reduces the contact angle and the droplet spreads or wets the surface. The surface effectively becomes more hydrophilic under the influence of the electric field. Theoretically, the effect should be independent of both the polarity and frequency of the effective voltage.

A Short History of Electrowetting

The earliest investigations of electrowetting occured over 60 years ago and were concerned with metal electrodes directly in contact with the electrolyte solution [21]. This was essentially an extension of classical electrocapillary experiments with a solid rather than liquid metal phase. In this case, the charge is separated across a diffuse, nanometers thick, layer within the liquid. Because of the molecular dimensions involved, the capacitance is very high, on the order of 10 μF/cm^2 and electrowetting is observed at very low (< 1 V) voltages. However, it was not until the early 1980's that classical electrowetting first attracted practical attention when it was proposed as a basis for display devices [33][34]. It was subsequently acclaimed as a microactuation principle for microelectromechanical systems (MEMS) [35][36][37]. However, these early efforts failed to produce any compelling practical applications or devices.

More recently, studies of electrowetting on solid insulators have led to a resurgence of interest in this physical phenomenon.[4] Vallet, Berge and Vovelle [39][40] achieved large, although irreversible contact angle variations on 12 μm thick polyethylene terephthalate (PET) films. The use of solid insulation permits a larger effect, because although the capacitance is much lower (nF/cm^2 – pF/cm^2), and the required voltages are much higher (up to 1000 V), higher electric fields can be withstood by the insulator than the spontaneous potential barrier in non-insulated systems. Furthermore, because the capacitance of the Debye layer, which is in series with the insulation, is so much higher, it may be neglected

---

[4] A current review [38] is entitled "Electrowetting: a Recent Outbreak"

so that the effect does not depend on electrolyte-specific space-charge effects [41]. The use of a solid insulator also makes available a much wider range of materials for controlling the properties of the electrode surface. Thus, electrowetting on insulated electrodes offers substantial advantages which warrant reconsideration of electrowetting as a microactuation principle.

The irreversibility of the effect in these first studies was attributed to electrically-induced modification of the polymer at the edge of the droplet. Subsequent work by Welters and Fokkink [42] and Verheijen and Prins [43][44] at Philips Research Laboratories produced highly reversible effects using high dielectric strength polymers (parylene and polyimide) for insulation along with a fluoropolymer (Telon AF) coating to increase the hydrophobicity and reduce the contact angle hysteresis of the surface. These studies primarily used 10 μm thick films and voltages of up to 200 – 300 V to achieve maximum contact angle reduction. Electrowetting has also emerged recently as a tool for fundamental studies of wetting dynamics and for improving industrial coating processes [45] [46]. Other applications include a voltage controlled variable focal length lens [47] and a high-density capillary array with possible application as a programmable optical filter [38].

Deviations from Ideality

Although Equation 1.7 predicts complete wetting (i.e. $\cos\theta = 1$) of the solid at sufficiently high voltages, this condition has never been observed experimentally. In practice, the contact angle variation slows down at high fields, and saturates before the onset of complete wetting. For the PET films, saturation occurred at about 30° while for parylene films the angle was about 60°. Quilliet and Berge [38] attribute the difference to the use of ac voltage in the former case and dc voltage in the latter case. Different physical mechanisms have been proposed to explain contact angle saturation depending on the type of voltage. For ac fields, ionization of the air around the edges of the droplet at high fields has been observed and invoked to explain saturation [48], while for dc fields reversible trapping of charge in the insulator is suspected [43]. However, fundamental uncertainties concerning this effect persist and further studies are needed.

Some uncertainties also surround the basic formulation of the electrowetting problem. Blake *et al.* [45] have proposed that based upon thermodynamic considerations, the constant in the denominator of the voltage term in Equation 1.7 should be four instead of two. Although this is inconsistent with most published electrowetting data, Janocha *et al.* [49] studied “reverse” electrowetting of decane droplets in water on a number of different surfaces and found quadratic behavior with a coefficient ranging from 0.15 – 0.25. Another author [50] claims that the observed spreading of the droplet is not due to surface tension at all, but rather to line tensions resulting from the redistribution of charges along the contact line. Quilliet and Berge [38] point out that this would lead to a droplet size dependence which has not been observed. In any case, the effect of excess charge at the edge of the droplet may introduce new non-ideal phenomena. For example, contact line instabilities resulting in the expulsion of microdroplets from the perimeter of the droplet have been reported in some cases [39].

1.5 Chapter Summary and Conclusions

Recent advances in microfluidics have stimulated a desire to realize increasingly more complex systems, but so far, integration of the diverse components and technologies has remained a very challenging problem. Recognizing the power of digital design and organization techniques in microelectronics, we propose that similar advantages may be obtained in microfluidic systems that operate on discretized units of fluid using a small set of well-defined basic operations. Such “digital microfluidic” systems may offer more flexible and efficient microliquid handling capabilities and permit more complex, integrated and reconfigurable microfluidic systems.

However, the implementation of digital microfluidics requires new microactuation principles which allow independent manipulation of multiple fluid volumes. Many currently favored methods such as electrokinetic transport are unsuited for digital microfluidics because the driving force is applied globally prohibiting *independent* manipulation of fluid units. A more appropriate strategy would be based upon discrete droplets which are activated by local surface tension gradients. In this manner, droplets may be locally controlled and the use of surface tension exploits favorable force scaling behavior in the microdomain.

Thus, implementation of digital microfluidics hinges upon control of interfacial tension by some external means. While a number of chemical, thermal and electrical methods for controlling surface tension have been proposed in recent years, electrowetting, which is essentially direct electrical control of the surface tension, appears to offer substantial advantages over other methods. These advantages include: minimal disruption of the fluid, minimal requirements for the fluid, fast and large effects, efficient and direct control of the energy, and the inherent ease of implementing and controlling an electrically based method.

Chapter 2

Microactuator Theory and Design

2.1 Planar Electrowetting Microactuators

Electrowetting provides a mechanism for voltage control of the solid-liquid interfacial energy, but droplet microactuation also depends on asymmetrical energization of this interface. The required asymmetry is introduced by dividing the planar electrode in Figure 1.6 into an array of multiple independently controllable electrodes. The wire may be replaced with a continuous planar electrode to ensure continual contact with the droplet as it moves. This arrangement describes the basic electrowetting planar microactuator structure shown in Figure 2.1.

A polarizable and conductive liquid droplet is sandwiched between the two plates and surrounded by a filler fluid which may be air or an immiscible liquid such as silicone oil to prevent evaporation of the droplet. Both plates are covered with a hydrophobic coating that is electrically insulating on the bottom-plate, and may or may not be insulating on the top-plate. The high contact angle of the surface ensures that in the absence of an electric field the interfacial energy is lower when covered by the non-polar fluid, and that in the presence of the field the energy is lower when covered by polar conductive fluid.

The droplet volume is slightly larger than the pitch of the electrodes to ensure overlap between the droplet and adjacent neighboring electrodes. When all electrodes are at the same potential the interface is uncharged and the system energy is independent of the droplet position. When a potential difference is applied between an electrode underneath the droplet and the other electrodes, a surface energy gradient is established which drives the droplet onto the charged electrode. As the droplet aligns itself with the charged electrode it maximizes both the area of overlap and the electrostatic energy stored in the effec-

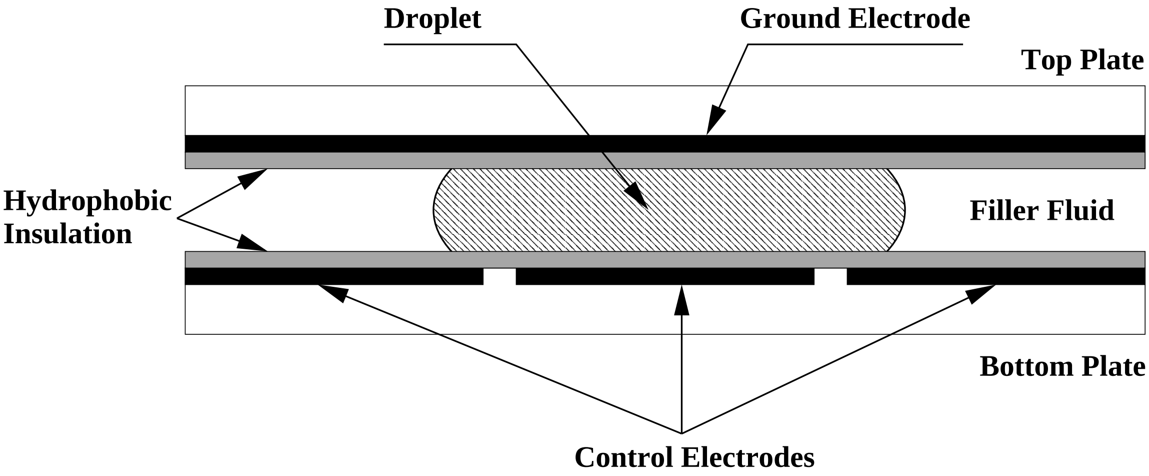

Figure 2.1: Side-view schematic of the planar electrowetting microactuator

tive capacitors between the droplet and electrodes. Since the force is applied directly at the meniscus, no fixed channels or structures between the plates are necessary to contain the droplet. Thus, reconfiguration within the liquid layer is facilitated, as channels, reservoirs, mixers,etc. only exist in a virtual sense anyway.

Overlap between the droplet and adjacent electrodes may be increased through the use of interlocked or interdigitated electrode shapes as illustrated in Figure 2.2. Such designs increase the dynamic range of droplet volumes which may transported and reduce the sensitivity with respect to the position of the droplet relative to the electrode. For non-interdigitated square electrode designs, the minimum droplet volume is approximately the product of the electrode area and gap height between the plates. When relaxed, the expected footprint of a droplet corresponding to this minimum volume is approximately a circle of diameter $D = 2L/\sqrt{\pi}$, where L is the electrode length. Thus, the overlap between the centered and relaxed droplet with each adjacent electrode is 6.4% L, and droplets may be transported by successive cycles of “shift-and-center” then “relax-and-touch-next”. However, as the droplet footprint exceeds the area of the electrode, centering becomes less effective and droplet transport may no longer be possible. In order to relax

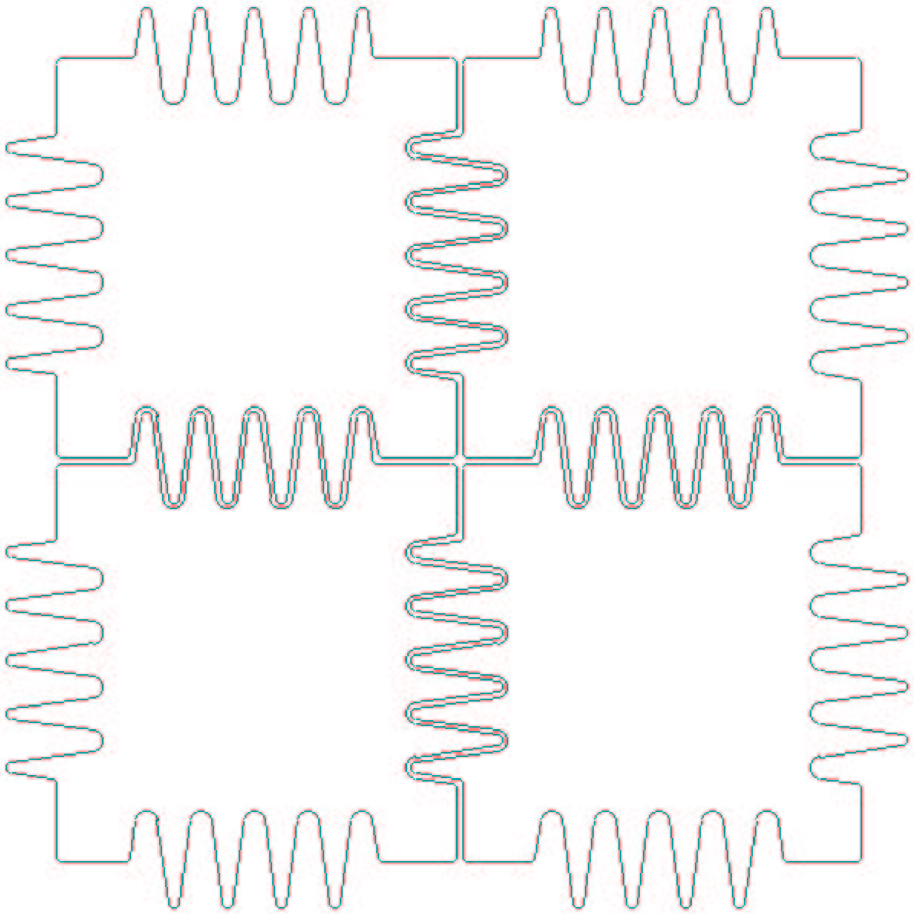

Figure 2.2: Interdigitated electrode design. Top-view of a 2 x 2 array showing typical spacing and arrangement of electrodes.

the volume sensitivity we used the interdigitated electrodes of Figure 2.2 for the majority of our work. The disadvantage of this electrode design is that it is more difficult to layout and fabricate, more likely to result in voltage breakdown of the insulator due to the sharper contours, and more difficult to model and analyze due to the complex geometry.

Electrowetting microactuators may also be employed for the generation, deformation or splitting of droplets. Figure 2.3 presents a scheme for isolating electrode-sized droplets from a larger liquid reservoir. An “inlet” electrode is first energized creating a liquid bridge extending from the source (on the left, not shown) to the droplet-forming electrodes (Figure 2.3A). The “cut-off”, “packing” and “array” electrodes are then simultaneously energized and the liquid advances over them (Figure 2.3B). The cut-off electrode is then de-energized and the liquid source recedes, breaking the meniscus over the cut-off electrode and leaving a newly formed droplet behind (Figure 2.3C). Finally, the packing electrode is de-energized and the droplet is consolidated onto the array electrode (Figure 2.3D). The purpose of the packing electrode is to provide additional volume to the droplet to ensure that it can be transported from the array electrode to the adjacent array (on the right, not shown).

Following isolation from the liquid reservoir, droplets may be further subdivided by “stretching and breaking” them across array electrodes. Figure 2.4 depicts a possible scenario involving a 4 x 7 checkerboard array of control electrodes. The droplet initially covers an area of four electrodes, and may be transported by simultaneous activation of groups of four electrodes within the array (Figure 2.4A,B). The droplet is then divided by stretching it while deactivating the electrode beneath the center of the droplet (Figure 2.4C,D). The resulting halves may then be transported by activation of groups of two electrodes at a time (Figure 2.4E). These halves may then be further subdivided producing four droplets which are transportable by activation of single electrodes (Figure 2.4E). This example is meant to illustrate the potential flexibility of systems based upon arrays of electrowetting electrodes. For sufficiently small pitch sizes, virtually any electrowetting-based

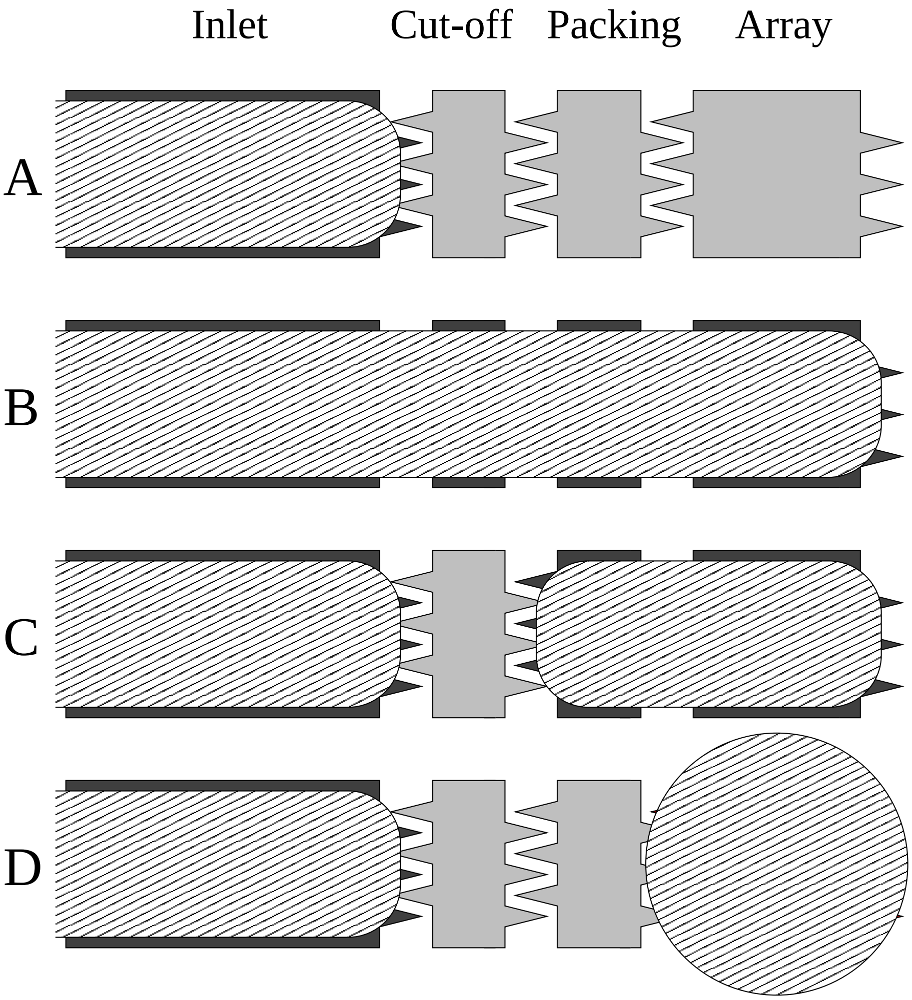

Figure 2.3: Formation of droplets from a liquid reservoir using specialized electrodes

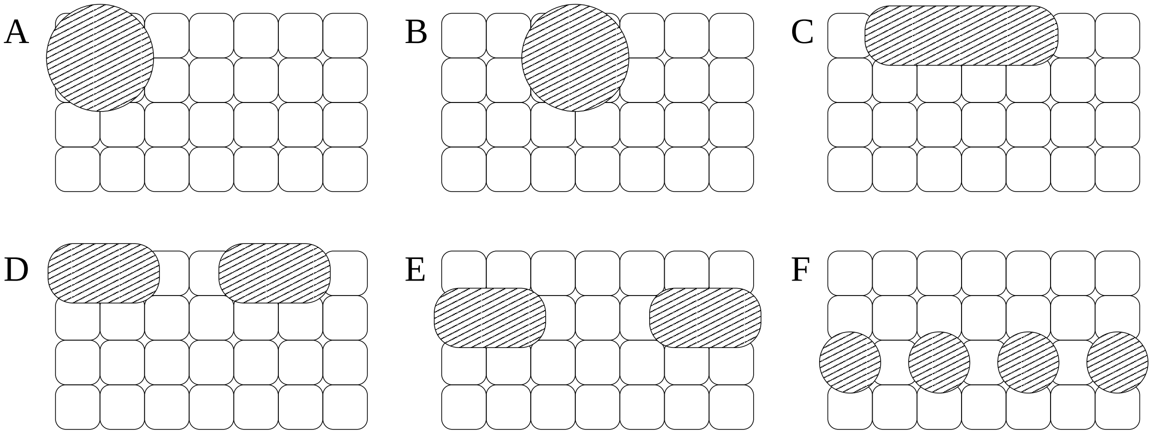

Figure 2.4: Example of operations conducted on a two-dimensional array of electrodes

manipulation may be accomplished by activation of specific patterns of electrodes on the surface.

2.2 Electrical Design and Analysis

2.2.1 Electrode Arrangement

Several variations on the basic microactuator differing in the arrangement of the electrodes are illustrated in Figure 2.5. In the "double-insulated" design (Figure 2.5a) both the control electrodes and the ground electrode are isolated from the droplet by insulation. This arrangement prohibits transfer of charge to the droplet and mitigates against electrochemical reactions at the electrode-droplet interface. Alternatively, the top electrode may be uninsulated (Figure 2.5b) in which case the ground electrode directly contacts the droplet. The advantage of this design will become apparent in the analysis which follows. Another possibility is to have matching aligned control electrodes on both top and bottom plates (Figure 2.5c). It will be demonstrated that this arrangement is theoretically most efficient, but also the most challenging and expensive to manufacture and assemble. The simplest design to manufacture is the "single-sided" design (Figure 2.5d) without a top electrode. However,

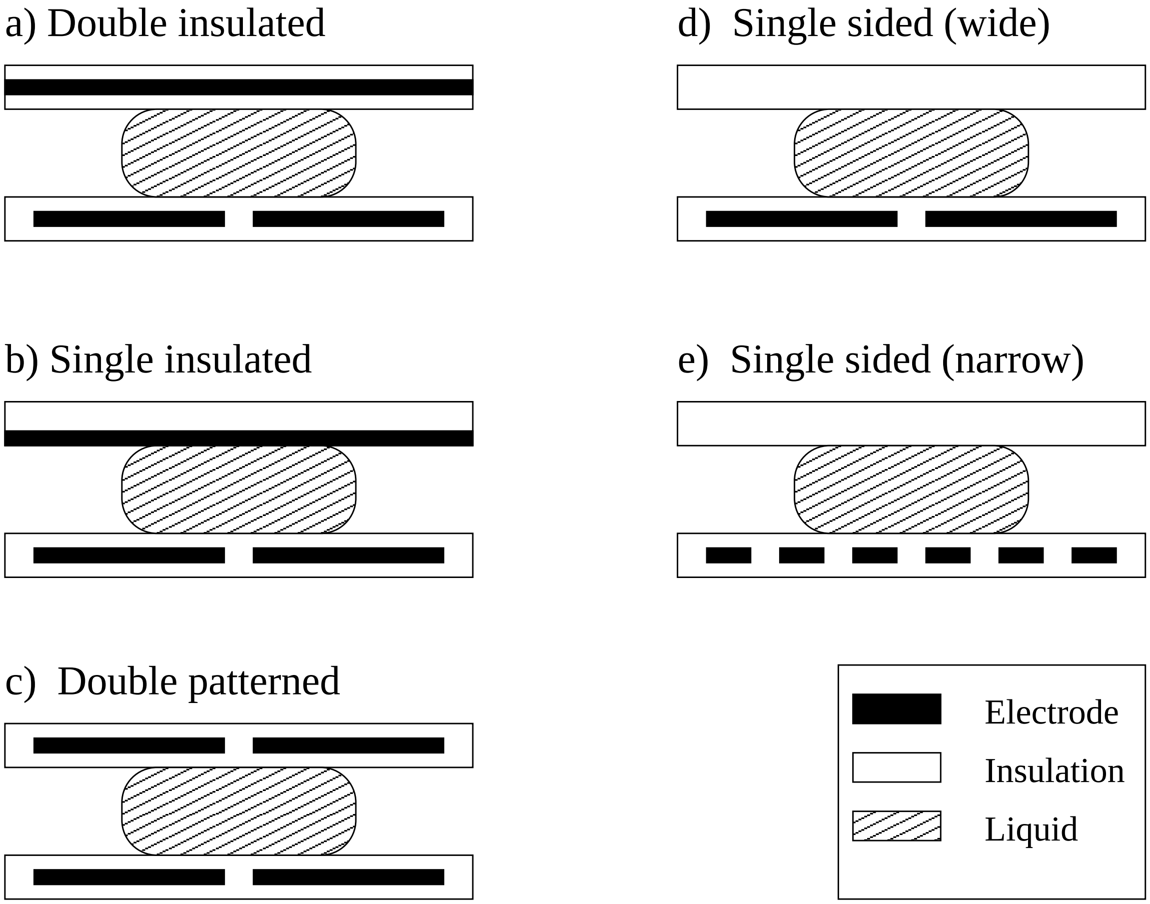
a) Double insulated

b) Single insulated

c) Double patterned

d) Single sided (wide)

e) Single sided (narrow)

Figure 2.5: Possible electrowetting microactuator electrode arrangements

it will be shown that this design is unworkable because it lacks the required asymmetry for generating a surface tension gradient. It is possible to operate without a top electrode when the control electrodes are small in size relative to the droplet as illustrated in Figure 2.5e which is essentially the design of Washizu [31]. The primary disadvantage of this approach is the large I/O count required and lack of a unit-cell-based design approach.

In order to evaluate the different electrode designs we present a simple parallel-plate capacitor model to calculate the total capacitive electrical energy stored in the system as a function of the droplet position between two adjacent electrodes (Figure 2.6). Such a model yields no information concerning the dynamics of droplet movement, but serves to establish certain features of the energy gradient which drives its motion. The droplet is assumed to be a perfect conductor and the energy stored at each interface is represented by a charged capacitor. The capacitor C_t models the capacitance between the droplet and top electrode while C_1 and C_2 represent the capacitance arising from the overlap between the droplet and electrodes 1 and 2 respectively. The electrodes and the droplet footprint are modeled as squares of side length L. We use a parallel-plate approximation for each capacitance so that the total capacitance is directly proportional to the area of the interface

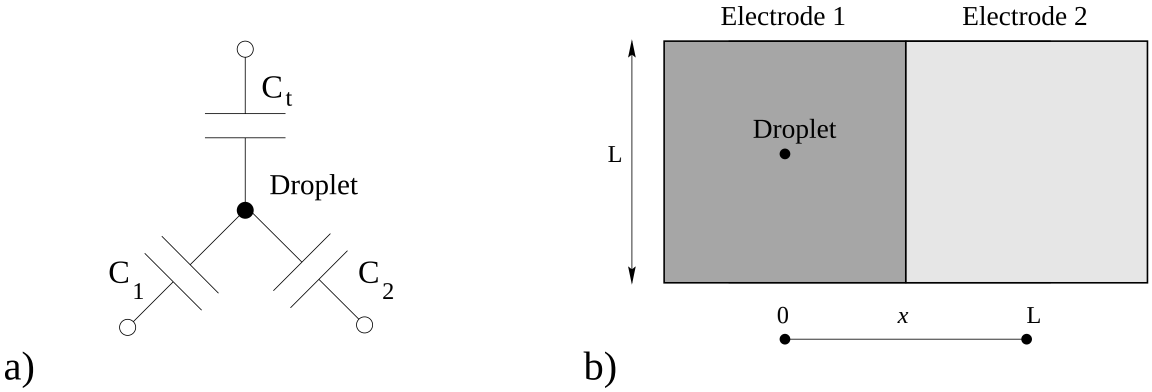

Figure 2.6: Simple parallel-plate capacitor model for analyzing electrode arrangement: a) the equivalent circuit with each interface represented by a capacitor b) the geometry with both droplet and electrodes modeled as squares

or overlap. The model could be extended to a droplet having a circular footprint, but the extra computational expense is not justified for this simple analysis. The centroid of the droplet can move laterally, assuming any position x between 0 (fully covering electrode 1) and L (fully covering electrode 2). The areas of overlap between the droplet and electrodes 1 and 2 are given by $L(L-x)$ and Lx respectively, and the area of the droplet-top electrode interface is always L^2. For our analysis we assume that the top electrode and electrode 1 are at ground potential while electrode 2 has a potential of V volts and we calculate the total electrostatic energy as a function of droplet position.

We consider first the single-insulated arrangement of Figure 2.5b. In this case C_t is shorted out of the circuit and the droplet potential is 0 V. If the insulation has capacitance per area C_0 then the total equivalent capacitance between the source and ground as a function of position is C_0Lx, and the total energy $E(x)$ is

$$E(x) = E_0Lx \tag{2.1}$$

where $E_0 = \frac{1}{2}C_0V^2$. Thus, the energy of the system increases linearly reaching a maximum value of E_0L^2 at $x = L$ as plotted in Figure 2.7. Now consider the double-insulated arrangement of Figure 2.5a. The parallel combination of capacitors C_t and C_1 appears in series with capacitor C_2. We initially assume that C_0 is the same for the top and bottom sides giving an equivalent capacitance of $C_0(Lx - \frac{x^2}{2})$ and energy

$$E(x) = E_0(Lx - \frac{x^2}{2}) \tag{2.2}$$

The energy increases parabolically to a value of $\frac{1}{2}E_0L^2$ at $x = L$ which is half of the value of the single-insulated electrode implementation. Both the single and double-insulated designs have positive energy gradients over the entire range [0,L] which implies that a driving force for complete transfer of the droplet exists.

In the single-sided design of Figure 2.5d C_t is open-circuited and capacitors C_1 and C_2

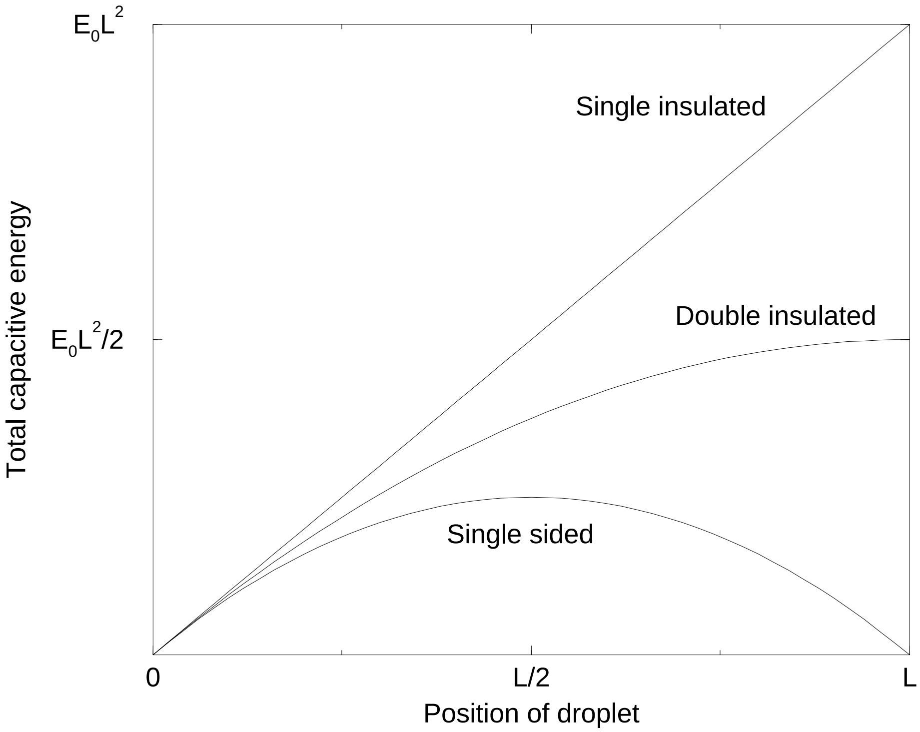

Figure 2.7: Total capacitive system energy as a function of droplet position between two electrodes

form a series combination with equivalent capacitance $C_0(Lx - x^2)$ giving

$$E(x) = E_0(Lx - x^2) \tag{2.3}$$

with an energy maximum at $L/2$. This energy maximum indicates that the droplet cannot be fully transferred between adjacent electrodes because no driving force exists once it has moved halfway and this design is therefore unworkable. This is a consequence of the geometrical symmetry and the polarity independence of the V^2 energy term. However, if the electrodes are much narrower than the droplet as shown in Figure 2.5e then the droplet may be transported incrementally in a single-sided design.

We can generalize these results by defining a parameter α to be the ratio of top insulation to bottom insulation capacitance per area. We then have

$$E(x) = E_0 \left(Lx - \frac{x^2}{1+\alpha} \right) \tag{2.4}$$

with a maximum value of $\frac{1}{4}E_0 L^2(1+\alpha)$ at $\frac{1}{2}L(1+\alpha)$. Higher values of α lead to tighter coupling between the droplet and top electrode resulting in less voltage drop across that interface and higher total energies. Whenever $\alpha < 1$ an energetic maximum exists between 0 and L and movement of the droplet may cease before fully crossing the next electrode. Even when α is slightly larger than unity, the energy gradient close to $x = L$ may be insufficiently steep to overcome retarding forces acting on the droplet. On the other hand, excess droplet area and interdigitated electrode designs may relax the requirement on α. However, as a general design rule, we require $\alpha \geq 1$.

The double-patterned arrangement of Figure 2.5c can be evaluated using a slightly modified four capacitor model. If V volts are applied simultaneously to a set of opposing top and bottom control electrodes with adjacent electrodes grounded the resulting energy function is

$$E(x) = 2E_0(Lx - x^2) \tag{2.5}$$

which is equivalent to the single-sided result because of the geometrical symmetry. However, this symmetry may be disrupted by applying different voltages to the top and bottom control electrodes. Thus, if $+V/2$ and $-V/2$ Volts are applied to the opposing control electrodes the new energy function is

$$E(x) = 2E_0Lx \tag{2.6}$$

The control electrodes are matched and so pin the droplet potential at 0 V giving the same result as the single-insulated arrangement with a factor of two difference attributed to the doubled capacitor area. This arrangement produces twice the maximum energy of the comparable single-insulated design and four times the maximum energy of the comparable double-insulated design. Furthermore, the maximum voltage drop across the insulator is half of the value of the single-insulated design. Thus for the same electric field in the insulator eight times more force can be generated than for the double-insulated design and four times more force than the single-insulated design.

In order to assess the validity of our square droplet approximation, we calculated the overlap as a function of position between a circular droplet and one of the interdigitated electrodes of Figure 2.2. Calculations were made for two circular diameters, corresponding to $1.2L$ and $1.5L$ where L is the pitch of the electrode. The overlap as a function of position offset from the center of the electrode is shown in Figure 2.8. Despite the complex geometry, the relationship is nearly linear with a slope of -1. Thus, the results of this capacitance analysis can be extended to this geometry as well.

2.2.2 Dielectric Breakdown Analysis

Considering the relatively large electric fields required for electrowetting it is important to ensure that dielectric breakdown does not occur during operation of the device. Since the electrowetting effect is dependent upon interfacial electrostatic energy (proportional to

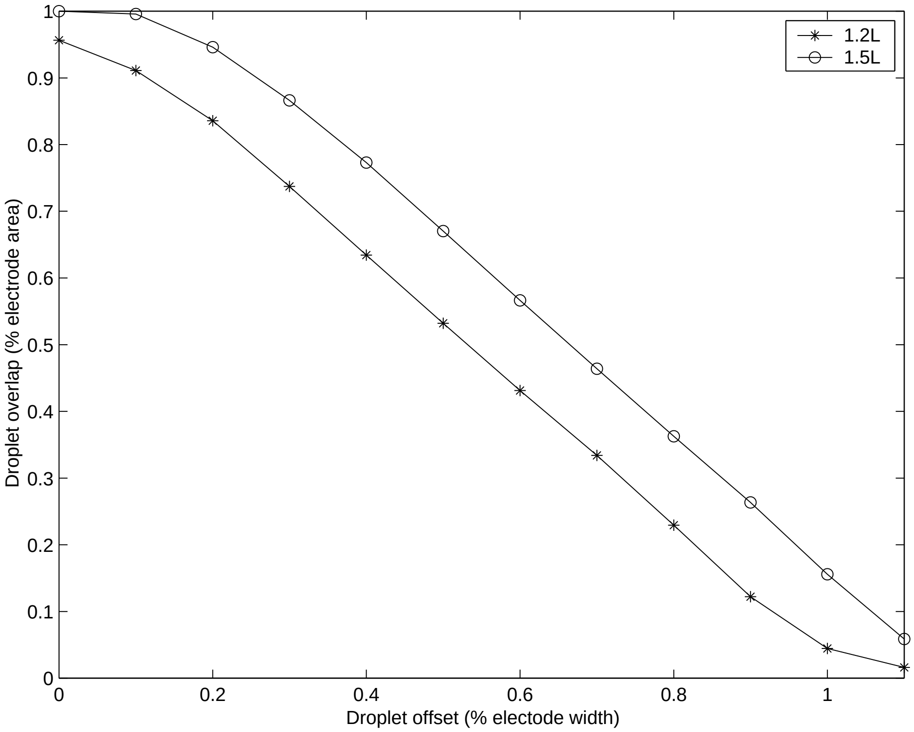

Figure 2.8: Overlap between a circle and interdigitated electrode as a function of relative position

V^2) while the breakdown voltage depends on the electric field (proportional to V) there always exists a minimum dielectric thickness d_{min} for which a given energy can be achieved without breaking down the dielectric. It is difficult to predict the useful range of energies for operation of the device. However, we may establish the criterion that the maximum energy should be sufficient to theoretically induce complete wetting of the surface according to Equation 1.7. Although this condition has never been observed experimentally due to contact angle saturation, it provides a useful upper bound for the energies that may be required.

The energy E_{cw} required for complete wetting of the solid depends on the initial contact angle θ_0 and surface tension of the liquid γ_{LV}. E_{cw} as a function of γ_{LV} is plotted for several values of θ_0 in Figure 2.9. For $\theta_0 = 100°$, which is typical of the insulators con-

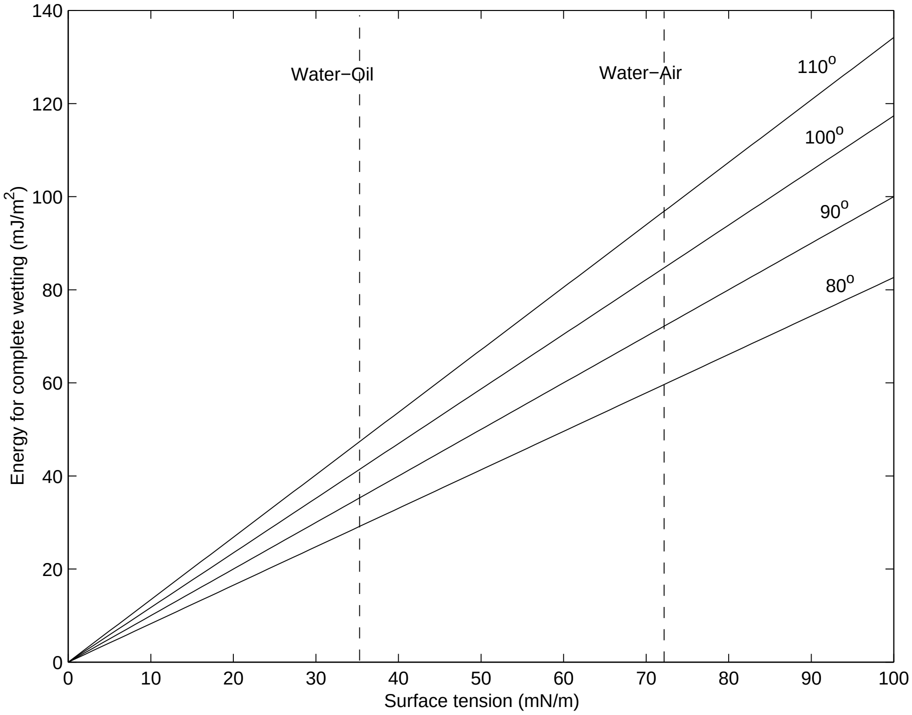

Figure 2.9: Theoretical energy required for complete wetting of the solid as a function of γ_{LV} for different values of θ_0. Dashed lines indicates surface tension values corresponding to water-oil and water-air interfaces.

Material	d_{min} **(μm)**	V_{br} **at** d_{min} **(V)**	d_{min} **at 100 V (μm)**	d_{max} **at 100 V (μm)**
SiO_2 (PECVD)	0.02	10	0.25	2.58
Parylene C	0.12	27	0.45	1.66
Teflon AF	0.22	47	0.48	1.02

Table 2.1: Minimum and maximum insulator thickness for 100 V electrowetting system. Material parameters can be found in Table 3.2

sidered here, the energy of complete wetting for the water-air system ($\gamma_{LV} = 72$ mN/m) is 84 mJ/m^2 and for the the water-oil system ($\gamma_{LV} \approx 35$ mN/m) is 40 mJ/m^2. The minimum allowable dielectric thickness must satisfy the condition $E_{bd} > E_{cw}$ where E_{bd} is the dielectric breakdown field of the insulator. Thus,

$$d_{min} = \frac{2E_{cw}}{\epsilon_r \epsilon_0 E_{bd}^2} \tag{2.7}$$

Values of d_{min} corresponding to E_{cw}=84 mJ/m^2 are calculated for three different insulators in Table 2.2.2. The breakdown voltage V_{br} at d_{min} is the minimum theoretical operating voltage that can satisfy the energy requirement in air without breaking down the insulator. For proportionally larger operating voltages and insulator thicknesses the margin of safety for breakdown is improved. We chose to accept a maximum operating voltage of 100 V and recalculated minimum (limited by E_{bd}) and maximum (limited by E_{cw}) thicknesses for each insulator in Table 2.2.2. These calculations indicate that satisfactory electrowetting force can be generated using voltages less than 100 V when the insulation is 0.5 – 1.0 μm thick.

Dielectric breakdown may also occur in the insulating fluid surrounding the droplet. Therefore it is important to ensure that the gap between the plates is sufficiently large to prevent shorting of the electrodes through the filler fluid. We analyze here the breakdown properties of the fluid far away from the droplet, neglecting any influence of the droplet or electrode shape upon the field. Consider an ideal parallel-plate capacitor with three dielectric regions with interfaces parallel to the plates. From electrostatic considerations the field E_1 in any one of the dielectrics is related to the voltage V_0 across the plates as

$$E_1 = \frac{V_0}{d_1 + \frac{\epsilon_1}{\epsilon_2} d_2 + \frac{\epsilon_1}{\epsilon_3} d_3} \tag{2.8}$$

where ϵ_n and d_n are the dielectric constant and thickness respectively of each of the three regions. When the top and bottom insulation are identical we may write the field in the medium E_m as

$$E_m = \frac{V_0}{h + \epsilon_m \frac{d_i}{\epsilon_i}} \tag{2.9}$$

where h is the gap height, ϵ_m and ϵ_i are the dielectric constants of the filler fluid and solid insulation respectively, and d_i is the total thickness of the insulation on both top and bottom plates.

The breakdown voltage of the filler fluid as a function of the ratio d_i/ϵ_i is plotted in Figure 2.10 for several values of h in both air ($\epsilon_r = 1.0$, $E_{bd} = 3.0$ MV/m) and silicone oil media ($\epsilon_r = 2.4$, $E_{bd} = 13.8$ MV/m). For most dielectrics a few microns in thickness, $d_i/\epsilon_i \approx 1$ μm. With an maximum operating voltage of 100 V the minimum gap height for silicone oil is less than 10 μm which is substantially less than is required for the present work. The minimum gap height in air is larger (≈ 30 μm at 100V), but it is unlikely that such small volumes of fluid would be handled in air anyway.

2.3 Dimensionless Number Analysis

Dimensionless ratios that compare forces encountered in flowing fluids are often used in fluid dynamics to gain insight into otherwise complicated fluid behavior. The forces of interest here include pressure, inertia, viscosity, gravity and surface tension. A ratio of any two of these forces yields a dimensionless number which qualitatively characterizes the behavior of the fluid.

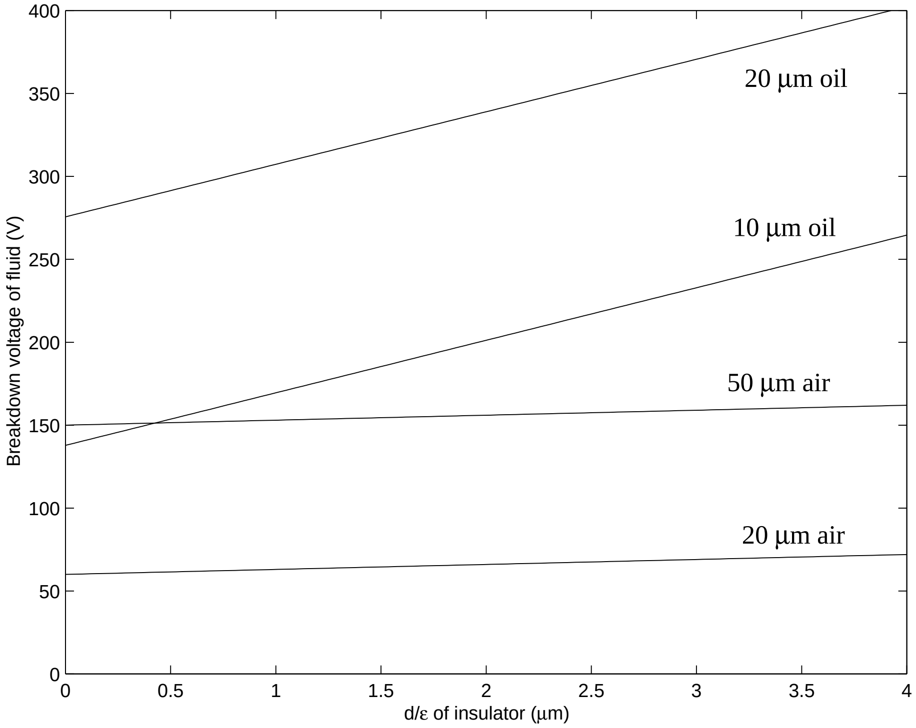

Figure 2.10: Breakdown voltage of filler fluid (air or oil) as a function of solid insulator properties for several values of h

One of the most important dimensionless quantities is the **Reynolds number** which is the ratio of inertial to viscous forces in a system, and is given by

$$Re = \frac{\text{inertial forces}}{\text{viscous forces}} = \frac{\rho U L}{\mu} \tag{2.10}$$

where ρ and μ are the fluid density and viscosity respectively, U is the velocity and L is a characteristic length of the flow field. For the systems under consideration here, 1 mm is considered to be an upper bound for L and 10 cm/s an upper bound on U. Thus for water[1] Re has a maximum value of approximately 100.

The Reynolds number signifies whether a particular flow pattern is laminar or turbulent, with the transition from laminar to turbulent flow usually occuring above 2300. However, Gravesen [3] has suggested that this value may not be relevant for microfluidic systems because L is often shorter than the entrance length for fully developed flow. When the ratio of L to the hydraulic diameter D is less than 70, Gravesen recommends that L be set equal to the entrance length for fully developed flow. In this case, the transitional Reynolds number Re_t is approximated by $30L/D$. Assuming a minimum L/D ratio of 3, the relevant minimum value of Re_t becomes 90. Since Re_t(min) is close to Re(max), it is possible that some turbulent flow may arise in the largest droplets moving at the highest velocities. However, generally speaking, laminar flow should dominate and mixing of fluids should occur only through diffusive action.

The **Bond number** is a measure of the hydrostatic gravitational force relative to the surface tension force and is given by

$$Bo = \frac{\text{gravitational force}}{\text{surface tension force}} = \frac{\rho g L^2}{\gamma} \tag{2.11}$$

where γ is the surface tension and g is the acceleration due to gravity. For water at a length scale of 1 mm, $Bo \sim 10^{-1}$ which indicates that the droplet shape is dominated by surface

---

[1] For water, $\mu = 1.0$ cP = 0.01 g/(cm·s), $\rho = 1.0$ g/cm^3, γ = 72 dyn/cm

tension rather than gravitational effects. The surface tension and gravitional forces acting on a spherical water droplet are compared graphically in Figure 2.11 where it can be seen that gravitational forces become relatively insignificant for droplets smaller than a few mm. Since 1 mm represents an upper limit for the length scale in this study, the effects of gravity are neglected when considering the shape of droplets.

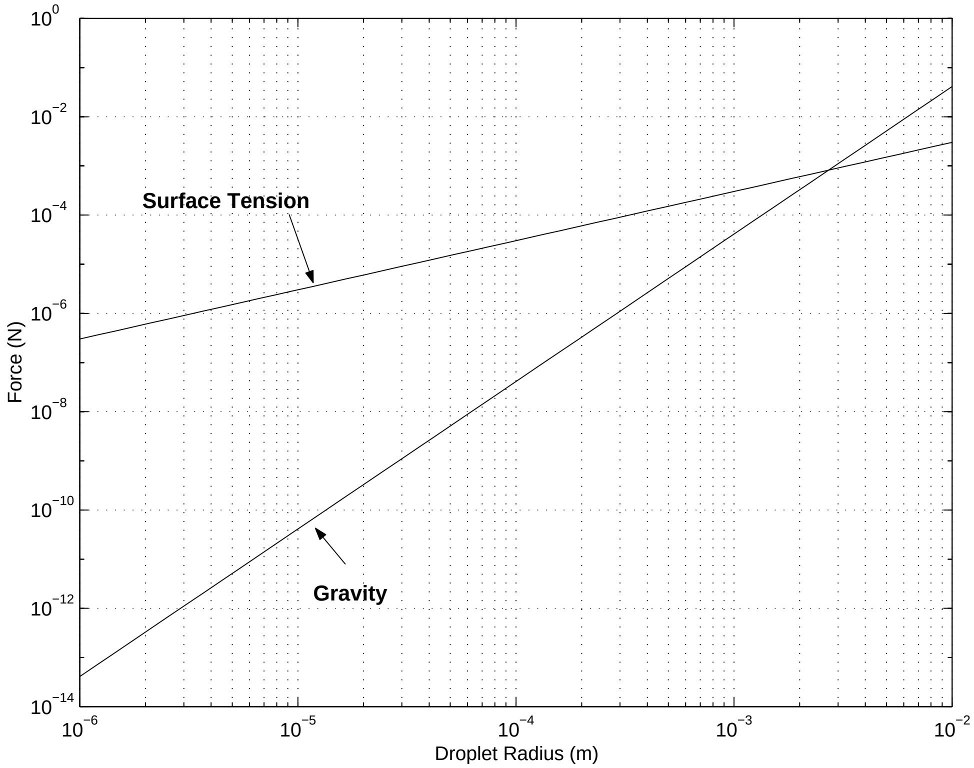

Figure 2.11: Comparison of surface tension and gravitational force acting on a spherical water droplet

Another dimensionless number of interest is the **capillary number** which compares viscous and surface tension forces and is given by

$$Ca = \frac{\text{viscous force}}{\text{surface tension force}} = \frac{\mu U}{\gamma} \tag{2.12}$$

The capillary number is important for characterizing the speed of contact line motion during wetting or dewetting processes because it determines the shape of the free surface near the contact line. For water with a velocity of 10 cm/s, $Ca \sim 10^{-3}$, which indicates that surface tension effects should determine the dynamics of contact line movement.

The **Weber number** is the ratio of inertial forces to surface tension forces and is given by

$$We = \frac{\text{inertial force}}{\text{surface tension force}} = \frac{\rho L U^2}{\gamma} \tag{2.13}$$

with $We/Ca = Re$. The Weber number is often used to characterize the stability of fluid streams in multiphase flow. For example, when $We > 12$ droplets are known to become unstable and to flatten, while higher values often result in droplet fragmentation. For water, with $U = 10$ cm/s and $L = 1$ mm, $We \sim 10^{-3}$ indicating the inertial stresses alone should not cause droplets to fragment.

2.4 Chapter Summary and Conclusions

Employment of electrowetting for microactuation of droplets requires asymmetrical energization of the solid-liquid interface in order to generate the necessary surface tension gradient. Using photolithographically defined metal electrodes, the required asymmetry can be realized within a planar structure in which the droplet is sandwiched between two plates. This same microactuator structure can be used to generate, split, or merge droplets in addition to transporting them. Thus, higher order structures such as mixers or reactors can be monolithically integrated with the transport system. Since there are no fixed channels and few unique structures, real-time reconfiguration through software control is a possibility.

An analysis of different electrode arrangements establishes the importance of minimizing the voltage drop across the unpatterned ground electrode insulation. Although, an arrangement utilizing patterned and insulated electrodes on both sides is most efficient when both voltage polarities are available. We expect that electrical energies of up to 100 mJ/m^2 may be required to achieve significant actuation. An electrical analysis indicates that this energy can be achieved at less than 100 V with insulators 0.5 – 1.0 μm thick while providing a comfortable margin against dielectric breakdown. To avoid breakdown through the filler fluid at these voltages, the gap height should be at least several tens of μm. We also note that the minimum design feature is likely to be at least an order of magnitude smaller than the electrode size. Thus, both of these factors point to a minimum droplet scale of about 50 μm or 0.1 nl for the present technology. A dimensionless analysis of the forces present in the system indicates that surface tension effects should dominate other phenomena as long as the length scale is below a few mm which establishes an upper limit on the droplet volume of about 10 μl or 10,000 nl.

Chapter 3

Microactuator Chip Fabrication and Materials

Based upon the analysis of the previous chapter a prototype electrowetting microactuator chip was designed, fabricated and tested. Initially disappointing process yields and test results led us to re-evaluate the chip design and further investigate certain critical materials issues before proceeding with subsequent fabrication work. We first describe our initial design and its shortcomings, followed by a discussion of materials issues. Finally, we describe the design and fabrication of the later prototypes which were successfully operated.

3.1 Design and Fabrication and Testing of Initial Prototypes

The initial design consisted of a 6 x 7 array of 150 μm pitch interdigitated electrodes with droplet-forming inlet electrode sets flanking both sides of the array. Each chip contained four separate arrays sharing a common wiring bus but having droplet-forming electrodes of different widths. A circular electrode, 1.6 mm in diameter, was connected through a 150 μm wide extension arm to each set of droplet-forming electrodes.

The circular electrode was part of a surface tension inlet designed to transport liquid from a circular opening in the top-plate to the droplet-forming electrodes at the edge of the array (Figure 3.1). The surface tension inlet consisted of a hole in the top-plate surrounded by a hydrophilic ring and channel on an otherwise hydrophobic glass plate. Matching hydrophilic rings on both sides of the top-plate and the top-side of the bottom plate, along with the hydophilic glass interior of the hole, provided a surface tension well for containment of the source droplet. Hydrophilic channels on the interior surfaces extending from the well to the array provided a path for surface tension driven liquid priming. The matching circular electrode and extension were designed to provide additional energy for priming if required. The circular electrode also served as a visible structure for alignment of the top and bottom plates.

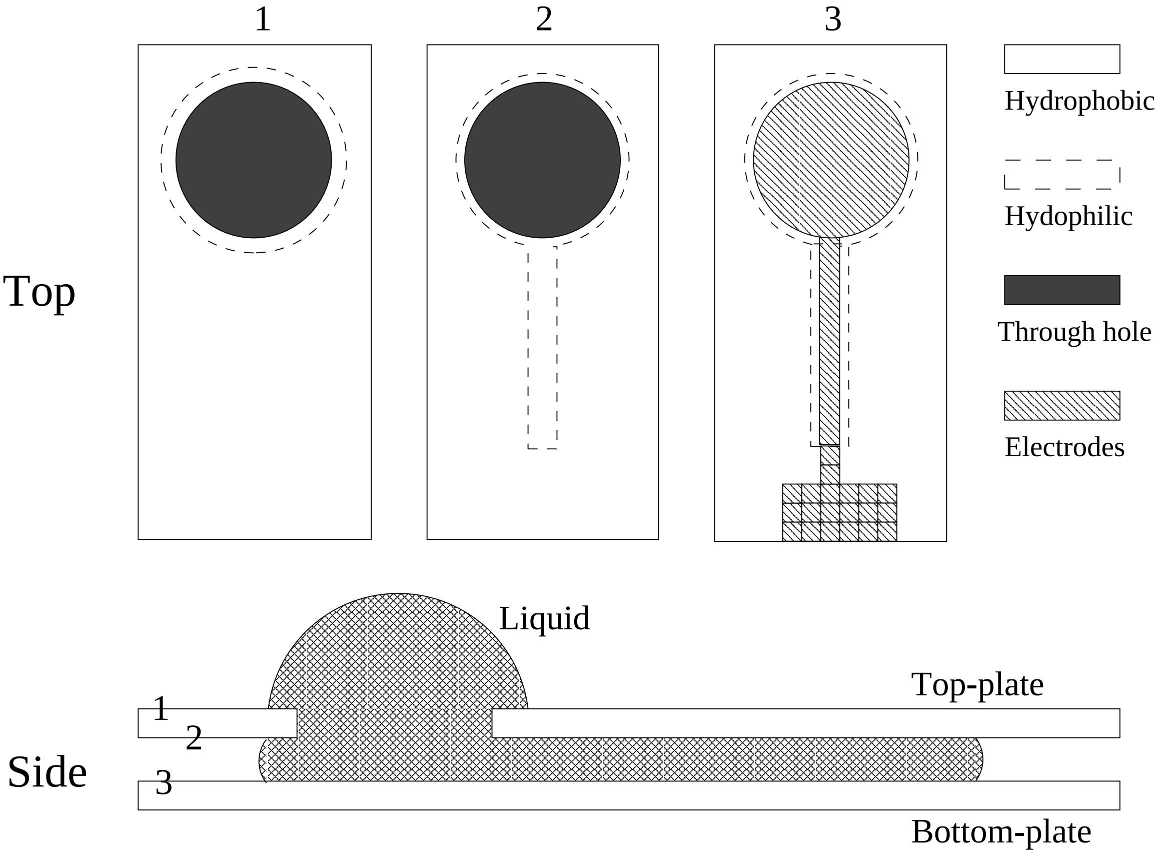

Figure 3.1: Surface-tension inlet employing both electrowetting and patterned surface chemistry to deliver fluid from a containment well and hole in the top-plate to the microactuator array (not to scale)

The electrowetting chips were fabricated using standard microfabrication techniques at the Biomedical Microsensors Laboratory (BMMSL) at North Carolina State University. The bottom-plates were fabricated on six-inch square borosilicate glass wafers using the process illustrated in Figure 3.2. First, a 1500 Å thick film of Au with a thin Cr adhesion layer was patterned to form the wiring layer. Next, 4000 Å of RF sputtered SiO_2 was deposited as a interlevel dielectric. Vias were etched in the dielectric and a second Cr/Au layer was deposited and patterned to form the control electrodes. Another 4000 Å of SiO_2 was deposited as insulation over the control electrodes and vias were etched to provide access to the bonding pads. Next, a layer of photoresist was deposited and patterned to protect areas of the hydrophilic inlet areas from a organosilane hydrophobization treatment. Finally, a 25 μm thick photo-patternable polymer film was laminated onto the wafer and patterned to provide stand-offs for attachment of the top-plate.

a) Deposit and pattern metal wiring

b) Deposit interlayer insulation

c) Pattern interlayer insulation

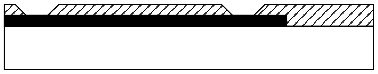

d) Deposit and pattern metal electrodes

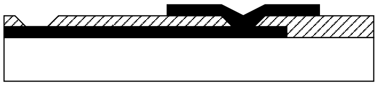

e) Deposit silicon oxide insulation

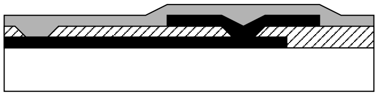

f) Pattern vias in oxide

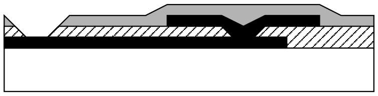

g) Hydophobize oxide surface

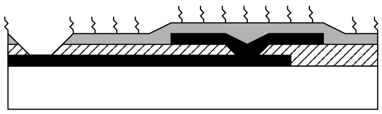

Figure 3.2: Fabrication process for initial electrowetting chip prototypes

The top-plates were fabricated separately on 0.3 mm thick three-inch square borosilicate glass plates. First, 1.2 mm diameter holes were milled in the glass, followed by deposition of a conductive indium-tin-oxide (ITO) layer to form the ground electrode. The

ITO was insulated with 4000 Å of sputtered SiO_2. Photoresist was then patterned on both sides of the wafer to protect the hydrophilic well and inlet areas from an organosilane hydrophobization treatment. The wafers were diced and the top and bottom plates were aligned and bonded together. Electrical connection to the bonding pads was made using 0.6 mm pitch heat-seal tape. The heat-seal tape was connected to a custom-made flexible patterned cable (Cu on Mylar) which was terminated with a standard 0.100" pitch socket connector. A spill-dam to contain the silicone oil was constructed on the assembled chip using silicone adhesive.

Due to an unexpected combination of processing problems, the yield of testable devices at the end of the first run was essentially zero. Before undertaking further fabrication, the design was modified to significantly reduce the process complexity and stringency as documented in Table 3.1. The electrode pitch was increased from 150 μm to 600 μm and the inter-electrode spacing (the minimum feature) was increased from 2 μm to 10 μm. The increased pitch also permitted a larger gap height and the 25 μm photopatterned gasket was replaced with a 100 μm thick manually applied self-adhesive film.[1] The dimensions of the array were reduced to 6 x 6 resulting in a lower I/O count. Since electrical testing revealed numerous shorts between the metal layers in the first run, the interlevel dielectric was changed from 0.4 μm of SiO_2 to 2.0 μm of polyimide which was considered to be more reliable. The surface tension inlet was abandoned as it significantly increased the process complexity but was not central to the demonstration of electrowetting-based droplet microactuation. The droplet-forming electrodes were retained with the source droplet to be inserted between the plates at the time of assembly rather than delivered through a hole in the top-plate.

The revised design was fabricated and a much more satisfactory yield of testable devices was obtained. A photograph of the central portion of one of the chips is shown in

---

[1] Double-sided Scotch brand tape

Specification	Prototype A	Prototype B
Electrode pitch (μm)	150	600
Inter-electrode spacing (μm)	2	10
Gap Height (μm)	25	100
Number of masks	9	4
Number of I/O's	50	44
Metal layers	1500 Å Cr/Au	1500 Å Cr
Interlevel dielectric	0.4 μm SiO_2	2.0 μm polyimide
Vias	12 μm circles	30 μm squares
Insulator	0.4 μm SiO_2	0.4 μm SiO_2

Table 3.1: Design specifications of initial prototypes

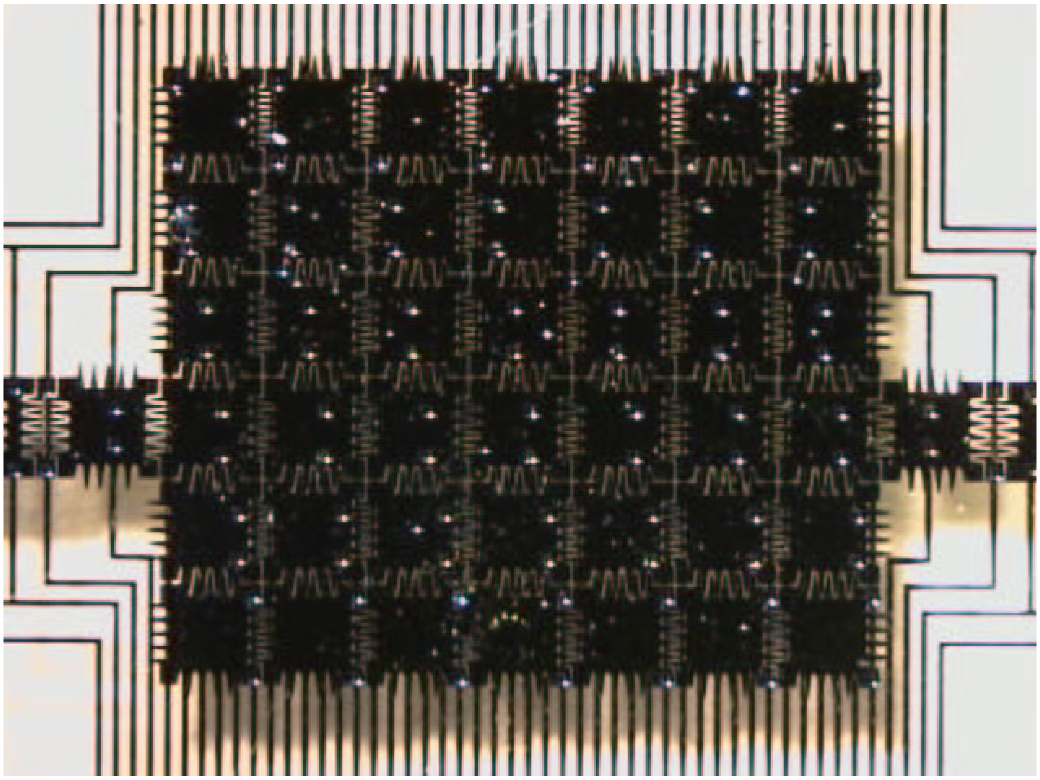

Figure 3.3: Top-view of electrowetting chip (prototype B) with 600 μm electrode pitch. The bright spots on the electrodes are reflections from the vias.

Figure 3.3. Several different problems emerged during testing of these devices. First, the heal-seal tape connections to the bonding pads proved to be extremely unreliable, failing to provide continuity in about 50% of the connections tested. It is possible that the heat-seal tape may have been aged or defective or that the metal pads had become contaminated during one of the process steps. The second problem was the presence of shorts between some electrodes, affecting 10 – 15 % of those tested. Shorts may arise either from incomplete lift-off of the metal between the electrodes or from defects in the polyimide interlevel dielectric layer. However, the most serious problem was the failure of the hydrophobized sputtered SiO_2 top insulation layer against electrolyte solutions. Direct current flow and electrolytic bubble generation were repeatedly observed when small voltages were applied between the electrolyte droplets and electrodes, thus rendering the devices inoperable.

3.2 Materials Design

In this section we discuss materials issues related to the electrowetting microactuator. There are essentially three types of materials required for an operable device. A conductor material to form the electrodes, an dielectric material to provide the capacitance between the liquid and conductor, and finally a hydrophobic coating at the interface of the insulator and liquid. Conceivably, the dielectric and hydrophobic layers could be of the same material, but this demands a rather rare combination of favorable electrical, mechanical and chemical properties.

3.2.1 Electrode Insulation

Having observed the inadequacy of the sputtered SiO_2 insulation in our first prototypes we evaluated a number of alternative inorganic and polymeric insulators. In addition to providing adequate insulation against conductive liquids, the electrode insulation should ideally possess:

- High dielectric constant
- High dielectric strength
- Low intrinsic charge
- Good thermal stability
- Good mechanical stability
- Good solvent resistance

High dielectric constant and dielectric strength are important for maximizing the microactuation force, while mechanical, thermal and charge stability are important for process compatibility and device reliability.

The insulators that were evaluated and their properties are listed in Table 3.2. We previously determined that an energy of roughly 100 mJ/m^2 at 50 – 100 V was a convenient target to achieve a large electrowetting effect at moderate voltages. This requires an insulator capacitance of 2 – 8 nF/cm^2. Thus, we evaluated each insulator at thicknesses designed to provide this range of capacitance. Samples of each insulator film were deposited on chips of Cr coated glass and tested by applying voltage between the Cr layer and a Pt wire immersed in an electrolyte droplet (5 – 10 μl of 0.1 M KCl) on the surface of the chip. Observation of bubbles or direct current flow, particularly at low voltages, was considered a negative result for this test. The origin and thicknesses of the tested samples are listed in Table 3.3 and described below.

Silicon dioxide The principal advantages of SiO_2 as a capacitive insulator are its high dielectric constant, high dielectric strength and availability as a widely used material in MEMS and microelectronics. Additionally, there exists a well developed chemistry for the modification and biofunctionalization of silica surfaces. Although poor results were obtained with sputtered SiO_2, plasma-enhanced chemical vapor deposition (PECVD) of SiO_2

Material	ϵ_r	**Diel. str. (MV/cm)**	**Proc. temp (°C)**	**Max use temp (°C)**
SiO_2 (PECVD) [51]	4.9	4–6	250	—
SiN (PECVD) [51]	6–9	5	250–350	—
Spin-on-glass [52]	5–7	—	400–450	—
DLC [53]	2.6–4.0	—	—	—
Parylene C [54]	3.15	2.2	room	290
Parylene N [54]	2.65	2.8	room	420
Polyimide [53]	3.2–3.6	1.2–2.4	300–400	450
Teflon AF (1600) [55]	1.93	2.1	170–330	360

Table 3.2: Physical properties of candidate insulators including dielectric properties, typical process temperatures and maximum use temperatures

Material	**Thickness (Å)**	**Source**
Silicon dioxide (sputtered)	4000	NCSU BMMSL, Raleigh NC
Silicon dioxide (PECVD)	2500	Tribofilm Inc., Raleigh NC
Spin-on glass (Flimtronics 20A)	2700, 5400	Duke cleanroom
Spin-on glass (Filmtronics 70F)	7000	Duke cleanroom
Silicon nitride (PECVD)	2500	Tribofilm Inc., Raleigh NC
Silicon nitride (PECVD)	3800	Trion Technology, Tempe AZ
Silicon nitride (PECVD)	4200	Strataglass, Mtn. View CA
DLC (PECVD)	2500	Tribofilm Inc., Raleigh NC
Parylene C	8000	Paratronix, Attleboro MA
Parylene C	8000	SCS, Clear Lake WI

Table 3.3: Origin and thickness of tested insulator samples

was expected to provide higher quality films. The required capacitance can be achieved with SiO_2 films as thick as 0.5 – 2.0 μm whereas the breakdown voltage at these thicknesses is several hundreds of volts. Samples of PECVD SiO_2 were obtained from Tribofilm Research Inc. (Raleigh, NC). However, all of the samples that were tested failed to insulate against electrolyte droplets.

Silicon nitride Silicon nitride (SiN) posseses many of the same benefits as SiO_2, with even higher dielectric constant and breakdown strength. In addition, SiN provides excellent scratch and chemical resistance and is highly impermeable to water. However, samples of SiN obtained from three different sources all failed under testing.

Diamond-like carbon Diamond-like carbon (DLC) is an amorphous carbon film in which some carbon atoms are bonded as in diamond. Consequently, DLC has many of the same properties as diamond including excellent scratch, wear and chemical resistance. In addition, DLC is typically flexible and biocompatible making it a desirable coating for biomedical applications. However, samples of PECVD DLC obtained from Tribofilm Research Inc. also failed under testing.

Spin-on glass Spin-on glasses (SOG) find wide use in microelectronics as diffusion sources, planarizing dielectrics, and passivation layers. A liquid precursor containing either inorganic silicates or organic siloxanes is applied to the substrate, spun at high speed, and then cured at several hundred degrees for 30 – 60 m undergoing a sol-gel transition. SOG was an attractive option because it combines the favorable electrical properties of SiO_2 with a highly planar and pinhole-free film. However, high stresses (400 – 500 MPa) generated by shrinkage of the film during curing lead to cracks in films thicker than a few thousand Å [51]. Organic SOG is less susceptible to cracking, but suffers from increased water absorption and less mechanical and electrical stability compared to inorganic SOG.

Both inorganic (Filmtronics 20A) and organic (Filmtronics 70F) SOG films of various thicknesses were applied at Duke and also failed the electrolyte droplet test.

Polyimide Polyimide is a high-temperature spin-coatable polymer that has been in commercial use for microelectronics since the 1970s [37]. Typically, a polyamic acid precursor is applied by spin-coating followed by a cure at 300 – 400 °C. Polyimide posseses a number of favorable properties, including excellent thermal stability, chemical resistance, toughness and wear resistance. Polyimide was used as an interlevel dielectric for the early prototypes. However, the minimum film thickness for this process at BMMSL was about 1.5 μm which gives a capacitance of only about 2 nF/cm^2. Since this was the minimum acceptable insulator capacitance polyimide was not tested at this time.

Parylene Parylene is the generic name for a family of crystalline para-xylylene polymers that are deposited from a vapor phase at room temperature under moderate vacuum [54][56]. This coating process results in films which are particularly conformal, uniform and pinhole-free. In addition parylene films have an excellent combination of chemical, electrical and mechanical properties. Deposition of parylene begins with sublimation of a dimer precursor under vacuum to produce a vapor which is then pyrolyzed at around 680 °C to produce reactive para-xylylene monomers (Figure 3.4). The reactive monomer vapor is then fed into a room temperature deposition chamber where it condenses and polymerizes on all exposed surfaces.

There are various types of parylene differing in the composition of their precursor molecules, but the most commonly used ones are parylene C and parylene N. Parylene C has a higher dielectric constant, and at sub-micron thicknesses, a higher breakdown voltage (Figure 3.5) than parylene N, while parylene N has superior thermal properties. Samples of parylene C were obtained from two sources and tested. Most samples demonstrated excellent insulation against the electrolyte solution with dielectric breakdown occasionally

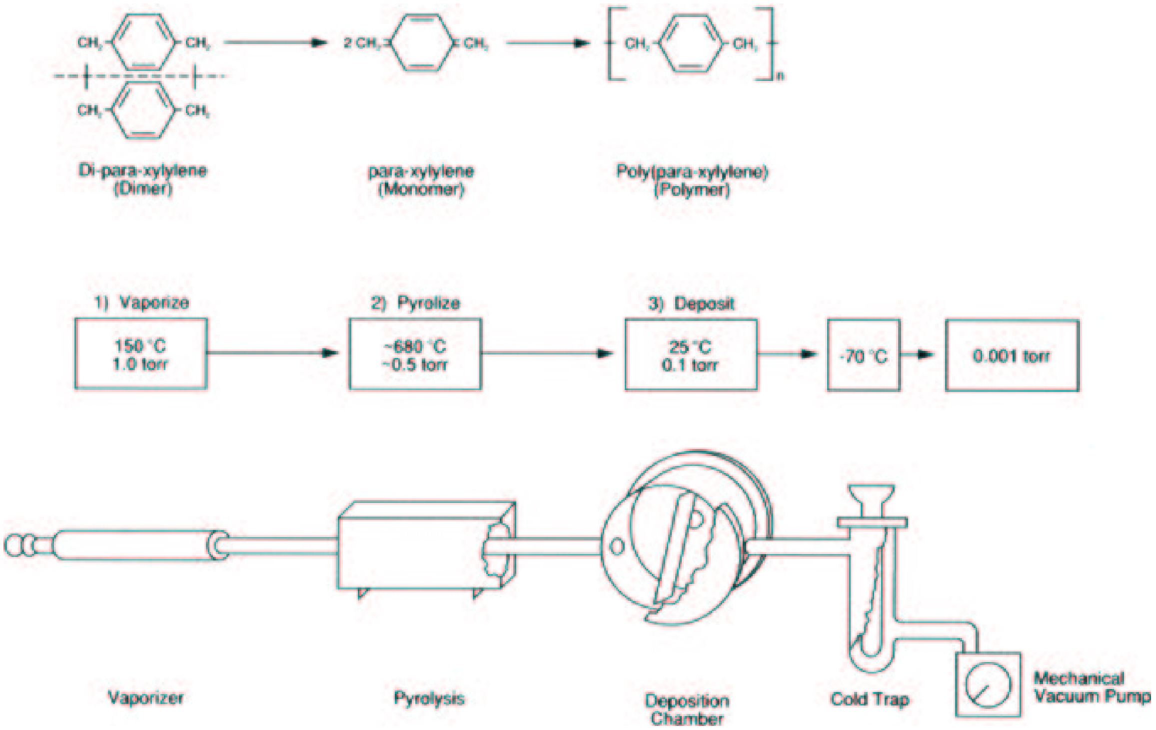

Figure 3.4: The three stage parylene deposition process. From [56]

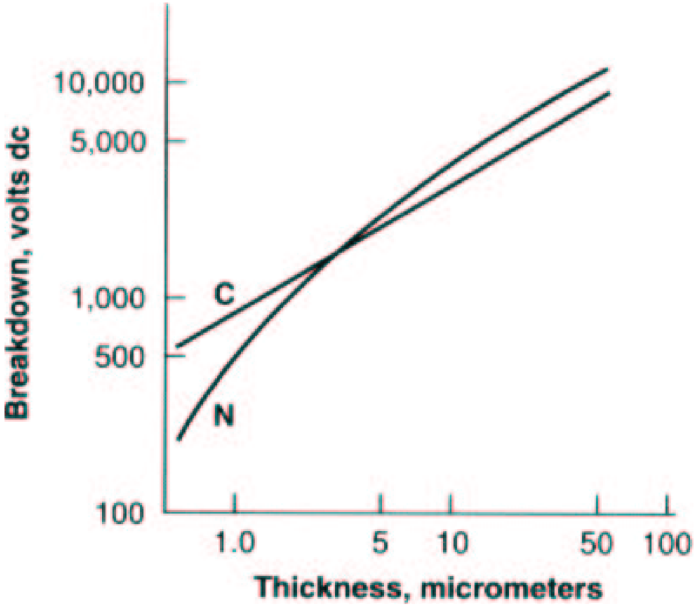

Figure 3.5: Breakdown voltage of parylene as a function of thickness and type. From [56]

occuring between 50 – 120 V. Additionally, we observed noticable electrowetting of the droplets at these voltages, although our observations and those of others [57] indicate that, due to some unknown mechanism, the electrowetting effect on bare parylene is relatively small and irreversible. Thus, parylene requires the use of a hydrophobizing top-layer which permits large and reversible electrowetting effects.

3.2.2 Electrode Hydrophobization

Recognizing that the electrode insulator material may not present an adequate surface for electrowetting it may be necessary to modify the surface character of the material. For siliceous surfaces such as SiO_2, reactive organosilanes may be used to chemically modify the surface through the covalent attachment of an organic monolayer. Alternatively, thin layers of a bulk polymer such as Teflon AF, may be applied by spin-coating or other means as part of a composite insulator structure. Silanized SiO_2 surfaces were used in the early prototypes, while thin spin-on Teflon AF films served as hydrophobization for parylene in the later devices.

Hydrophobization by Silanization

The use of organosilanes to alter the wettability of glass surfaces is a well-known technique in appled science [58][59]. We utilized two commercially available formulations for this purpose: Glassclad 18 and Glassclad 6C from United Chemical Technologies. Glassclad 18 is a monomeric octadecylsilane in a mixture of alcohols that reacts with water to form a silanol-rich prepolymer. The prepolymer then undergoes a condensation reaction with available hydroxy groups of siliceous surfaces to form a chemically bonded silicone film. Glassclad 18 was used as a freshly prepared 1% solution in water and applied using the following procedure:

- Immerse in 1% Glassclad solution for 10 s

Substrate	Untreated	Glassclad 18	Glassclad 18 (boiled 65 hr)	Glassclad 6C
BSG	41.5 ± 7.0	81.6 ± 5.8	36.4 ± 4.9	97.6 ± 1.2
SiO_2	9.9 ± 2.1	33.4 ± 4.2	75.6 ± 5.6	95.7 ± 1.8
ITO	63.0 ± 4.1	——	——	50.8 ± 0.8
SiN	66.5 ± 1.0	——	——	87.8 ± 3.7

Table 3.4: Effect of organosilane hydrophobization treatments on various substrates. Values are contact angle of the surface with deionized water in degrees.

- Rinse in deionized water for 10 s
- Cure at 110 °C for 10 m

Borosilicate glass (BSG) and sputtered SiO_2 samples were treated with Glassclad 18 and the contact angle with water was measured before and after treatment (Table 3.4). While a contact angle of 81.6° was imparted to the BSG surface, the SiO_2 surface only had an angle of 33.4° after treatment. The experiment was then repeated with samples that had been boiled in deionized water for 65 hours. It was expected that this pretreatment step would hydrolyze additional Si atoms on the surface and improve the yield of the organosilane reaction. After treatment with Glassclad 18 the contact angle of the boiled SiO_2 samples increased to $75.6 \pm 5.6°$ but the BSG samples saw a reduction in contact angle to $36.4 \pm 4.9°$.

The formulation Glassclad 6C was investigated next. Glassclad 6C is a chlorinated polydimethylsiloxane (PDMS) oligomer that is applied in a dry solvent. The terminal chlorines react with surface hydroxy or silanol groups to form a chemically bound PDMS film. Glassclad 6C was typically prepared as a 5 or 10% solution in dry hexane and applied using the following procedure:

- Immerse in Glassclad 6C solution for 1 m
- Immerse in hexane for 1 m
- Rinse with hexane for 15 s

- Cure at 110 °C for 25 m

Glassclad 6C treatment resulted in contact angles of $95.7°$ for SiO_2 and $97.6°$ for BSG. Compared to Glassclad 18, the Glassclad 6C coating was more hydrophobic, more uniform and less dependent on the type of silica surface.

Glassclad 6C was also applied to PECVD SiN and sputtered ITO films. Silicon nitride was considered as an alternative insulator to SiO_2, and ITO was considered for the ground electrode conductor. It was therefore worthwhile to determine whether these surfaces could be directly hydrophobized without an SiO_2 top-coating. Silicon nitride surfaces treated with Glassclad 6C had a contact angle of $87.8°$ while the contact angle of ITO surfaces decreased from $63.0°$ to $50.8°$ following treatment.

The Glassclad 6C coating was then investigated to determine its compatibility with certain processing steps. If the substrate is to be patterned following hydrophobization (i.e. for opening vias), the coating must be able to withstand photoresist baking as well as developing and stripping processes. The treatments tested included immersion in acetone, methanol, and AZ-300T photoresist stripper (Hoechst Celanese), baking at 115 °C, boiling in water, immersion in isopropanol, and wiping with a tissue (to test adhesion and mechanical strength). In each case the contact angle of a hydrophobized sputtered SiO_2 sample was measured before and after the treatment and the difference is recorded in Table 3.5. Only wiping and AZ-300T immersion had a significant effect on the contact angle. Since methanol and acetone alone are usually sufficient for the removal of photoresist, these results suggest that the coating should be compatible with photoresist processing.

Hydrophobization with Teflon AF

Teflon AF (Dupont Fluoropolymers) is a family of amorphous fluoropolymers based upon PDD[2] copolymers that possesses many of the usual advantages of fluorinated polymers

---

[2] 2,2-bistrifluoromethyl-4,5-difluoro-1,3-dioxole

Treatment	$\Delta\theta_{H_2O}$ **(degrees)**
Bake 115 °C (30 m)	+1.8
Boil (30 m)	-2.7
Isopropanol immersion (10 m)	-1.2
Methanol immersion (10 m)	-1.7
Acetone immersion (10 m)	-0.4
AZ-300T immersion (10 m)	-12.4
Wipe with tissue (15 s)	-5.3

Table 3.5: Effect of various treatments on Glassclad 6C hydrophobic coating

[55]. These advantages include excellent chemical resistance, low surface energy and high temperature stability. Unlike semicrystalline fluoropolymers, which are only soluble under specialized conditions, Teflon AF is readily soluble in many different perflourinated solvents at room temperature. As a consequence, it can be applied as a spin-coated film ranging in thickness from tens of nm to several μm. Typically, Teflon AF is applied as a 1 – 5 wt% solution in “Fluorinert” (3M Specialty Fluids) perfluorinated solvents and cured at temperatures of up to 330 °C. Various grades are available, but the most commonly used are Teflon AF 1600 and Teflon AF 2400, where the number indicates the glass transition temperature of the polymer (160 and 240 °C respectively).

Teflon AF’s dielectric constant of 1.9 is the lowest of any known polymer, making it a candidate for next-generation interlevel dielectrics [53], but a poor choice as a capacitor dielectric. For this reason Teflon AF was not considered as a primary insulator film. Additionally, Teflon AF films are known to be characterized by microvoids and micropores which would be expected to reduce its effectiveness as an insulator in a liquid environment. However, as a thin top-coating Teflon AF provides an excellent hydrophobic surface with high contact angle (104°) and exceptionally low hysteresis (2 – 5°). Furthermore, as a bulk film, Teflon AF, unlike organosilanes, can be applied to many different types of surfaces using a single process.

Teflon AF 1600 films were applied by spin-coating dissolved resin ranging in concen-

Conc. (wt. %)	**Thickness (Å)**
6.0	10,000
3.0	3000
1.0	600

Table 3.6: Concentration versus thickness of spin-coated Teflon AF 1600 films

tration from 1 – 3 wt.% in FC-75. The procedure used was:

- Spin-on Teflon AF solution at 3000 RPM for 20 s
- Air dry for 5 – 10 m
- Bake at 110 °C for 10 m
- Bake at 170 °C for 10 m
- Bake at 330 °C (or highest possible) for 10 m

When applied over parylene, the final 330 °C bake was replaced with an additional 10 minutes at 170 °C to avoid thermal degradation of the polymer. Typical film thicknesses at several concentrations of Teflon AF for this process are listed in Table 3.6.

3.2.3 Electrode Conductor

In order to visualize the operation of the device it is important that the top-plate conductor material be semi-transparent to visible light. Initally, thin sputtered Au films (100 – 200 Å) were investigated, but were found to have unacceptably low transmission. Even thinner sputtered or evaporated metal films of thickness 50 – 100 Å typically provide optical transmittance of less than 60% [60] with sheet resistances greater than 20 Ω/sq. [61]. Although anti-reflective coatings can be used to improve the transmittance it was felt that a suitable trade-off among process complexity, transmittance and sheet resistance could not be found for thin metal films in this case. By contrast, indium-tin-oxide (ITO) films of 1000 – 2000

Å thickness typically have $> 80\%$ transmittance in the visible spectrum with sheet resistances of less than 10 Ω/sq. Thus, ITO coated borosilicate glass (Delta Technologies) was used for the top-plate ground electrode.

The control electrodes on the bottom-plate have no such transparency requirements and conventional thin metal films were used for these conductors. Initially, 1500 Å sputtered Au films with a thin Cr adhesion layer were used for the control electrodes. In order to reduce the process complexity, the Au film was later abandoned in favor of a single 1000 – 2000 Å Cr layer. While Au is substantially less resistive than Cr (2.1 vs. 11.8 μm·cm), no direct current flow should be present in the device and fairly high resistances can be tolerated. A further advantage of Cr metallization is the widespread availabilty of 5" Cr/glass plates and processes for these plates since these are common substrates used for photomask fabrication. In fact, some devices were fabricated directly on E-beam written or optically printed photomask substrates.

3.3 Design and Fabrication of Later Prototypes

Having addressed the materials issues, a new series of prototypes were designed and fabricated with the film structure shown in Figure 3.6. The Cr control electrodes are insulated with approximately 8000 Å of parylene C with a thin ~ 600 Å top-coat of Teflon AF. The ground electrode is formed by a transparent ITO film with a matching Teflon AF top-coat. The Teflon AF film does not electrically insulate the top electrode from the liquid, but serves only to hydrophobize the surface.

To further reduce complexity a single-layer metal process requiring only one mask layer was adopted for these prototypes. Because of the constraints of wiring in a single layer the designs consisted primarily of linear arrays of interdigitated electrodes, although some 2 x 7 arrays were also designed and fabricated. Several die layouts for these prototypes are shown in Figure 3.3. The electrode pitches ranged between 1.5 mm and 150 μm

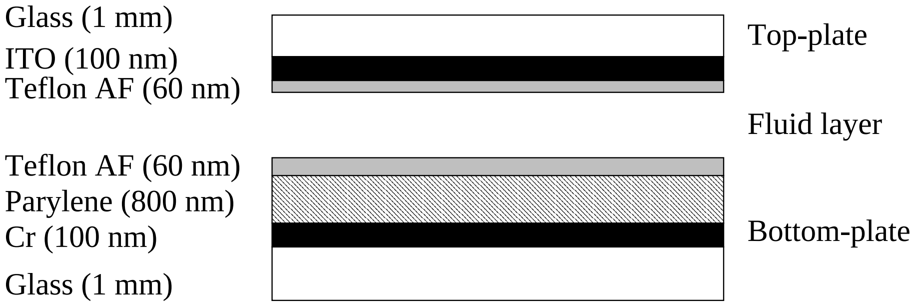

Figure 3.6: Cross-section of microactuator film structure for later prototypes (not to scale)

with a minimum 2.5 μm feature. The simplified process required only three steps: the Cr wiring/electrode layer was first deposited and patterned, parylene was then deposited using wafer-tape to mask the contacts, and finally Teflon AF was applied to both top and bottom plate surfaces. The yield of the process was virtually 100% and the results of testing are described in the following chapters.

3.4 Chapter Summary and Conclusions

A prototype electrowetting chip consisting of a 6 x 7 array of 150 μm pitch electrodes was designed and fabricated. However, because of processing problems and the failure of the SiO_2 insulation against electrolyte, the initial prototypes did not yield workable devices. After evaluating several alternative insulator materials, parylene C emerged as the most suitable choice for this application. However, the electrowetting performance of parylene is relatively poor and a top-coat of Teflon AF was required to effect large and reversible changes in contact angle. An alternative top-coat may consist of a thin layer of SiO_2 whose surface has been modified with organosilanes. Such treatments provide a great deal of control over surface wetting characteristics and are important for the functionalization of certain surfaces, as for example, in solid-phase synthesis of biopolymers. A new chip design utilizing the parylene/Teflon AF insulation system was fabricated with a simplified

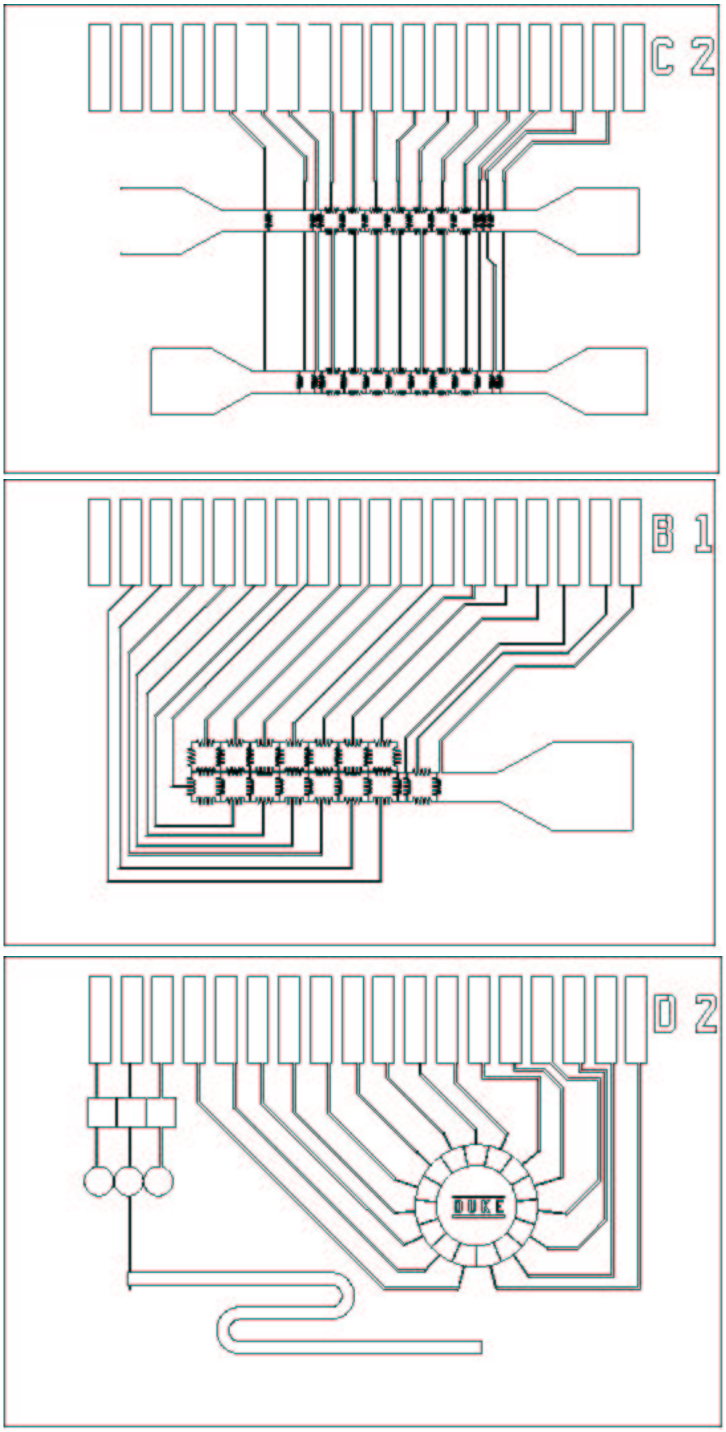

Figure 3.7: Die layouts from the single-metal-layer prototypes (3X actual size). The top die (C2) was fabricated with electrode pitches ranging 0.15 to 1.5 mm.

single-metal-layer process that required only one mask level. The improved process and materials resulted in functioning electrowetting chips suitable for experimental investigations.

Chapter 4

Experimental Results - Droplet Transport

Functional microactuator chips were fabricated as described in the previous chapter. Side and top views of a droplet transfer between two electrodes are shown in Figure 4.1. The side-view droplet is in air, while the top-view droplet, viewed through the ITO electrode, is in silicone oil media. Both droplets are 900 nl of 100 mM KCl solution. Droplets were readily transported in both air and silicone oil media, although the threshold voltage required to initiate droplet motion was considerably higher in air (40 – 50 V) than in oil (10 – 20 V). Transfer of droplets between adjacent electrodes is a fundamental operation of digital microfluidic systems based upon electrowetting. The remainder of this chapter

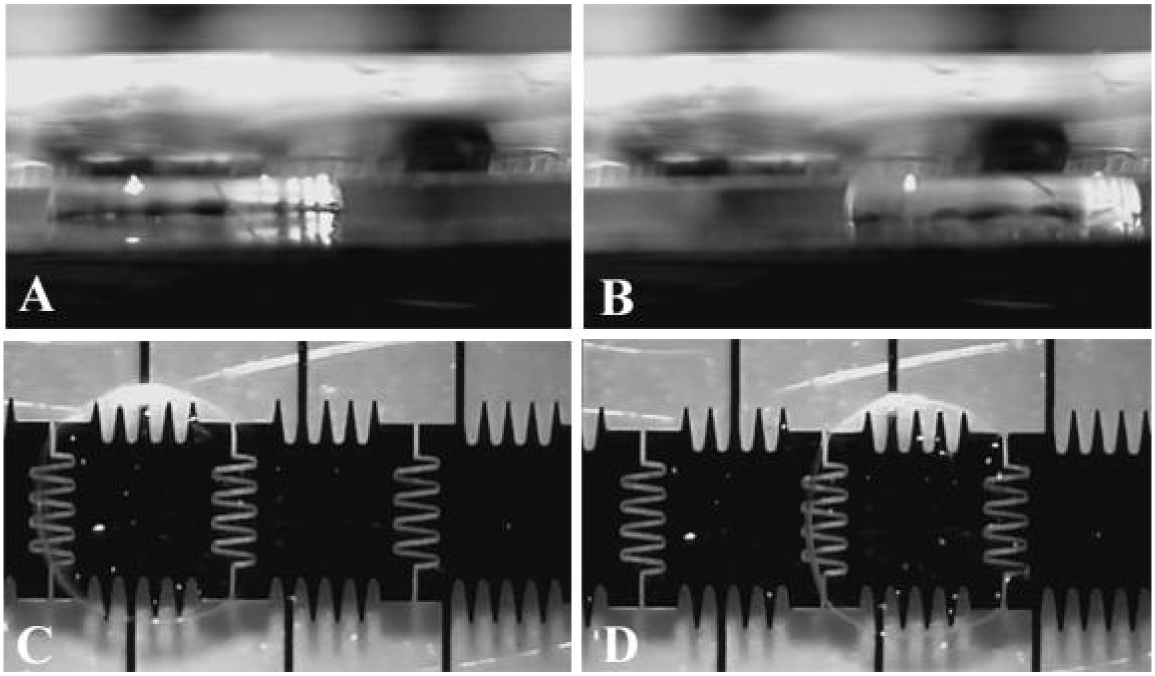

Figure 4.1: Side (A & B) and top (C & D) views (at 66 ms intervals) of droplet transport between two electrodes

is an experimental study of the dynamics of this important process. We first describe the experimental setup and techniques for determining droplet velocities. We then address some significant experimental difficulties that were present throughout this work and which affected the quality of data we were able to obtain. Finally, we present the results of our experiments and discuss them in the context of physical descriptions of wetting behavior.

4.1 Experimental Methods

4.1.1 Experimental Setup

The experimental setup for testing the electrowetting chips is depicted in Figure 4.2. A 90 MHz Pentium personal computer controlled a custom-made electronic unit capable of independently switching up to 50 outputs between ground and the output of a 120 V dc power supply (Agilent 3612A). The outputs of the electronic unit were connected to a custom-made stage assembly. The chips were mounted in a holder with spacers of known thickness on either side to provide stand-offs for the top-plate. A modified electronic test clip (Pomona Electronics) was used to contact the row of bond pads on the chip and to secure the chip against the holder. The top-plate was positioned across the spacers and held in place by clips on either side to provide a fixed gap between the chip and top-plate. The electrolyte was typically dispensed onto the chip using a micropipettor prior to positioning the top-plate. The filler oil was introduced after the droplet and top-plate were in place by dispensing it at the edge of the plates and allowing it to wick into the gap.

Images were obtained with an industrial microscope (VZM 450i, Edmund Industrial Optics) and color CCD camera (Sony XC-999). The field of view of the microscope was 1.4 – 8.8 mm. Images were either captured directly to a PC using a frame grabber (Miro DC30, Pinnacle Systems) or were videorecorded with a super-VHS videocassette recorder (JVC-S4600) for later analysis.

The electronic controller unit essentially consisted of an address decoder connected to

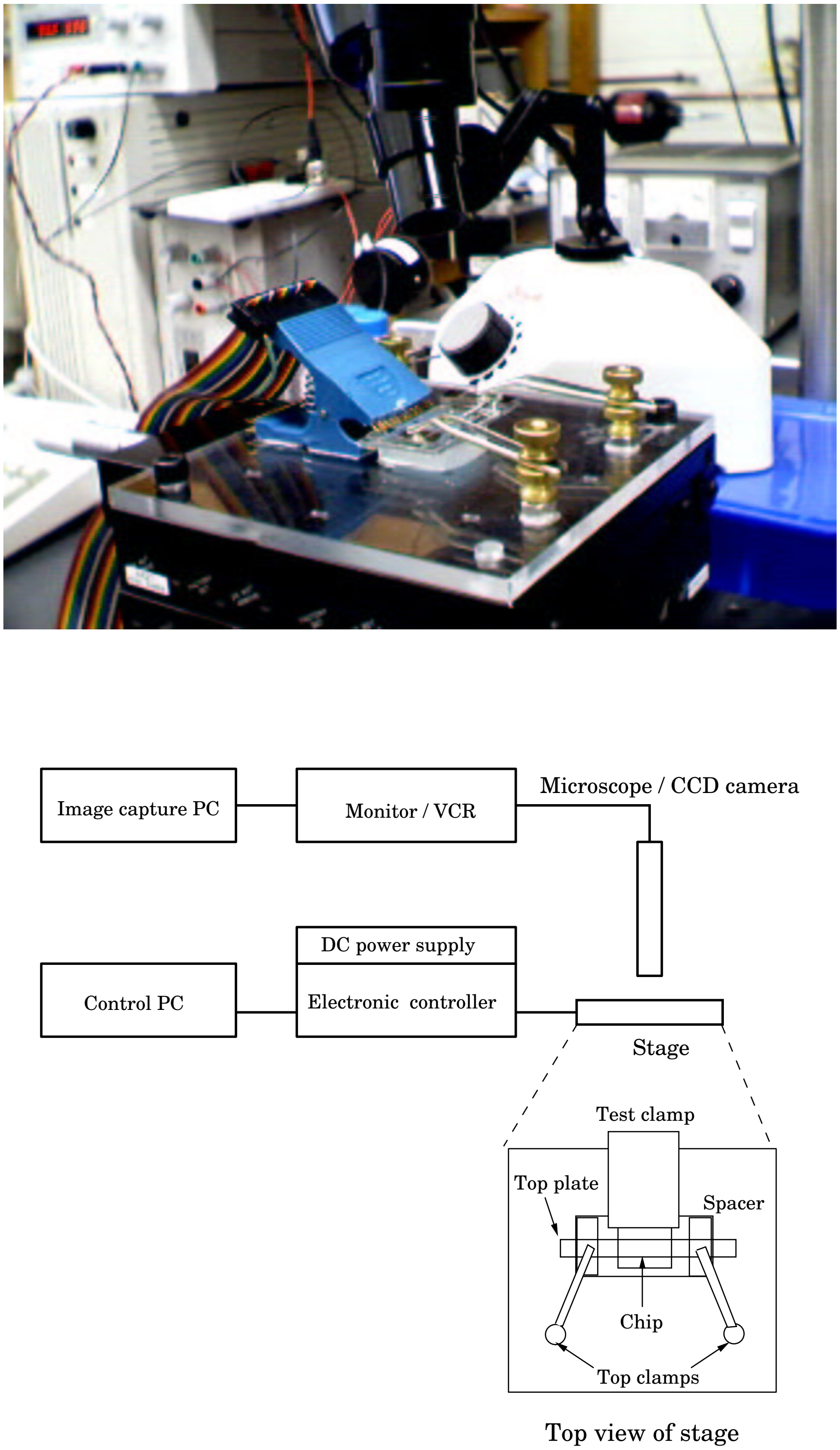

Figure 4.2: Photograph and diagram of the experimental setup

a bank of flip-flops which in turn drove a bank of power transistor switches. The power transistors were rated for up to 100 V and 1.3 A. The unit was controlled through the parallel port of the control PC using a set a predefined byte-codes including *on* and *off* codes for each of the 50 channels, as well as codes for setting or reseting all outputs and enabling or disabling the high-voltage output. Control software was written in C with in-line x86 assembly code and ran under MS-DOS for real-time control.

Three factors determine the maximum switching rate of the control system: the output voltage rise time, the parallel port write speed, and the speed of software execution. The output voltage rise time was measured and found to be approximately 6 μs over the range 0 – 100 V. The parallel port was configured in "standard parallel port" mode on a 1.3 MHz ISA bus. Each switching event therefore required three parallel port write cyles or 2.3 μs to execute. The combined effect of the parallel port and software execution latency was experimentally determined by comparing programmed and actual pulse rates at several different frequencies. With a typical output control subroutine consisting of about 20 lines of C code, the latency was approximately 10 μs. The total delay of 16 μs gives a maximum possible switching frequency of 62.5 KHz, with 95% timing accuracy below 3125 Hz and 99% accuracy below 625 Hz.

4.1.2 Measurement of Droplet Transfer Rates

In considering the design and operation of digital microfluidic systems, a fundamental parameter of interest is the maximum rate at which fluid units can be transferred between adjacent cells. In the present design this frequency f_{max} is the inverse of the time t_{tr} required for a droplet a traverse a single electrode. The characterization of f_{max} under different experimental and design conditions was the primary objective of this study of droplet transport.

Frame Counting Method

For relatively slowly moving droplets, transfer rates were determined through video analysis. Moving droplets were videorecorded and transfer times were subsequently measured by counting video frames (30 frames/s) between the initiation of droplet motion and the crossing of the far edge of the destination electrode by the leading edge of the moving droplet. Due to the limited frame rate of the camera this method was not considered to be reliable for determination of rates greater than about 8 Hz. This method was primarily used in the earliest experiments and for certain special cases such as droplets moving in viscous oil.

Constant Switching Rate Method

For measurement of more rapid movement, an indirect voltage balancing technique was used. A voltage pulse was programmed to oscillate across a line of three or four adjacent electrodes at a programmed switching frequency f_s. The magnitude of the voltage was then adjusted until the movement of the droplet was able to fully track the position of the voltage pulse. The minimum voltage at which the droplet was observed to move smoothly between the outside edges of the outer electrodes was taken to be the threshold voltage V_t for continuous travel at the rate f_s. The rate f_s is equivalent to f_{max} at the voltage V_t and $1/f_s$ is the electrode transit time t_{tr}. The transition from weakly tracking to fully tracking movement of the droplet was usually quite abrupt, occurring over a 0.1 – 0.2 V range, which was close to the output precision of the power supply.

In many cases the voltage required to initiate tracking of the droplet was slightly (< 3 V) higher than the voltage required to sustain it. In these cases, the voltage was first increased above the threshold required to initiate tracking and then reduced to the lower threshold to determine V_t. This effect was believed to be due to geometrical effects arising from elongation along the axis of motion of the moving droplet. Thus, a droplet already in motion elongates and reaches the next electrode sooner than a droplet activated from a relaxed position. For larger droplets at higher velocities this elongation complicated the measurements because it was not always apparent whether a droplet had moved or merely stretched across the adjacent electrode. Furthermore, due to observer and camera limitations, this method was not considered to be very reliable for rates greater than about 50 Hz in any case.

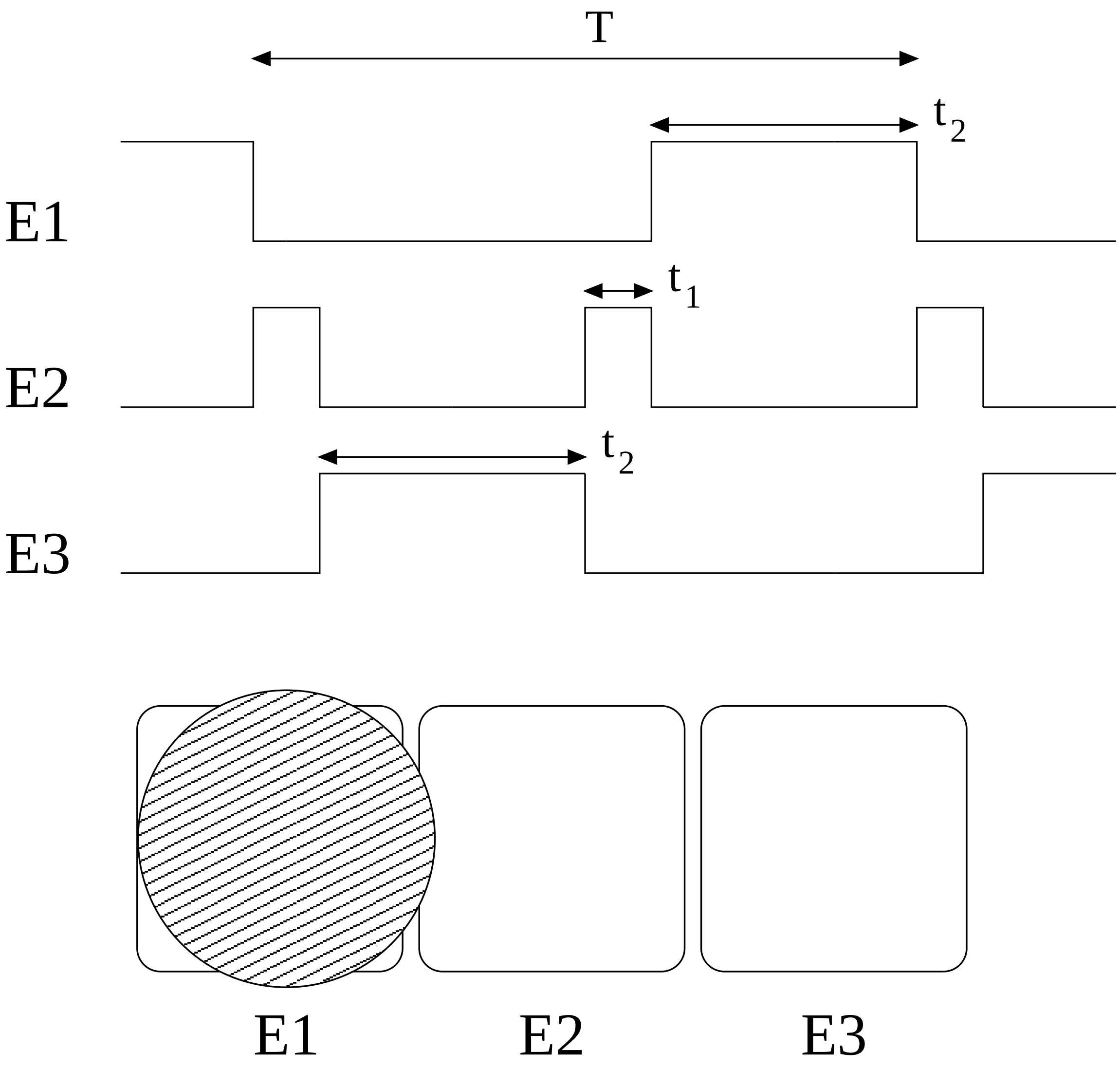

Figure 4.3: Constant oscillation rate method for measuring droplet velocites

Constant Oscillation Rate Method

For more precise determination of faster rates, the previous method was modified so that the visual determination was independent of the switching rate. In this case the total period T of the droplet oscillation was fixed (usually 1 s), and the electrodes were allowed to switch at different rates. The interior electrodes were pulsed on for a time t_2 while the end electrodes were pulsed on for a time $t_1 > t_2$ with $T = 2(t_1 + nt_2)$, where n is the number of interior electrodes. This voltage protocol for a measurement using three electrodes is illustrated in Figure 4.3. The droplet can only be transferred between the terminal electrodes when $t_2 > t_{tr}$. As in the previous method, the voltage was balanced to determine the threshold for continuous transfer with $f_s = 1/t_2 = 1/t_{tr} = f_{max}$.

One deficiency of this method is that when only three electrodes are involved as illustrated here, charging of the middle electrode could allow the droplet to sometimes oscillate when $t_{tr} > t_2$. For this reason, four or more electrodes (two interior) were usually preferred for these measurements. We also note that these measurements may tend to underestimate the average droplet velocity as they are most sensitive to the slowest transfer in the each pathway. Transfer rates may vary slightly depending on electrode variations or the direction of transfer, especially when particulate contamination or significant surface heterogeneity is present. In principle, there is no upper frequency limit for this method and it was used to measure rates in excess of 2 KHz.

4.2 Experimental Limitations

4.2.1 Droplet Volume Control

Evaporation of the droplets in air affected our ability to precisely control and maintain droplet volumes during the course of experiments. Furthermore, evaporation of liquid alters the salinity of the droplet and may result in slight variations of other properties such as surface tension as well. We studied the evaporation of these droplets to assess the significance of the problem and to determine appropriate time scales for conducting experiments in air. We performed a simple experiment, under typical laboratory conditions, where droplets of deionized water were dispensed onto a Teflon AF surface and allowed to evaporate in air. Top-view images of the droplet were captured and later analyzed to determine the diameter of the droplet as a function of time. Neglecting hysteresis effects, the cube of the droplet diameter is presumed to be directly proportional to the volume.

Droplets with initial nominal volumes of 1.0 μl and 10.0 μl were studied. The smaller volume represents a typical size for droplet transport experiments, while the larger volume represents a typical size for contact angle or electrowetting measurements. Each droplet was tested under both covered and uncovered conditions. For the smaller droplet the cover was a 1 cm wide Teflon AF coated strip of glass positioned 0.3 mm above the bottom surface (thus sandwiching the droplet), while the cover for the larger droplets was an inverted 50 mm diameter polystyrene petri dish to determine if this simple arrangement could reduce evaporation. The ambient temperature and humidity over the course of the experiments was in the range 23 – 24 °C and 37 – 41 % relative humidity respectively.

The cube of the droplet diameter, normalized with respect to the initial measurement, as a function of time is plotted in Figure 4.4. The 10 μl droplets lose 10% of their volume within 5 – 10 m. When making volume sensitive measurements of these droplets in air, this should be considered a maximum reasonable experimental duration. We note that even simple contact angle measurements are sensitive to volume loss both on theoretical (contact angle hysteresis) and practical (optical geometry/gravitational effects) grounds. The smaller 1.0 μl droplets evaporate 10% of their volume within 1 – 3 m. Even when oil is used in the system to prevent evaporation, this amount of time is typically required to initially dispense and position the droplet and fill the gap with oil. Furthermore, the micropipeted volumes are 2.5 – 12.0 % inaccurate in the sub-microliter range according

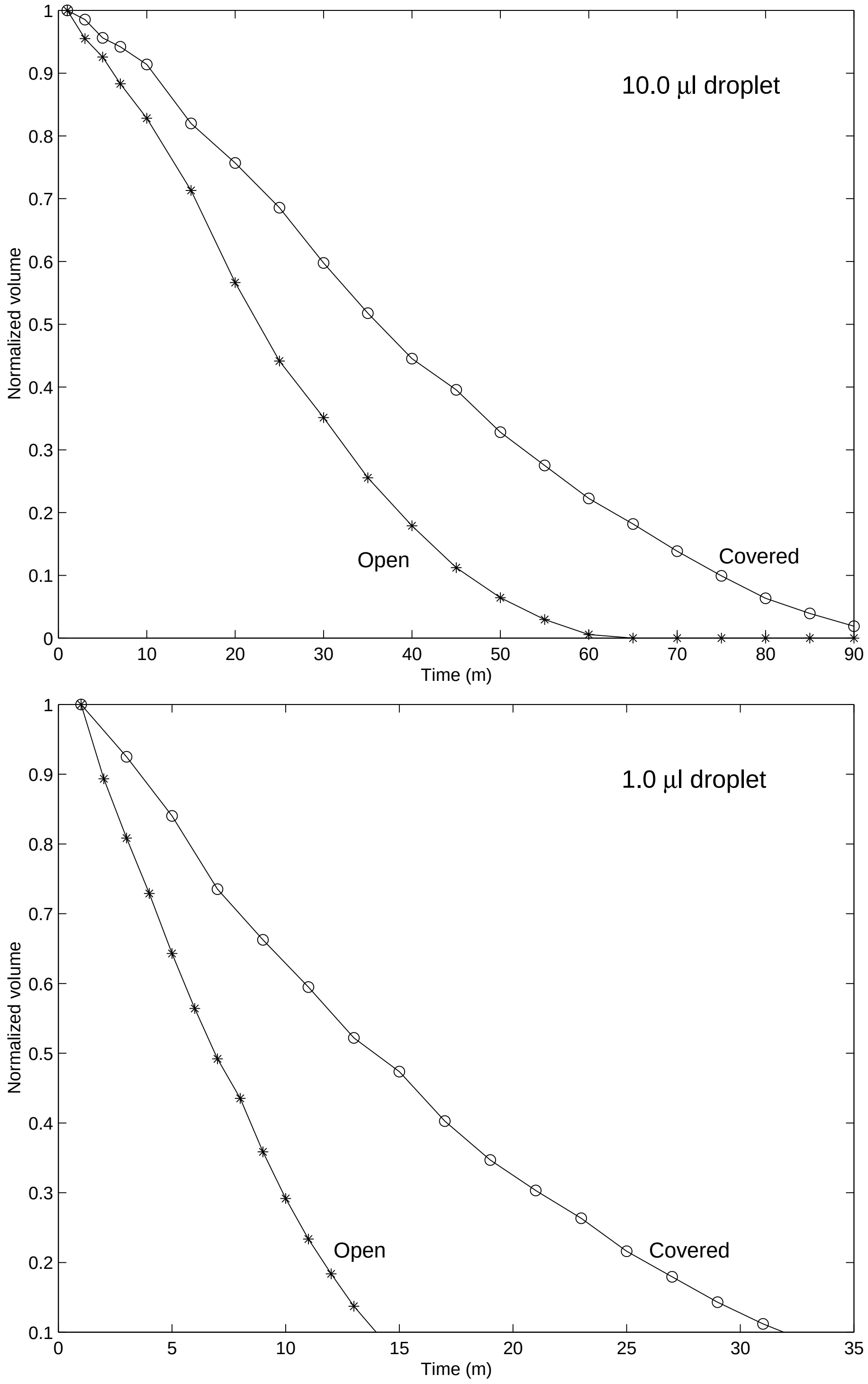

Figure 4.4: Evaporation of 10 μl (top) and 1.0 μl (bottom) water droplets from a Teflon AF surface in air as a function of time

to the manufacturer of the pipettor (Eppendorf Reference, 0.1 – 2.5 μl) we use for these droplets.

Thus, we were not able to precisely control the volume of droplets across multiple experiments or during the course of single experiments in air. We do note that when immersed in oil, droplet volumes were constant over periods as long as several days. When the gap height is known, the diameter of the relaxed droplet footprint provides an estimate and means for verification of the actual droplet volume. However, the gap height is somewhat sensitive to the cleanliness and uniformity of the glass surfaces. For example, a 10 μm diameter particle between the top-plate and holder or between the chip and holder might have resulted in 1 – 10 % variation in the gap height and corresponding error in the estimated droplet volume.

4.2.2 Insulator Reliability

A more serious experimental concern was the reliability and stability of the electrode insulation. The insulation was often observed to degrade over the course of an experiment, producing surface energy variations across the surface. It is unclear whether this surface energy change is due to injected charge in the insulation or to chemical rearrangement of the polymer surface. We find that when the applied voltage is removed in these cases, the droplet tends to drift towards a preferred location on or between two electrodes. In some cases 10 – 15 V applied to an electrode adjacent to one of these regions was necessary to simply compensate for this drifting motion. No change in the location or magnitude of the effect was observed after changing the droplet, oil and top-plate, indicating that the effect is present in the electrode insulation. We were not able to discern any clear patterns in the onset, strength or physical location of this effect although both the magnitude and time of the voltage contribute to it. At higher voltages (60 – 100 V) electrode insulation degraded quite rapidly and for this reason testing at these voltages was generally limited. One consequence of this was that at high voltages and velocities, droplets often fragmented due to the opposing force of voltage on one electrode and high-energy regions of the insulation on adjacent electrodes.

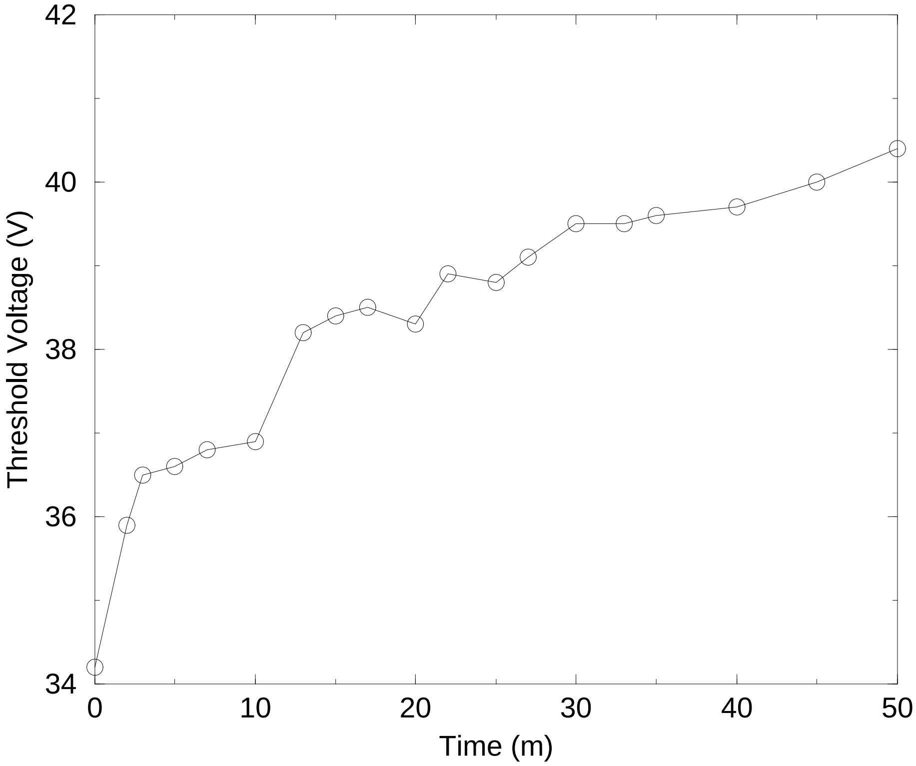

Figure 4.5: Threshold voltage rise associated with degradation of the insulation

Figure 4.5 shows the result of an experiment in which the threshold voltage for 10 Hz droplet transfer (constant switching rate method) was periodically determined for a continually oscillating droplet. We observe a time-dependent increase in the threshold voltage arising from the insulator degradation effect. Since the measured threshold voltage depends on the slowest electrode transfer in the sequence, it is very sensitive to any heterogeneity along the flow pathway. We attempted to minimize the effect of this instability on our experimental data by several means. First, we reduced the total time and voltage magnitudes in our experiments as much as possible. Secondly, a new chip or portion of a chip was usually dedicated to each series of measurements, particularly if high voltages had been previously applied. Finally, the first members in each series of measurements were remeasured at the conclusion of the each experiment to determine whether significant threshold shifts had occured. However, despite these safeguards, degradation of the insulation was a serious source of uncertainty in our measurements.

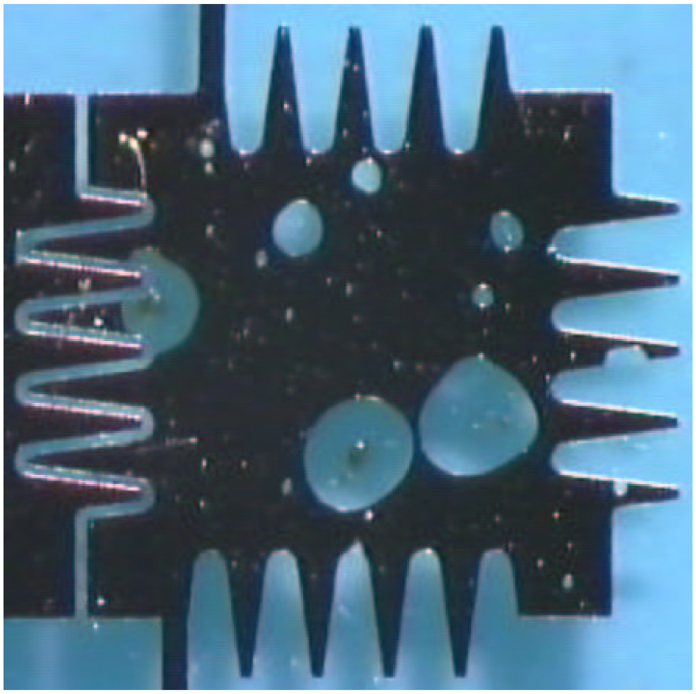

Figure 4.6: Disintegration of a control electrode due to dielectric failure

Dielectric failure of the insulator also presented certain experimental difficulties. The thickness uniformity and dielectric strength of the parylene films were generally less than advertised. Parylene is primarily used as an insulator for circuit boards, biomedical implants or other applications requiring films thicknesses of tens of μm. Since commerical parylene deposition processes and equipment are usually optimized for these conditions we were not able to obtain consistently high quality sub-micron films. Destructive dielectric breakdown was sometimes observed at voltages as low as 50 V. Many devices exhibited a low voltage failure mode, presumably due to pinhole defects, that resulted in slow disinte-

Parameter	Range or conditions
Gap height, h	0.19 – 1.04 mm, with $L = 1.5$ mm and $D/L \approx 1.3$
Droplet diameter, D	1.31 – 2.18 mm, with $L = 1.5$ mm and $L/h \approx 5$
Electrode pitch, L	0.15 – 1.50 mm, with $L/h \approx 5$ and $D/L \approx 1.3$
Electrode shape	interdigitated, square, circular, wedge
Medium type	air, silicone oil
Droplet viscosity	1.0 – 58.4 cP
Oil viscosity	0.8 – 9.4 cP
Droplet volume, V_D	3 nl – 3 μl
Velocity, v	0 – 10 cm/s

Table 4.1: Parameter space for droplet dynamic investigations

gration of the electrodes as illustrated in Figure 4.6. This problem was often more insidious because its effects only gradually became apparent during the course of an experiment.

4.3 Effect of System Parameters on Droplet Transport

The effect of varying certain system parameters on droplet transport rates was studied. Both geometrical parameters, such as droplet size, system scale, and electrode shape as well as liquid and interfacial properties such as liquid viscosity and type of filler fluid were investigated. The parameter space that was explored is summarized in Table 4.1. For geometrical manipulations, the standard liquid system was a 100 mM KCl solution droplet in 1 cSt. silicone oil, while for liquid manipulations, the standard geometry was a 900 nl droplet with $L = 1.5$ mm (interdigitated shape), $h = 0.31$ mm and $D = 1.9$ mm. Except when otherwise indicated, these parameters should be assumed for the data presented throughout this section.

The droplet volumes studied ranged from about 3 μl to 3 nl. To minimize voltage-induced degradation of the insulation, the voltage range was typically limited to 0 – 60 V, which produced droplet velocities of 0 – 10 cm/s. Droplet transfer rates were determined using one or more of the techniques previously described. In some cases, transfer characteristics were compared over the full range of voltages and velocities, while in others, comparison was made at a single point only (typically 10 Hz or 1.5 cm/s). The polarity of the control electrode voltage was always positive with respect to the top-plate electrode. We initially conducted on experiment to determine if there was a voltage-polarity effect on droplet transfer rates, but as can be seen in Figure 4.7 no dependence on polarity was observed. We also note that the only electrolyte we studied was 100 mM KCl. However, we observed similar results with droplets of deionized water, so it appears unlikely that testing of intermediate concentrations would produce any different results. Furthermore, both theoretical and experimental studies consistently report that there is no effect of ion type or concentration for the electrowetting effect on insulators [41][43][44].

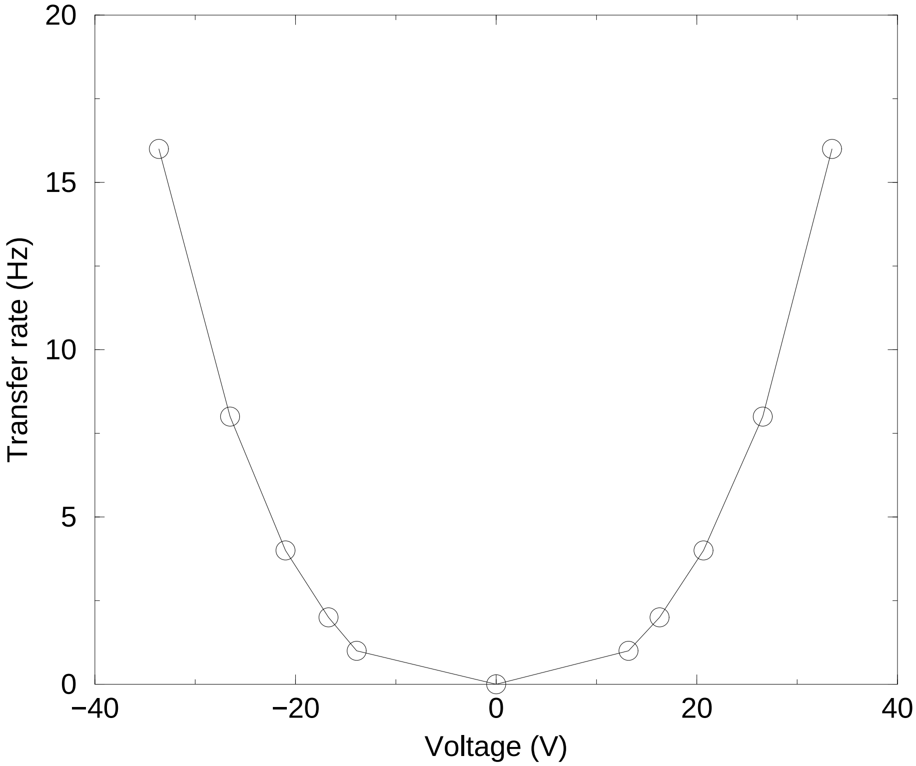

Figure 4.7: Effect of voltage polarity on transfer rates

h **(mm)**	**Aspect (**L/h**)**	**Volume (**μ**l)**	V_{th}**(V)**
0.19	7.9	0.57	34.5
0.30	5.0	0.90	29.1
0.57	2.6	1.71	27.8
1.04	1.4	3.12	26.9

Table 4.2: Effect of varying the gap height on the 10 Hz threshold voltage

4.3.1 Effect of Gap Height

The effect of varying the gap height h on droplet transport was investigated. In each case, the droplet volume V_D was adjusted to maintain a constant droplet diameter. Thus, V_D varied linearly with h while the system aspect ratio $A = L/h$ varied inversely. The threshold voltage for 10 Hz travel on 1.5 mm pitch arrays in silicone oil was determined for four values of h. Results are shown in Table 4.2 and Figure 4.8. A sharp increase in threshold voltage was observed for $A > 5$ while relatively little variation was observed at lower ratios. It is interesting to note that even as the droplet mass and surface area (for viscous drag) are increased by a factor of 5.5, V_t is reduced by over 20%. Furthermore, the maximum tested volume of 3.1 μl is comparatively large for a “microfluidic” actuator. At a transport frequency of 50 Hz, such a volume could provide an average liquid flow rate of almost 10 ml/m. This far exceeds the capabilities of even the best membrane-base micropumps [62].

At the highest aspect ratios ($A = 7.9$) droplet outlines were observed to be slightly non-circular at rest, and to deform markedly in response to the applied voltage. While at intermediate values ($A = 5.0$) droplet contours were usually highly circular at rest but deformed moderately when traveling at velocities greater than about 1 cm/s. The tallest droplets ($A = 1.4$) were not observed to deviate from their rounded shape even at relatively high velocities (> 5 cm/s).

The differing tendencies of the droplets to deform can be understood in terms of the relative energy cost of a non-minimal shape as a function of the energy-per-length (meniscus height) of the perimeter of that shape. The relative deformability of the droplets may

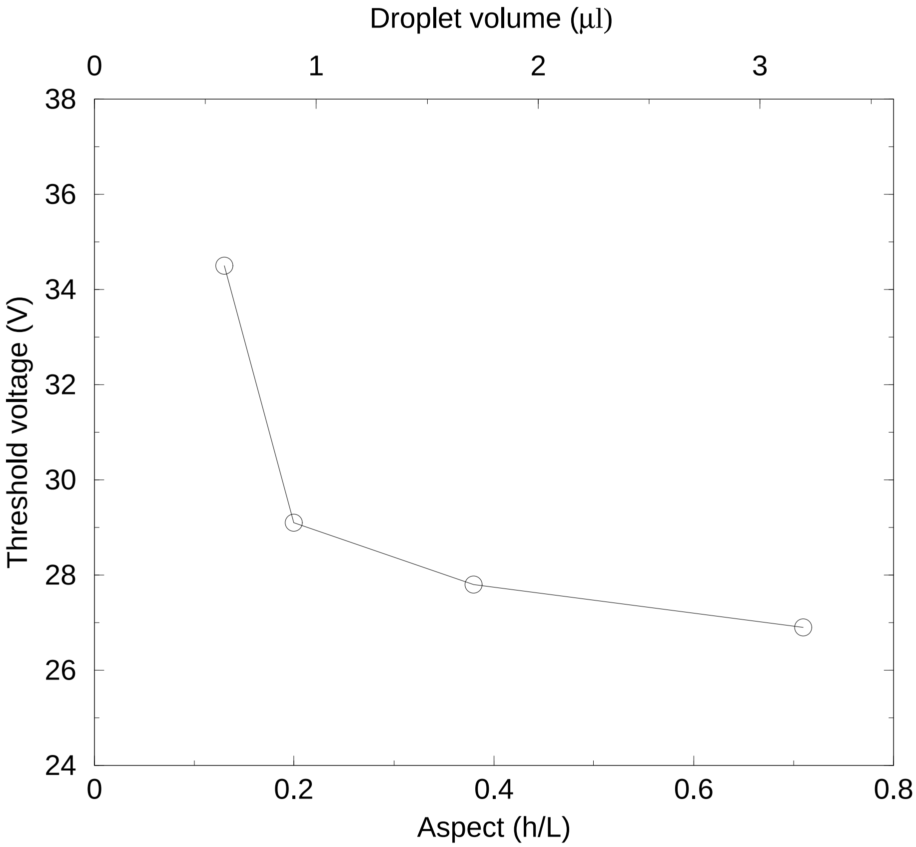

Figure 4.8: Effect of varying the gap height on the 10 Hz threshold voltage

D (mm)	Ratio (D/L)	Volume (μl)	V_{th}(V)
1.31	0.87	0.42	55.0
1.50	1.00	0.55	37.0
1.58	1.05	0.61	35.1
1.77	1.18	0.76	29.3
2.00	1.33	0.97	30.3
2.18	1.45	1.16	31.5

Table 4.3: Effect of varying the droplet diameter on the 10 Hz threshold voltage

explain the larger voltages required at higher aspect ratios. Thinner droplets may deform and stretch in response to electrowetting forces to a larger degree than taller droplets which are constrained to respond uniformly by translation. Thinner droplets are also more likely to be affected by contamination and surface heterogeneities. Furthermore, the method used here to determine transfer rates is sensitive to the slowest transfer in each cycle. Thus larger dynamic variations due to less regular behavior of the droplet might also tend to result in a higher measured threshold voltage.

4.3.2 Effect of Droplet Diameter

The effect of the droplet diameter D was studied by varying the droplet volume within a fixed gap height. The threshold voltage for continuous 10 Hz travel across 1.5 mm pitch electrodes with a 0.31 mm gap in silicone oil was determined for volumes ranging from roughly 400 – 1200 nl and droplet size ratios $B = D/L$ ranging from 0.9 – 1.5. Results are shown in Figure 4.9 and Table 4.3.

Smaller droplets require higher voltages due to the reduced overlap between the droplet and adjacent electrode. From the layout it was determined that 1.20 mm or $0.8L$ is the maximum diameter of a droplet concentric with the 1.5 mm interdigitated electrode that does not overlap any portion of the adjacent electrodes, and thus represents a presumed minimum transportable droplet size for these electrodes. At 1.84 mm ($1.23L$) the droplet completely overlaps the middle teeth, while at 2.00 mm ($1.33L$) all of the electrode's teeth

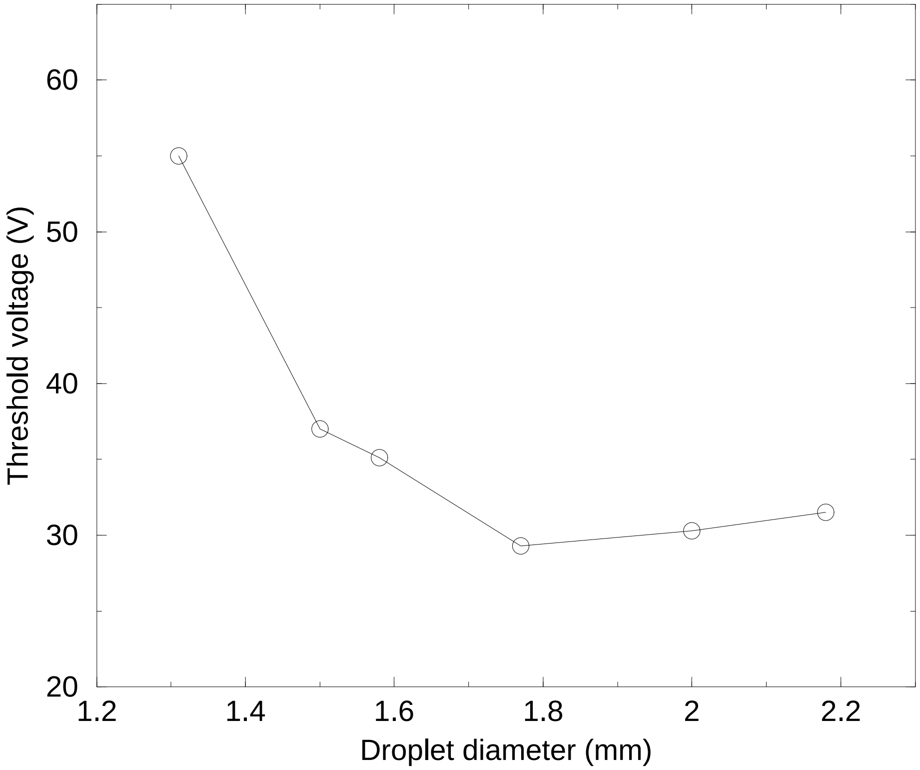

Figure 4.9: Effect of varying the droplet diameter on the 10 Hz threshold voltage

Pitch L (μm)	**Gap h (μm)**	**Aspect (L/h)**	**Vol. (nl)**
1500	300	5.0	900
1200	250	4.8	478
900	190	4.7	204
600	120	5.0	57
300	65	4.6	8
150	88	2.3	3

Table 4.4: Electrode sizes tested and assoicated gap height, aspect ratio and droplet volumes

are circumscribed by the droplet. There appears to be a minimum threshold voltage around 1.8 mm, while for droplets larger than this, the effect of the relatively small increase in overlap area is presumably offset by the added mass, surface area, and contact line length of the droplet resulting in a slight increase in threshold voltage. Again, we note a trend towards larger voltages for smaller droplets and that the contact line geometry appears to play a larger role than the surface area or volume of the droplet.

4.3.3 Effect of Electrode Pitch

To investigate the scaling behavior of electrowetting microactuation, identically shaped arrays with electrode pitch L ranging from 1500 – 150 μm were fabricated and tested. The minimum spacing between adjacent control electrodes was fixed at $L/60$ which indicates a minimum feature size of 2.5 μm for the 150 μm pitch arrays. Since this feature size is the limit of the present technology, these were the smallest electrodes that could be fabricated. The gap height h was reduced in proportion to L, although the manual assembly process made it difficult to accurately control this spacing for distances less than 100 μm. The tested values of L and h are listed in Table 4.4 along with the associated approximate droplet volumes.

Transfer rate characteristics were obtained for each array with 100 mM KCl droplets in 1 cSt. silicone oil. The minimum droplet volume that could be dispensed using the manual pipettor was about 400 – 500 nl. When smaller droplets were required they were formed *in situ* using control electrodes to "pinch off" appropriately sized droplets from a larger source droplet as will be discussed in Section 5.1.1. The resulting droplets were fairly uniform in size ranging from 1.1 – 1.3 times L. However, the inability to precisely control the geometry over the range of electrode pitches studied was a significant limitation of these experiments.

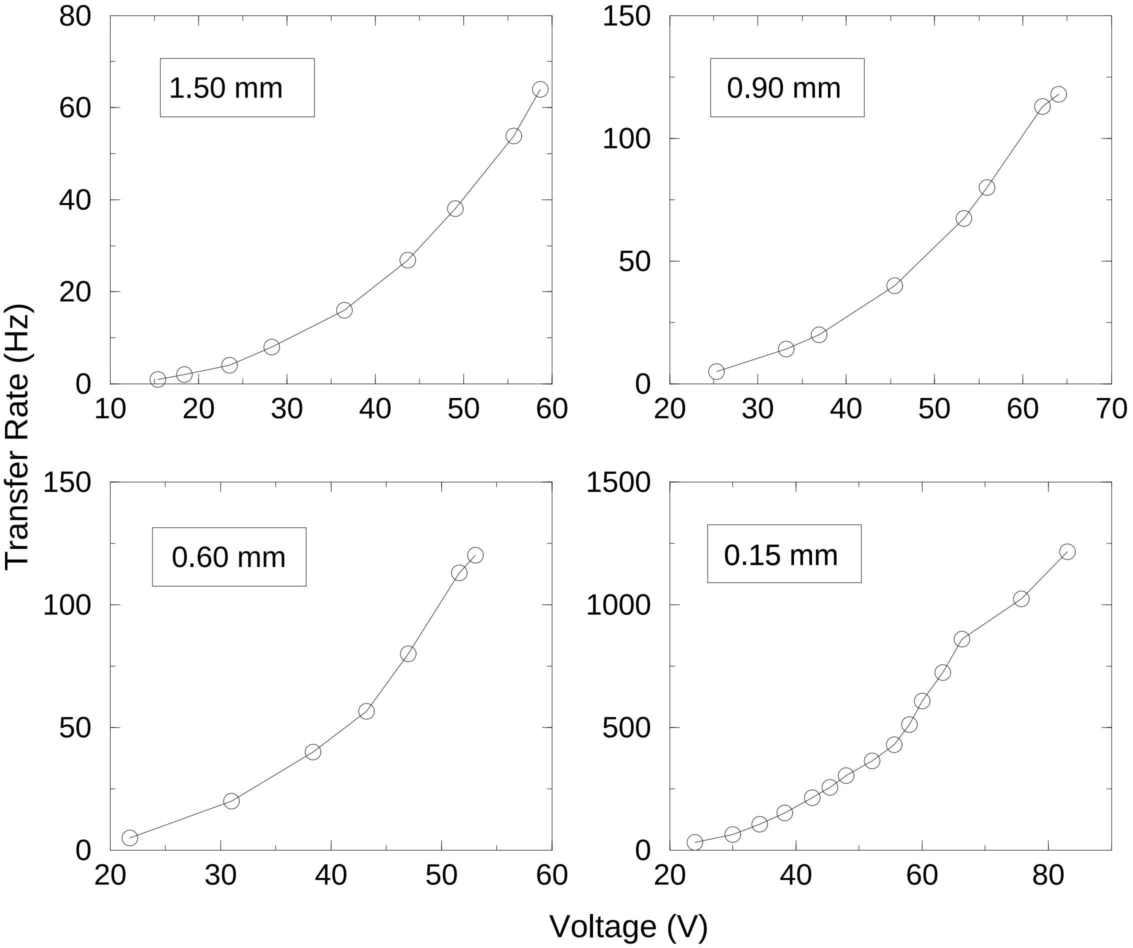

Figure 4.10: Threshold voltage versus maximum transfer rate for electrodes of different pitches

Voltage versus maximum transfer frequency curves for several values of electrode pitch are shown in Figure 4.10. We observe that the transfer frequency at a particular voltage increases with decreasing pitch size. For the smallest electrodes (150 μm pitch) rates in

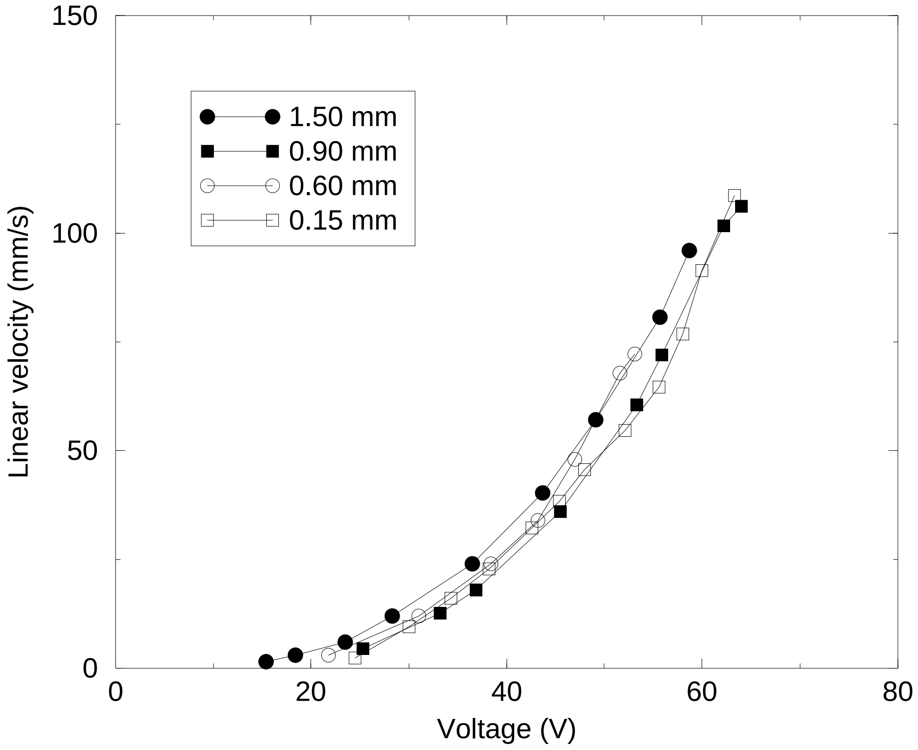

Figure 4.11: Threshold voltage versus average linear velocity $v = fL$ for electrodes of different pitches

excess of 1 KHz were achieved at moderate voltages. If the curves in Figure 4.10 are re-plotted as average linear velocity $v = fL$ rather than frequency they nearly collapse onto a single line for all values of L as shown in Figure 4.11. Thus, the relationship between average linear droplet velocity and voltage appears to be the same over the ten-fold variation in electrode pitch and 300-fold variation in droplet volume studied here.

4.3.4 Effect of Electrode Shape and Arrangement

Alternative electrode shapes including circles and rounded squares were investigated. The primary objective of this was to determine whether electrowetting microactuation could be accomplished using simpler combless electrode designs. Such designs have the potential to reduce fabrication complexity and cost as well as improve the yield and electrical reliablilty of electrowetting-based systems. Circular and square electrodes arranged in 1 x 3 arrays at 1.2 mm pitch were tested (Figure 4.12). In both cases, droplets could be readily transported when they had sufficiently large volumes. We also tested a structure composed of wedge-shaped electrodes arranged in a circular array of outer diameter 4.95 mm shown in Figure 4.13. Droplets were transported around the loop at speeds of up to 200 revolutions-per-minute. We did not attempt to make dynamic comparisons of the different electrode shapes because single-point comparisons are unlikely to be very informative and a larger study of all the relevant geometrical parameters was outside the scope of this work.

We also attempted to transport droplets without a ground electrode, thus implementing the “single sided” arrangement of Figure 2.5. In this case, the top-plate was simply a piece of glass coated with Teflon AF. Squarish electrodes were used for this experiment because the simpler geometry permitted more accurate interpretation of the position of the droplet. The lower portion of Figure 4.12 shows the result when voltage is applied between adjacent control electrodes without ground connection on the top-plate. As predicted by the analysis of Section 2.2.1, the droplet comes to rest halfway between the electrodes.

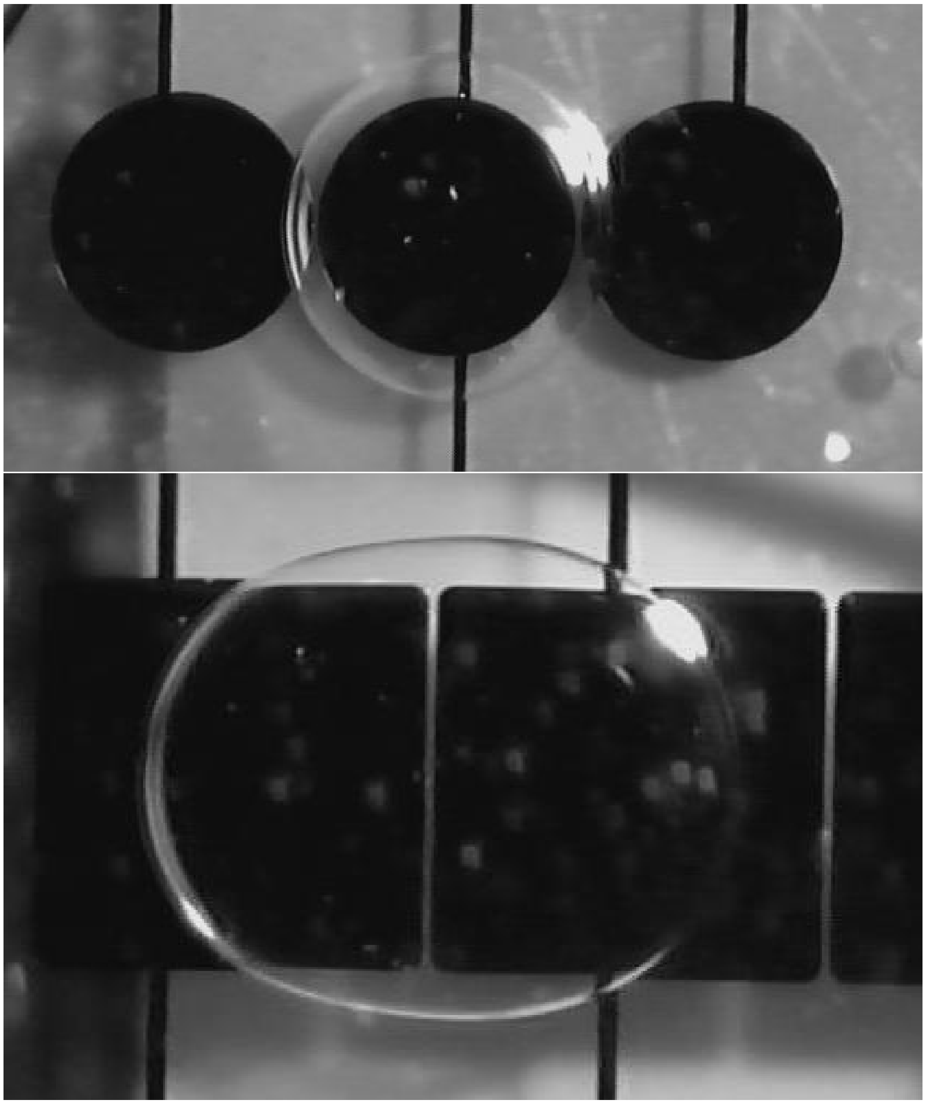

Figure 4.12: Circular and square-like electrodes

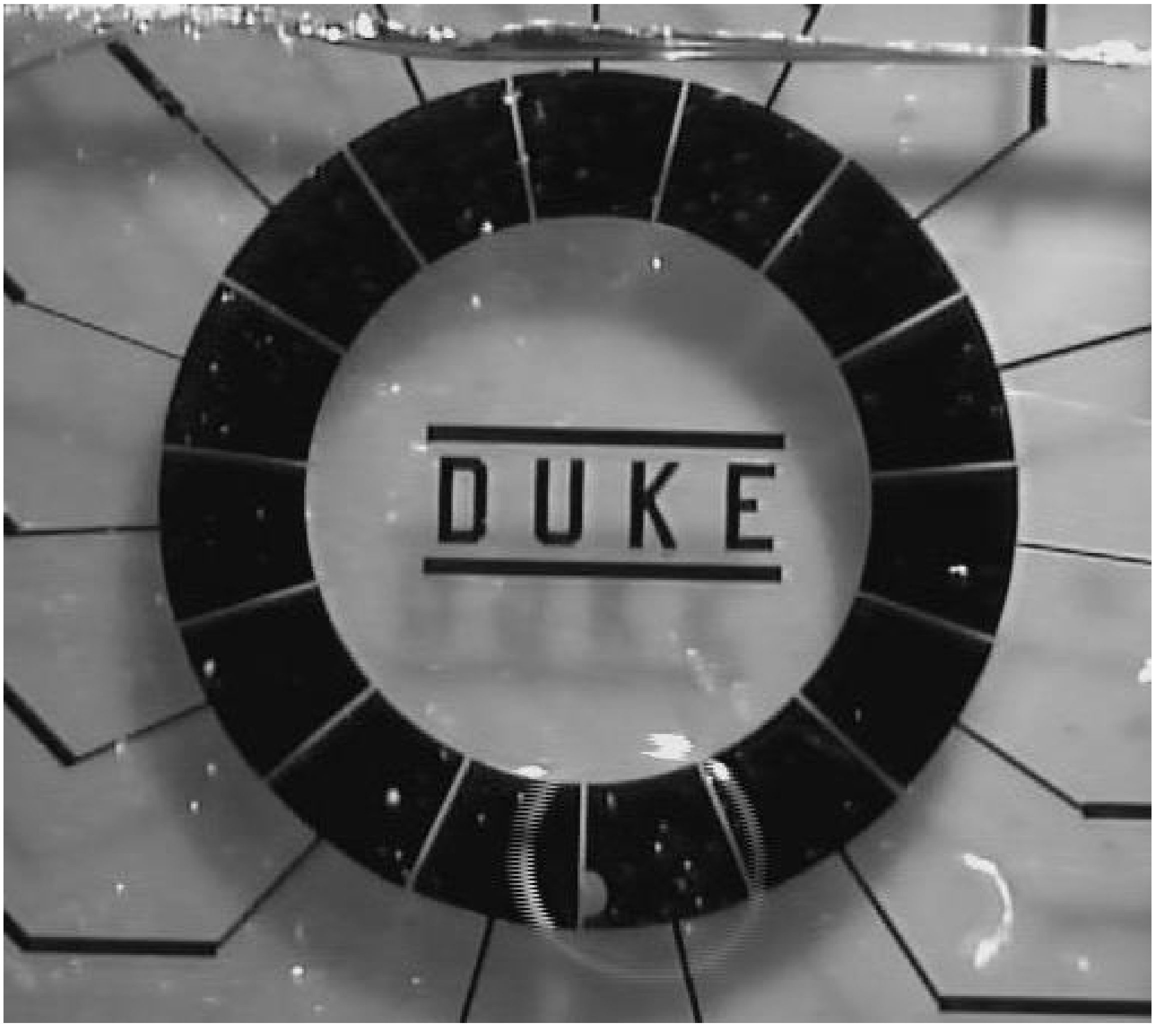

Figure 4.13: Rotary device composed of 15 wedge-shaped electrodes

However, at high voltages the droplet was often observed to travel slightly beyond the midpoint, although never far enough to reach the next electrode. It is not clear whether this high-voltage is related to some fundamental aspect of electrowetting-based microactuation or due to the insulator degradation effects described earlier.

4.3.5 Effect of Medium

The effect of the filler fluid or medium on droplet transport was investigated next. Droplet transfer rates were determined using the standard arrangement in both silicone oil and air. Air measurements were also repeated within several minutes after the oil measurements with the bulk oil having been removed by absorbing it onto a tissue. In this case, oil residue on the surface or in the pores of the Teflon AF is presumed to alter the properties of the surface. The threshold voltage to initiate motion of the droplet was also determined in each case and is plotted as the x-intercept for each curve shown in Figure 4.14.

Silicone oil media improves the transport of droplets at all voltages. While the curve for oil initially rises more slowly than for air, the two curves appear to be more-or-less similar but shifted by about 25 V with respect to each other. Results for “air after oil” show behavior intermediate between that of air and oil. This suggests that the difference between the two media is largely due to effects at the solid-liquid interface rather than the liquid-liquid or liquid-vapor interface. It has been reported that impregnation of Teflon AF with silicone oil reduces the contact angle hysteresis of the surface [43]. Considering that the shapes of the three curves are reasonably similar, contact angle hysteresis provides a plausible explanation for the observed differences. We also note that sometimes droplets could not be transported at all in air on freshly prepared Teflon AF films. However, after allowing the films to age for 1 – 2 weeks, we were usually able to obtain the sort of results shown Figure 4.14. Again, we believe that contact angle hysteresis is the culprit, although we are unaware of the reasons of this aging effect.

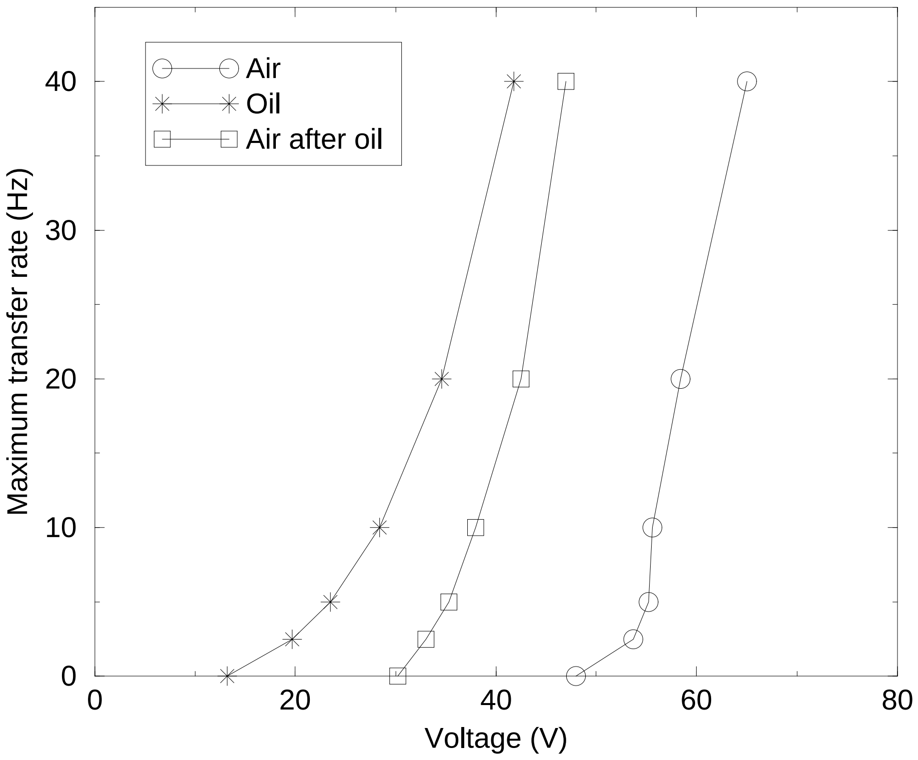

Figure 4.14: Effect of medium on droplet transport rates

The sharper rise in the curves for air at low voltages might be attributed to the observation that the droplets move unsteadily under these conditions. Hesitating or “jerky” movement of the contact line at low velocities has been described in numerous other systems and is known as “stick-slip” behavior [63]. Stick-slip motion is not observed at any velocity in oil, although this is likely explained by the presence of an oil-film between the droplet and surface at low voltages. Young’s equation gives the contact angle at the water-oil-solid triple boundary as

$$\cos\theta_{SWO} = \frac{\gamma_{SO} - \gamma_{SW}}{\gamma_{WO}} \tag{4.1}$$

where the subscripts O, W and S refer the oil, water and solid phases respectively. In terms of measurable parameters, the contact angle may be rewritten as

$$\cos\theta_{SWO} = \frac{\gamma_{WA}\cos\theta_{SWA} - \gamma_{OA}\cos\theta_{SOA}}{\gamma_{WO}} \tag{4.2}$$

where the subscript A refers to air. For Teflon AF and 1 cSt. silicone oil, we have measured $\theta_{SWA} = 104°$, and $\theta_{SOA} = 30°$. The surface tension of the oil γ_{OA} is reported to be 17.4 mN/m [64], water is 72.8 mN/m and we have a measured roughly 34 mN/m for the oil-water interfacial tension γ_{WO}. We therefore calculate $\theta_{SWO} = 164°$, although we observe that water droplets “float” within the oil in the absence of an electric field and so the true value is likely close to, or actually, 180°. A film of oil will exist between the droplet and surface whenever $\gamma_{WO} + \gamma_{SO} < \gamma_{SW}$ is satisfied.

When the oil-film is present and voltage is applied between the droplet and electrode, an electrostatic pressure is developed between the droplet and solid surface which squeezes out the oil. Since the pressure is proportional to the thickness of the oil-film which in turn depends on the pressure, the oil should be excluded rapidly and completely above some threshold voltage. It is also possible that the oil becomes trapped as miniscule droplets at the water-solid interface. The possible presence of an oil-film implies that the droplet may not always remained grounded as was initially assumed. Furthermore, the interaction of wetting and dewetting processes (contact line movement) and adhesion and de-adhesion processes (separation of interfaces) may complicate our attempts to understand the underlying physics of the process.

4.3.6 Effect of Droplet and Oil Viscosity

The effect of droplet viscosity was investigated using sucrose as an additive to modify the viscosity of 100 mM KCl droplets. Addition of up to 60 wt.% sucrose produced viscosities ranging from 1.0 – 58.4 cP. Addition of sucrose also increased the surface tension and density of the droplets, but these effects were relatively small compared to the effect on viscosity as shown in Table 4.5. The threshold voltage for continuous 10 Hz travel of 900 nl droplets on 1.5 mm pitch electrodes was determined for each sucrose solution in Table 4.5 and the results are plotted in Figure 4.15. We observe an initially sharp increase in threshold voltage as a function of viscosity with progressively smaller slope at higher viscosities. However, even over the entire 60-fold range of viscosity, the threshold voltage varies by only approximately 10%.

The effect of the silicone oil viscosity was investigated using oils of different molecular weight provided by Gelest, Inc. Again, there is a slight variation in the surface tension and density associated with oils of different viscosity, but these effects are comparatively small as shown in Table 4.6. The threshold voltage for 10 Hz travel of 900 nl droplets of 100 mM KCl solution was determined in each oil with results plotted in Figure 4.16. The viscosity of the oil appears to have a much larger effect on transport rates with a 75% increase in threshold voltage associated with a 10-fold variation in oil viscosity. The larger effect of the oil viscosity might be explained through its interaction at the droplet/solid interface. In addition to increasing the hydrodynamic resistance to the moving droplet, the oil viscosity may influence the thickness and dynamics of the oil film between the droplet and insulator and lead to reduced electromechanical coupling (by reducing the capacitance).

Sucrose conc. (wt. %)	**Viscosity (cP)**	**Surf. Tens. (mN/m)**	**Density (g/cm^3)**
0	1.0	72.8	1.00
20	1.9	73.0	1.08
50	15.4	74.9	1.23
60	58.4	76.5	1.29

Table 4.5: Physical properties of sucrose solutions. From [65]

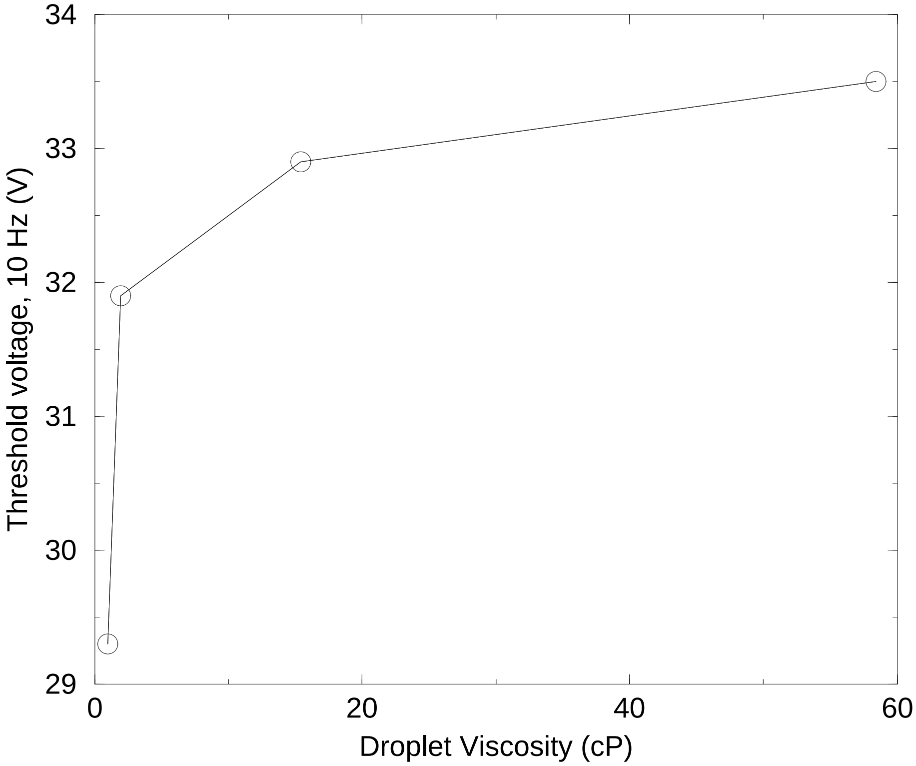

Figure 4.15: Effect of droplet viscosity on 10 Hz threshold voltage

4.4 Video Analysis of Droplet Transport

Droplet transport dynamics were studied through a frame-by-frame video analysis of moving droplets. For these experiments, video was recorded using a higher frame rate (60

Kin. Visc. (cSt.)	**Dyn. Visc. (cP)**	**Surf. Tens. (mN/m)**	**Density (g/cm^3)**
1.0	0.8	17.4	0.818
2.0	1.7	18.7	0.873
5.0	4.6	19.7	0.918
10.0	9.4	20.1	0.935

Table 4.6: Physical properties of different silicone oils. From [64]

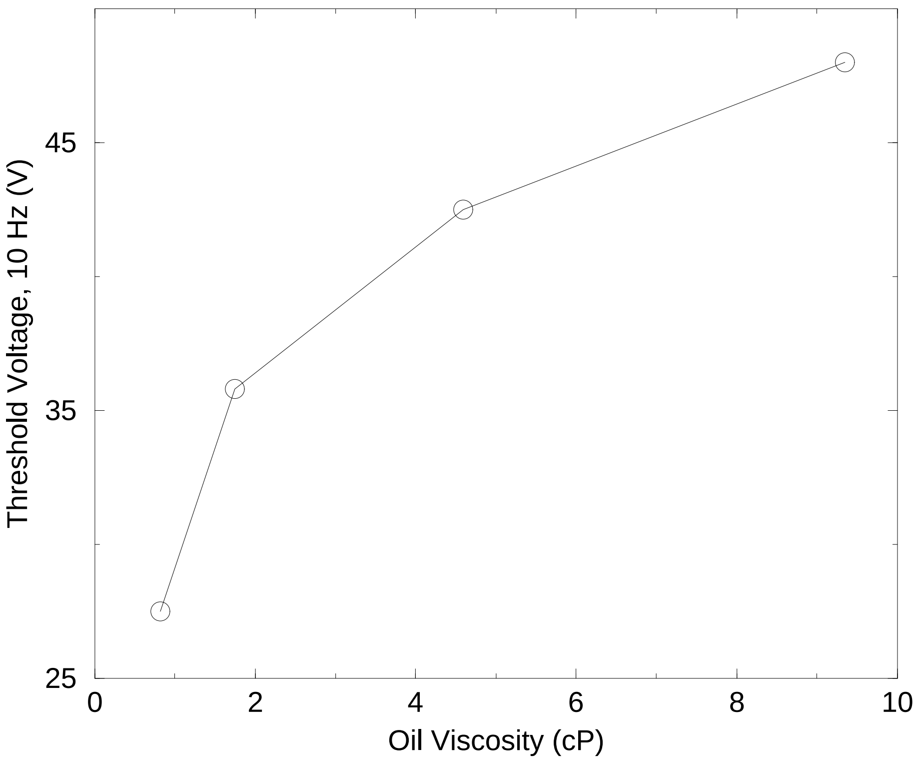

Figure 4.16: Effect of silicone oil viscosity on 10 Hz threshold voltage

frames/s) camera and electronic image enhancement equipment. The standard experimental system was used with a switching rate of 2 Hz ($T = 0.5$ s) at approximately 26 V. Images were subsequently analyzed to determine the position and shape of the droplet as a function of time. The positional accuracy of the analysis after digitization was about 10 μm.

The position of both the leading and trailing edges of the droplet relative to their initial positions during the course of a single electrode transfer is shown in Figure 4.17. It is evident that the droplet elongates along the axis of motion as the leading edge initially accelerates more rapidly than the trailing edge. The difference between the two curves in Figure 4.17 is plotted as percent elongation (relative to initial length) in Figure 4.18. The droplet elongation reaches a maximum value of 7% at approximately $T/4$ and by $T/2$ the droplet has nearly recovered its original shape.

The center of the droplet was taken to be the mean position of the two edges. The velocity and acceleration of the center of the droplet were then determined by differentiating a high-order polynomial fit to the position data. The results are shown in Figure 4.19. The droplet reaches a maximum velocity of approximately 6.5 mm/s, over twice the mean velocity, at a time between $T/4$ and $T/2$. The magnitude of the droplet acceleration during the second half of the cycle is somewhat smaller than during the first half of the cycle. The effect of droplet elongation can be seen as small velocity peak during the initial part of the cycle.

4.5 Modeling of Wetting Kinetics

Summarizing the results of the dynamic testing, we find that within certain regimes the droplet velocity appears to be nearly independent of the geometry of the system. Thus, droplets larger than some threshold require little or no additional energy for transport, despite their additional mass and surface area. We also find a scaling relationship whereby

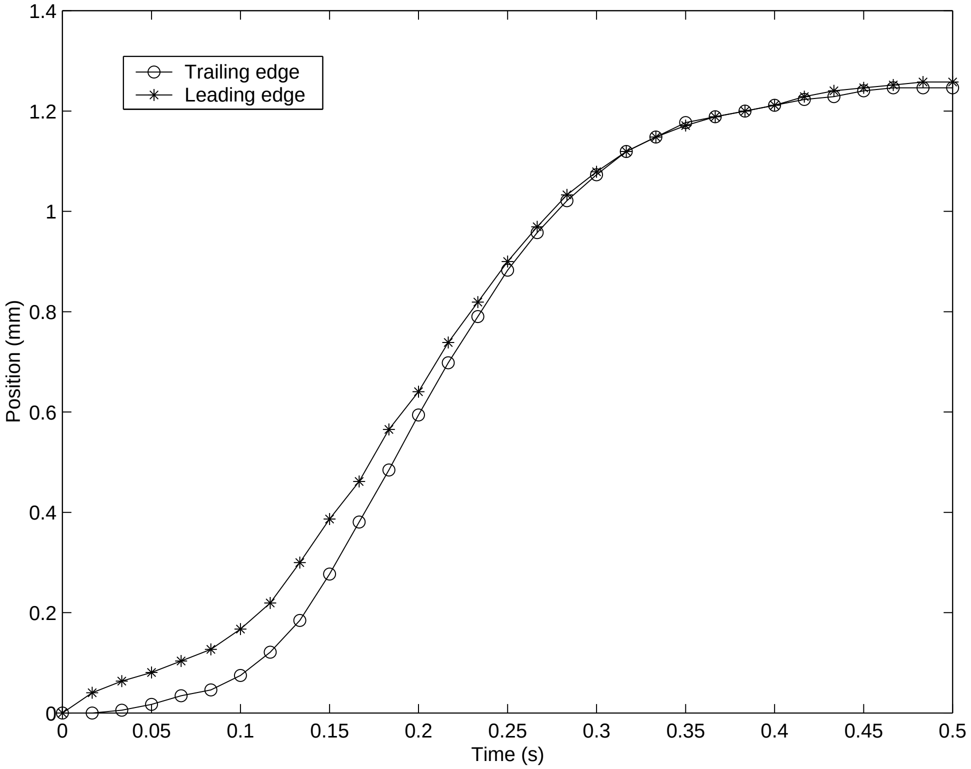

Figure 4.17: Cumulative distance traveled by the leading and trailing edges of the droplet as a function of time

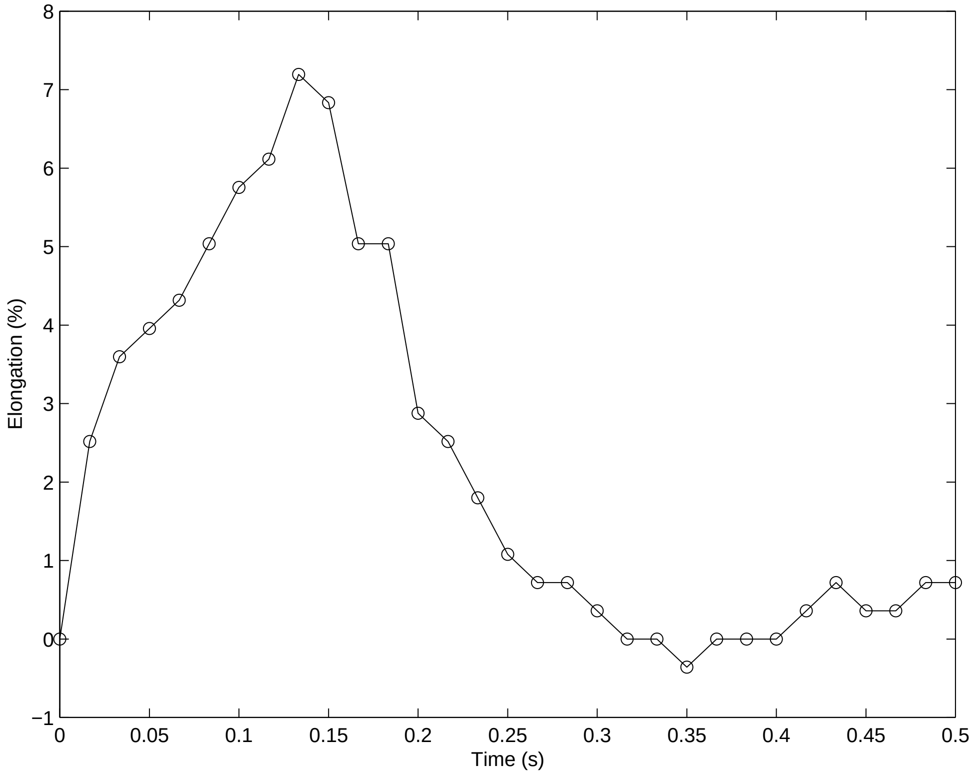

Figure 4.18: Elongation of a moving droplet along its axis of motion as a function of time

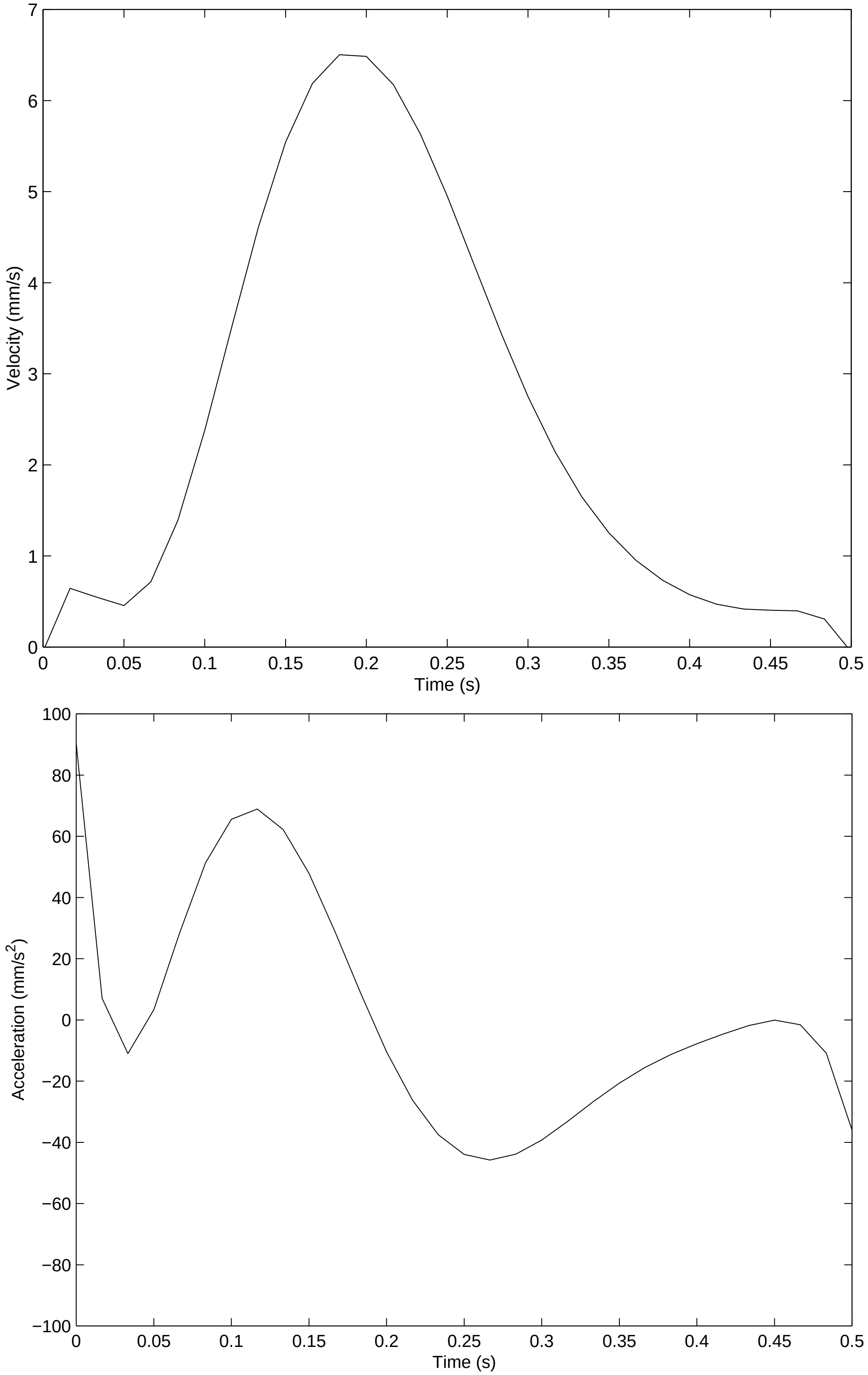

Figure 4.19: Droplet velocity (top) and acceleration (bottom) as a function of time

the linear velocity of the droplet as a function of voltage is conserved over a ten-fold range of length scales and 300-fold range of droplet volumes. Furthermore, the viscosity of the droplet appears to only modestly affect the rate at which it can be transported. Taken together, these observations suggest that dissipative processes occurring in the interior of the droplet (i.e. hydrodynamics) have relatively little effect on the dynamic behavior of the droplet.

On the other hand, we observe that the chemical condition of the surface may have a very large effect. The presence of a (presumed) submicroscopic silicone oil film reduced the voltage requirement in air by 15 – 20 V. We also observed that many times droplets could not be transported at all in air depending on the age and condition of the Teflon AF film. Thus, we are led to the conclusion that droplet transport dynamics are largely governed by interactions occurring at or near the wetting line, and that the speed at which the contact line may advance (or recede) across the surface imposes the limit on droplet velocities. Even the observed geometrical dependencies might be explained in terms of their effect on the shape and position of the wetting line rather than through strictly hydrodynamic effects.

Thus, one possible model might view the droplet as a sort of deformable band which deforms and moves in response to a force field which acts only along its perimeter. However, calculating this force field is an extremely difficult problem as it depends on the local electric field as well as multiple physical and chemical processes occuring at and around the wetting line. Furthermore, there are major uncertainties about the physical conditions in our system. For example, whether an oil-film is present between the droplet and surface, or how the contact angle of the droplet changes as it moves, or how effects like contact angle saturation and hysteresis or dissipative mechanisms such as microdroplet expulsion effect the behavior of the droplet. Even in the absence of electrostatic effects, modeling and simulation of dynamic wetting behavior is an extremely complicated problem that has only been solved for a few simple cases. Given that a full model which takes into account all of the relevant geometry and physics is presently unfeasible, simple models of wetting kinetics under ideal conditions may provide at least first-order insights. We attempt to apply one such wetting model to our experimental data.

Wetting Kinetics Models

Most theoretical and experimental studies of wetting kinetics are concerned with explaining one of two possible dynamic situations. The first, droplet spreading, is concerned with the determination of the time-dependence of the spontaneous change in contact angle of a non-equilibrium droplet resting on a solid surface [66][67][68]. The second attempts to account for the velocity dependence of the contact angle of a liquid which is forcibly driven across a surface [45][69][46]. We have already noted that because of contact angle hysteresis, the equilibrium angle may assume a range of values between the advancing and receding limits θ_A and θ_R. When a liquid is driven across a surface, the contact angle assumes a dynamic value which increases with positive velocity and decreases with negative velocity, potentially reaching 180° or 0° in the limit (Figure 4.20). At these limits fluid entrainment occurs and a maximum velocity for forced wetting (or dewetting) is obtained. The determination of maximum wetting velocities is an important problem in certain industrial applications such as liquid-coating and petroleum recovery.

At present, only a partial theoretical understanding of wetting kinetics is available. In a review of dynamic wetting, Blake [63] reports that a number of fundamental uncertainties and theoretical challenges surround the interpretation of wetting behavior. For example, there is disagreement concerning whether experimentally measured contact angles reflect the true situation at microscopic distances from the contact line. Some have argued that dynamic contact angles result from hydrodynamic distortion near the contact line and that the true contact angle remains fixed at the equilibrium value. Others have proposed that

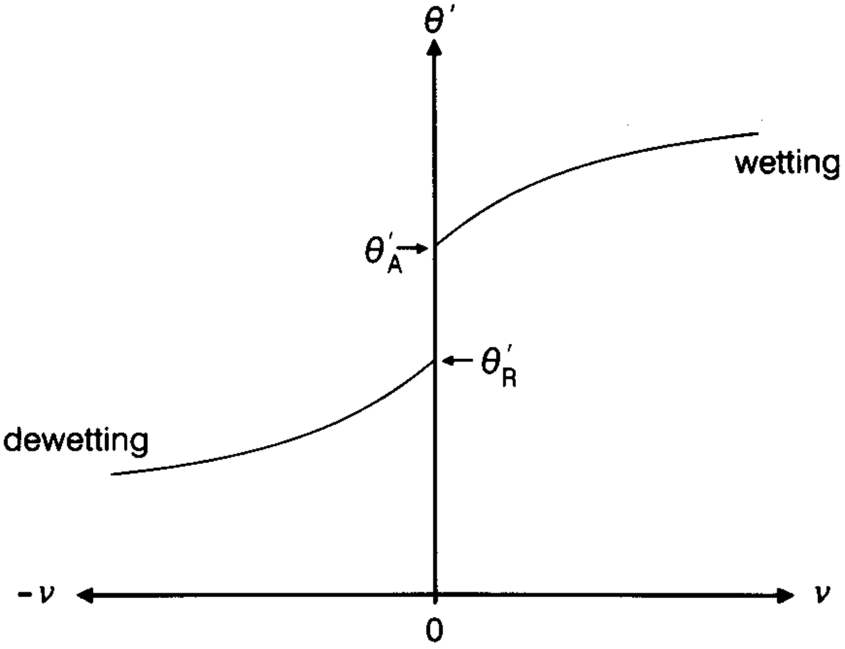

Figure 4.20: Velocity dependence of the contact angle. From [63]

the displaced phase is always entrained by the advancing phase, forming a submicroscopic film that subsequently collapses.

Wetting models fall into two categories: hydrodynamic and molecular-kinetic. Hydrodynamic models emphasize the dissipation due to viscous flows within the core of the droplet, and neglect the mechanism by which the contact-line moves across the surface. To avoid violating the no-slip condition, hydrodynamic calculations are usually truncated some finite distance away from the contact-line. Molecular-kinetic models on the other hand focus on the dissipative molecular processes occurring at the advancing contact-line and neglect the viscous flows within the droplet. It seems likely that neither approach can provide a complete description and several attempts have been made to develop a combined model which allows for both types of dissipation [66][68].

Molecular Kinetic Theory

A theory of wetting based upon statistical molecular interactions at the contact line was first proposed by Blake and Haynes [70]. The molecular-kinetic theory of wetting assumes that the macroscopic motion of the wetting line is determined by individual molecular displacements occurring along its length. The overall speed v is determined by the frequency k and length λ of these displacements. There are n adsorption sites per unit area and when these sites are isotropically distributed $\lambda = n^{-1/2}$. If k^+ is the frequency of displacements in the forward direction and k^- is the frequency in the reverse direction, then $k_{net} = k^+ + k^-$ is the net frequency and $v = k_{net}\lambda$. From the theory of activated transport processes in liquids, k_{net} may written in terms of its equilibrium value k_0 giving

$$v = 2k_0\lambda \sinh\left(\frac{w}{2nkT}\right) \tag{4.3}$$

where w is the work done per unit area by the driving force, k is Boltzmann's constant, and T is the absolute temperature. In the absence of applied force, the net rate of displacements is zero and the contact line fluctuates around its mean position. For small forces with the argument of $\sinh \ll 1$, Equation 4.3 reduces to

$$v = k_0\lambda \frac{w}{nkT} \tag{4.4}$$

and the velocity is linear with respect to w. The linearized form is sometimes written as

$$v = \frac{1}{\zeta_0} w \tag{4.5}$$

where $\zeta_0 = nkT/k_0\lambda$ may be viewed as a friction coefficient for the contact line. For large arguments of sinh the expression becomes

$$v = k_0\lambda \exp\left(\frac{w}{2nkT}\right) \tag{4.6}$$

and an exponential dependence is obtained.

For modeling dynamic contact angle behavior, the driving force is assumed to be the out-of-balance surface tension force acting at the wetting line which is given by

$$w = \gamma_{LV}(\cos\theta_0 - \cos\theta) \tag{4.7}$$

where θ_0 is the equilibrium contact angle and θ is the dynamic contact angle. Contact angle hysteresis is accounted for by setting θ_0 equal to θ_A or θ_R depending on the direction of impressed motion. This model for dynamic contact angle has been applied to a number of systems, with n, λ and k_0 determined by curve-fitting of data. The fitted values of the molecular parameters are generally consistent with their physical interpretation. However, is also true that these parameters are not otherwise measurable, and these models therefore have more theoretical than practical utility.

The molecular-kinetic model of wetting has recently been extended to the problem of electrostatic assist [45][46]. Electrostatic assist is essentially an application of electrowetting where the electrowetting effect reduces the dynamic contact angle of a flowing liquid and permits higher wetting or coating speeds by postponing the onset of entrainment. In this case, the equation (slightly modified here) describing the velocity dependence of the contact angle was [45]

$$v = 2k_0\lambda\sinh\left(\frac{\gamma_{LV}}{2nkT}\left[\cos\theta_0 + \frac{\epsilon_0\epsilon_r}{2d\gamma_{LV}}V^2 - \cos\theta_E\right]\right) \tag{4.8}$$

where $\cos\theta_E$ is the dynamic contact angle in the presence of the electric field. Reasonably good curve-fits to the experimental data were obtained with this equation for values of λ and k_0 which were independent of the electric field.

In electrostatic assist, the liquid is driven by an externally applied force (e.g. a moving plate) and the voltage modifies the wetting characteristics. In this work the voltage itself drives the motion of the liquid, and we make the assumption that the voltage term dominates the argument of the sinh function and that the effect of the dynamic contact angle may be neglected. We further assume that contact angle hysteresis can be modeled as a negative energy constant in the sinh argument expressed as an effective voltage threshold V_T. Thus we obtain the equation

$$v = 2k_0\lambda \sinh\left(\frac{\epsilon_0\epsilon_r}{4dnkT}\left[V^2 - V_T^2\right]\right) \tag{4.9}$$

Assuming isotropic distribution of sites $\lambda = n^{-\frac{1}{2}}$ we have three unknowns λ, k_0, V_T, three independent fitting parameters X_1, X_2, X_3, and an equation of the form

$$v = X_1 \sinh\left(X_2[V^2 - X_3]\right) \tag{4.10}$$

It is important to note that when the argument of sinh is small, the equation is linearized and X_1 and X_2 are no longer uniquely determined. For the curve-fits presented here the maximum value of the sinh argument was 1.2 – 2.0. Thus X_1 and X_2 could be separately resolved, but only over a portion of the data.

Figure 4.21 shows fitting curves for the data obtained under different media conditions from Figure 4.14. The values of the fitting parameters for each condition are listed in Table 4.7. Values for the scaled arrays of Figure 4.11 are also listed with two separate sets of data for the 1.5 mm pitch system (all under silicone oil). In addition to λ, k_0 and V_T, we calculate $k_0\lambda^3$ which is inversely proportional to the linearized friction coefficient ζ_0. We also recast the hystersis energy term as an activation energy E_a per absorption site. This activation energy represents additional irreversible work associated with each molecular displacement although its origin, like contact angle hystersis generally, is not well understood.

The value of λ ranges from 0.38 – 0.85 nm across the data and has no clear trend with respect to the experimental manipulations. The values of λ from the scaling experiments are nearly half of the values from the medium type experiments, although this may be due to variations associated with different chips since the two sets of conditions overlap.

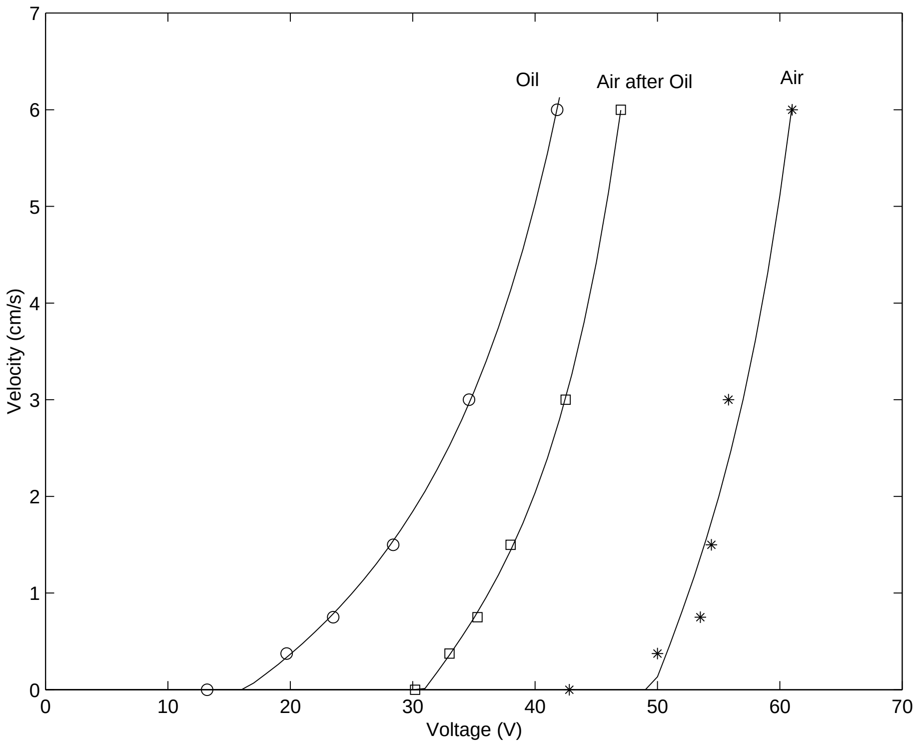

Figure 4.21: Curve-fits of experimental data using molecular-kinetic model

Condition	λ **(nm)**	k_0 **(MHz)**	$k_0\lambda^3$	V_T **(V)**	E_a **(kT)**
Air	0.76	16.9	7.5	49.6	3.09
Air after oil	0.85	10.0	6.2	30.9	1.50
Oil	0.72	16.7	6.2	16.2	0.22
Oil 1.5 mm A	0.38	113.2	6.1	19.1	0.11
Oil 1.5 mm B	0.53	31.6	4.7	18.8	0.21
Oil 0.90 mm	0.39	101.7	6.0	25.6	0.21
Oil 0.60 mm	0.56	26.5	4.6	18.7	0.23
Oil 0.15 mm	0.45	49.5	4.6	18.7	0.15

Table 4.7: Molecular-kinetic model fitting parameters

These values of λ are slightly lower than, but not inconsistent with other reported values. For example, Blake [63] reports values ranging from 0.36 – 1.40 nm for various systems, while Schneemilch *et al.* [46] report somewhat higher values (1.20 – 3.14 nm) for their studies of water on Teflon AF. The precise physical meaning of the parameter λ is not presently understood. For heterogenous solids, λ is expected to be related to the chemical structure of the surface, while for amorphous and homogeneous solids it is expected to be related to the molecular size of the liquid. In practice, λ does not correspond well to either molecular dimension and may depend in some complex way on the fluid structure at the interface [69]. However, the size of the liquid molecule (0.3 nm for water) may at least indicate a minimum theoretical value of λ which is not inconsistent with our results.

Somewhat larger variations were obtained for k_0 which ranged from 10.0 – 113.2 MHz. Again, there was no clear trend across the data or with respect to the experimental manipulations. These values of k_0 are at the high end, but not inconsistent with other values in the literature which range from 10^3 – 10^9 Hz with typical values on the order of 10^6 Hz. It possible that the large variations in λ and k_0 may be partially due to poor resolution of these parameters at small arguments of sinh. Indeed, the product $k_0\lambda^3 \propto 1/\zeta_0$ appears to be more consistent, grouped around two values for oiled surfaces (4.6 and 6.1 MHz·nm^3) and one value for air (7.5 MHz·nm^3). It is possibly significant that identical values of ζ_0 were obtained for oil and oil-after-air on the same chip, while a significantly higher value was found for air. This might suggest similar “frictional” properties for the two oiled surfaces at low velocities. If E_a is thought of as “static friction” and ζ_0 “kinetic friction”, then this might imply that the oil-film provides equivalent reduction in kinetic friction compared to the oil-filled condition, but a lesser degree of reduction in static friction. The apparent grouping of ζ_0 around two different values for oil is intriguing and could be related to degradation or charging effects in some chips but not others. The parameter V_T shows the expected dependence on the type of medium and independence with respect to scale. The activation energy, E_a, which is equivalent to the electrostatic energy per site associated with V_T, shows a trend similar to that of V_T, with $0.19kT$ for oil, $1.50kT$ for air-after-oil and $3.09kT$ for air. Thus, the difference in V_T between the various conditions is not merely a consequence of variation in λ.

The quality of the curve-fits and reasonable values of the molecular parameters obtained here tends to suggest an underlying validity for this modeling approach. However, these results are based on too little data and the model requires too many simplifications to justify any conclusions. It should be remembered that this model describes a single average contact line velocity, while the real droplet contact line is characterized by both a time and positional dependence. Additionally, the moving droplet contains both advancing and receding interfaces which are usually treated differently under molecular-kinetic analysis. The results presented here, therefore, capture only certain average features of the contact line motion and the molecular parameters may thus lose their physical meanings. In any case, the physical interpretation of these parameters remains controversial and none of them are directly measurable, so that the model, even if correct, has relatively little predictive value. However, further fundamental studies of the processes at the moving contact line under conditions controlling for geometrical and time-dependent effects may ultimately provide a basis for effective models of electrowetting-driven droplet motion.

4.6 Chapter Summary and Conclusions

The dynamics of transferring a droplet between two adjacent electrodes was investigated. Droplet transfer speeds as a function of voltage were determined using a manual balancing technique in which voltage pulses were programmed to switch at a fixed frequency and the voltage magnitude was adjusted until the droplet was able to follow the traveling pulse. However, several problems affected the reliability of these measurements. The most significant problem was the tendency of the insulation to degrade, particularly at high voltages. This degradation effect was unpredictable and had a dramatic effect on the measured transfer rates, although attempts were made to control for it as much as possible.

The effect of various geometrical and liquid parameters on droplet transport was studied. Variation of the droplet width and height was found to have relatively little effect on droplets larger than a certain threshold size. Scaling of the system geometry produced proportionally higher transfer rates, with linear velocities remaining fixed as a function of voltage. Several alternative electrode shapes were tested and droplets could be rapidly transferred in each case which relaxes the fabrication requirements for future devices. The droplet medium had a very significant effect on droplet transport, with silicone oil producing far better and more consistent results than air. However, when the Teflon AF surface had been soaked in oil, results in air were significantly improved. Droplet viscosity had a relatively small effect on transfer rates, while the oil viscosity produced a much larger effect. Visualization of the droplet transfer process confirms the presence of both deformational and translational effects during droplet flow.

Surveying these results we concluded that the dynamics of droplet flow are primarily governed by processes at the wetting line rather then hydrodynamic effects inside the droplet. A simple model for wetting kinetics was presented and molecular parameters were obtained by curve-fitting the data. Although these results did not justify any meaningful conclusions, they do seem to support the basic validity of the model. However, a more accurate model which accounts for geometrical and time-dependent effects will not be possible until a better understanding of all of the relevant physical phenomena at the contact line is available.

Chapter 5

Experimental Results - System Implementation Issues

While the transport of liquid droplets is a constituative operation of digital microfluidics, it alone cannot serve as the basis for practically useful systems. An additional requirement for most systems is that the unit droplets can be generated from a macro-droplet or continuous-flow source with some degree of volume consistency. Recklessly pursuing the microelectronic analogy, we may refer to this process as analog-to-digital conversion. Thus, practical systems demand formational and volumetric control of droplets in addition to positional manipulations. Reliable and efficient operation of digital microfluidic systems will likely require some droplet detection and sensing capabilities as well. Power dissipation issues are critical for many biological applications where thermal control is essential. Issues of solvent compatibility and droplet integrity are extremely important for determining the classes of applications and operations which may be best suited to the technology. In this chapter, we attempt to experimentally address each of these issues and provide a basis for assessing the feasibility of, and implementing practically useful systems.

5.1 Droplet Generation and Splitting

Generation of uniform unit-sized microdroplets from a continuous fluid source is a critical operation affecting the servicability of droplet-based microfluidic systems. Once microdroplets are formed, further volume manipulations may also be required. For example, a single sample droplet may be divided or aliquoted into multiple smaller droplets for a series of parallel measurements. When droplets are mixed or fused together, a subsequent (or antecedent) fission step may be required to maintain a consistent droplet size for transport.

Systems may operate simultaneously on droplets of unit-size and droplets of integer multiples of the unit-size in the same way that digital electronic systems work simultaneously with bits, bytes, and words. Thus one droplet size may be employed to transport material from a source to a test array where the droplet is subdivided, operated upon, and possibly further subdivided, or reassembled for transport to a new location. However, such schemes would ultimately have to contend with the effect of varying the aspect ratio within a single fixed gap height.

5.1.1 Electrowetting Droplet Generation

The original design featured a surface tension inlet designed to provide an interface between an exterior macroscopic "input" droplet and the interior electrodes of the array. This feature was later abandoned because of processing related difficulties. Later designs retained the droplet-forming electrodes which were tested on macrodroplets that had been manually inserted between the electrode plates. Although we could form microdroplets on an *ad hoc* basis when required, as for the scaling experiments at small pitch as shown in Figure 5.1, the process could not be automated and the performance of the droplet-forming electrodes was generally dissatisfactory.

There were several reasons for the poor performance of these droplet generation devices. First, given the relatively large surface area covered by the inlet electrodes (1 – 30 mm^2), they were particularly susceptible to damage arising from randomly distributed defects in the insulation. Since the function of these electrodes is essentially to pin and deform the edges of the droplet, it is possible that much of the interior area of these electrodes could be removed in future designs to minimize this problem. In fact, we observed that the thin electrodes formed by the wires were quite capable of pinning the contact line and deforming droplets which led to the second major difficulty.

Since the wires were in the same layer as the control electrodes, they exerted an elec-

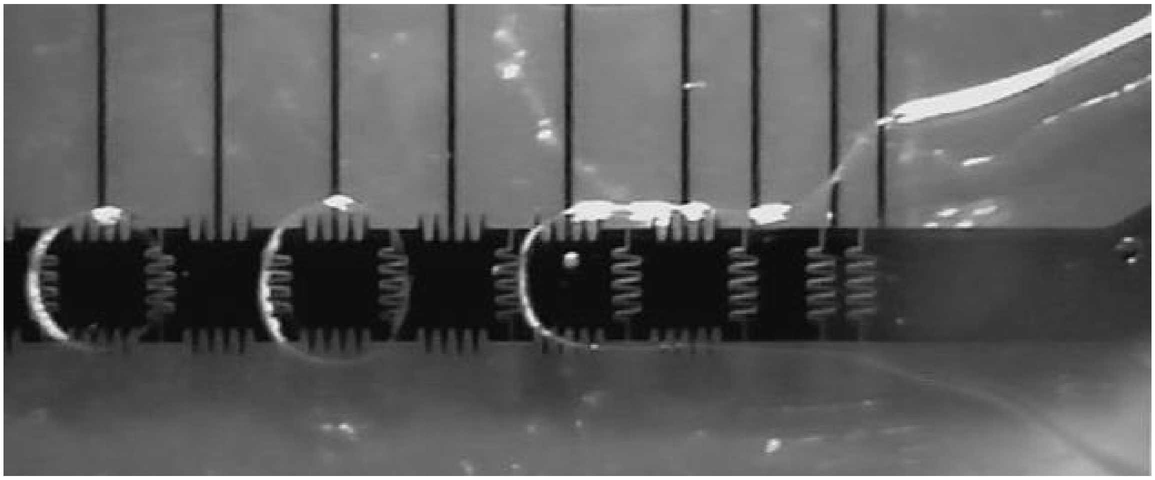

Figure 5.1: Electrowetting formation of microdroplets

trowetting force on the droplet which interferred with the action of the electrodes. This can be clearly seen in Figure 5.1 where the wire leading to the rightmost electrode has caused the large droplet to spread perpendicularly to the axis of the array. This effect usually precluded the formation of an appropriately shaped liquid plug for dispensing microdroplets. Additionally, the wires sometimes resulted in stretching of resting microdroplets perpendicularly to the axis of the array as can also be seen in Figure 5.1. An extreme case of this phenomenon can be seen in Figure 5.2 where the contour of an oversized droplet has broken free of the control electrodes and propagated along the length of two wires for a distance of several mm (including several right-angle turns along the way). In a two-level metal process, the wires would be buried under a thicker layer of insulation avoiding this problem. Thicker insulation could also be deposited and patterned over the wires in a single-level metal process requiring only one additional mask level. Even without additional mask levels there is ample opportunity to minimize the size and optimize the placement of wires to reduce this problem.

Another problem was that the length of the extension arms of the inlet electrodes were generally too short and the enlarged (paddle-shaped) portions too small to allow a well-

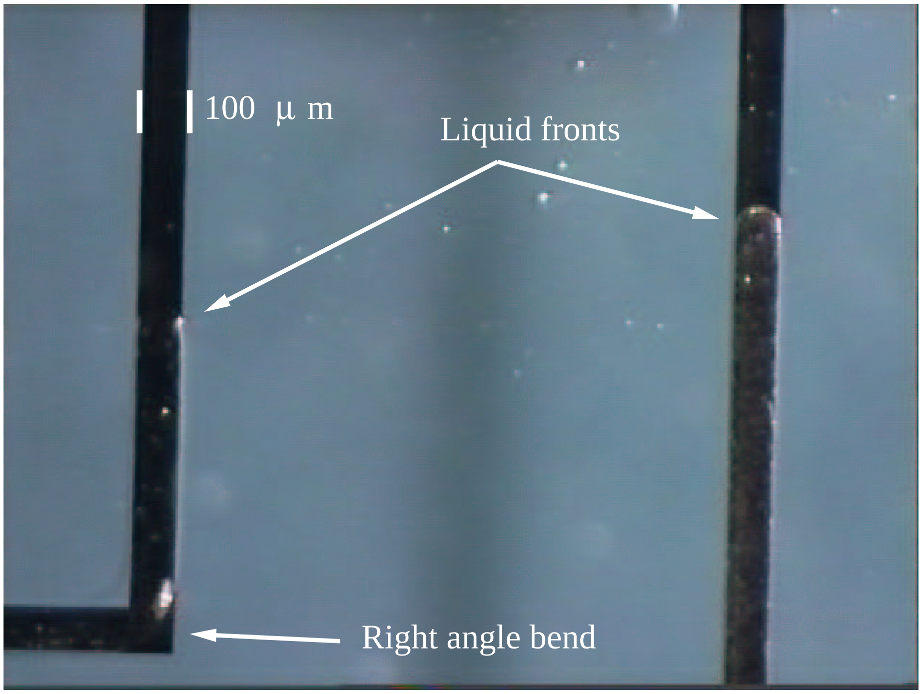

Figure 5.2: Inadvertant formation of liquid channels along 100 μm wide wires

defined liquid plug to be formed. Thus, the macrodroplets tended to deform bluntly, rather than acutely as required for plug formation. In the original 150 μm design the arms were 4.5 mm long or 30 times the width of the arm. However, as the electrodes were enlarged in later designs it became necessary to abbreviate the extension arm length to accomodate a reasonable die size. Thus this ratio shrank to 2 – 4 in the later designs, with similar transformation occuring to the enlarged portions of the electrode. These results demonstrate that electrowetting forces can be used to generate microdroplets from a much larger source droplet, but that improved designs for this operation are needed.

5.1.2 Pressure-Assisted Droplet Generation

We next investigated the use of an external pressure source to assist electrowetting microdroplet formation. The general setup is illustrated in Figure 5.3. A vial containing the electrolyte liquid is pressurized through a three-way solenoid valve by a conventional micropump and pressure regulator capable of delivering up to 15 psig. The valve switches the vial pressure between the pump output and atmospheric pressure requiring 5 – 20 ms to open depending on the pressure. Conventional plastic tubing connects the vial to the chip where a plastic pipette tip mates the tubing with a 0.75 mm hole drilled in the top-plate. The valve is controlled electronically using the same hardware and software that controls electrode switching.

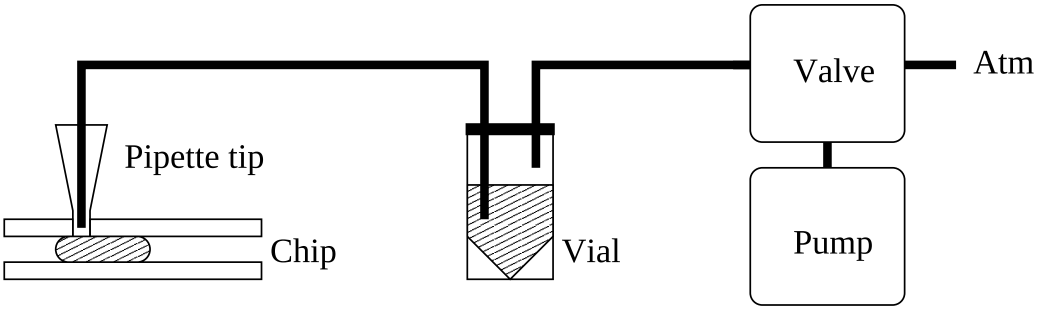

Figure 5.3: Experimental setup for pressure-assisted electrowetting droplet generation

The procedure used to generate droplets was to first pressurize the electrolyte to begin the flow of liquid into the oil-filled gap (Figure 5.4A). Simultaneously, three or four electrodes adjacent to the hole were energized to guide the fluid along the main axis of the array. When the liquid front reached the most distant of these electrodes, the other electrodes were de-energized and the valve was opened to atmospheric pressure (Figure 5.4B). Because the surface is highly hydrophobic, the liquid retracts into the pipette tip upon the removal of the positive pressure. As the liquid retracts, a droplet is formed and remains on the energized electrode (Figure 5.4C). This droplet is subsequently transported away (Figure 5.4D) and the process may be repeated.

Through proper adjustment of the voltage, pressure and timing we were able to automatically generate and transport hundreds of droplets of fairly uniform volume. A histogram of some of the generated droplet volumes is shown in Figure 5.5. These volumes

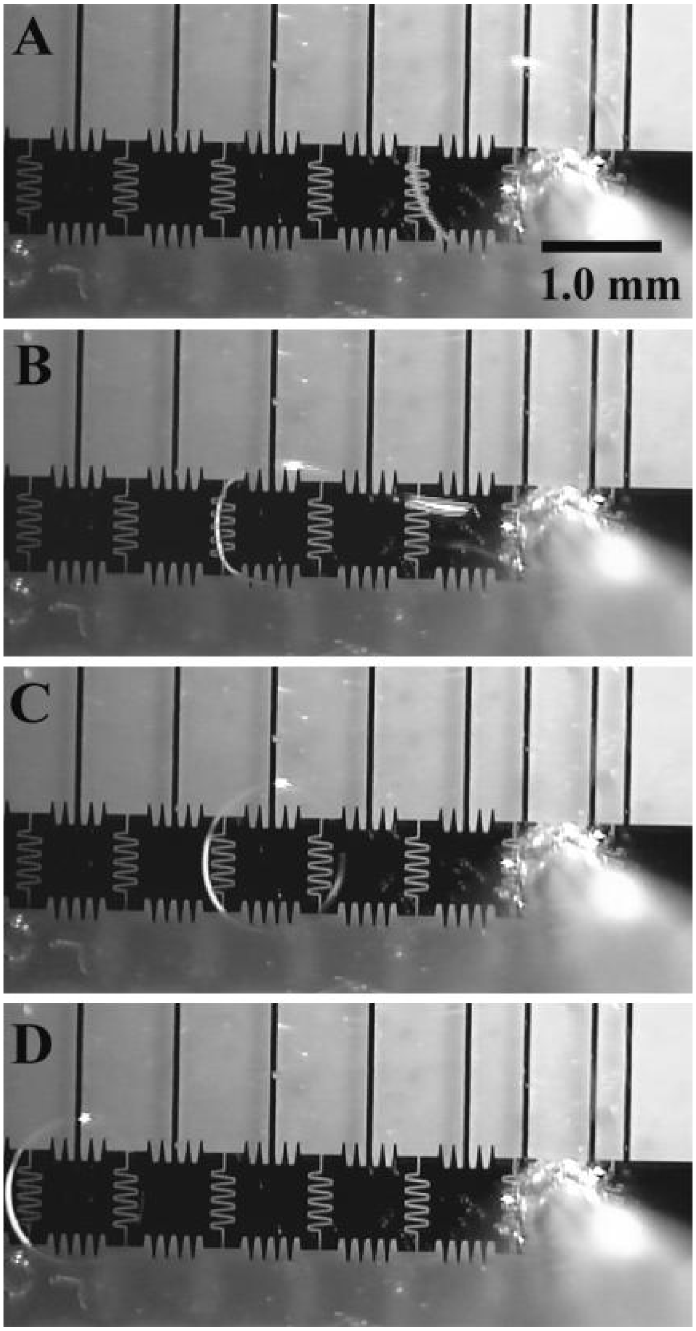

Figure 5.4: Time-lapse series of automatic droplet generation using an external pressure source

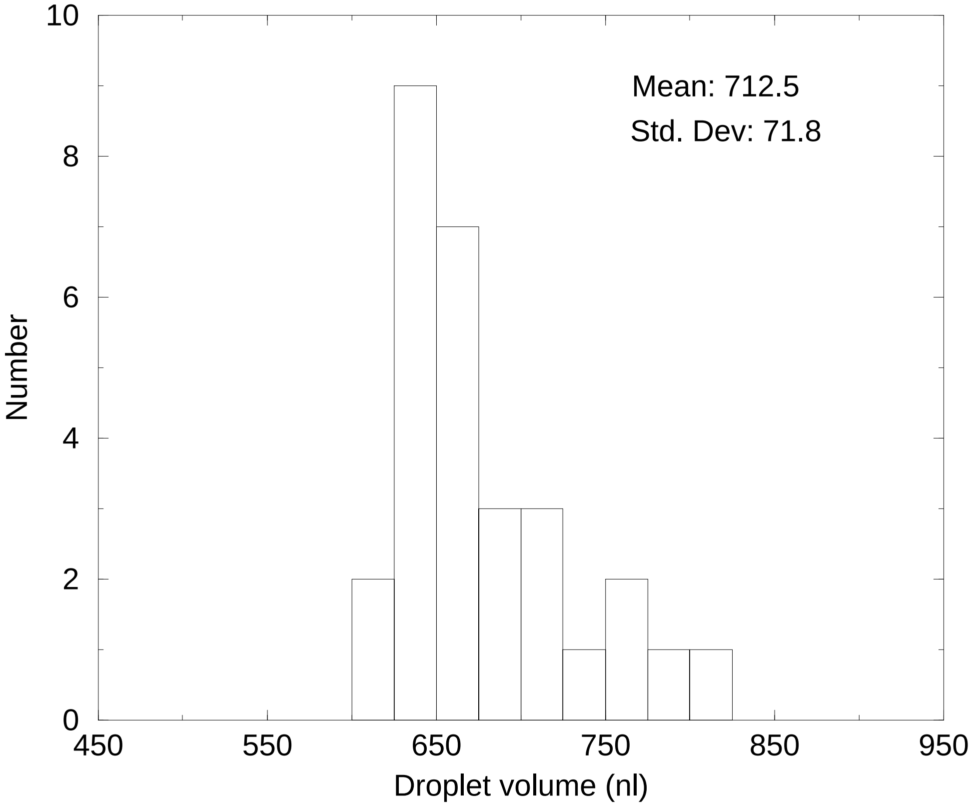

Figure 5.5: Histogram of automatically generated droplet volumes using the external pressure assist system (bin size = 25)

were recorded towards the end of the experiment at which point several electrodes had begun to deteriotate resulting in significantly greater variation than was present earlier in the experiment. The maximum droplet generation frequency we achieved was about 4 Hz, although much higher frequencies can likely be obtained through fine tuning of the system parameters. We expect that the turn-on time of the mechanical valve and retraction speed of the liquid meniscus may be the rate limiting factors. The retraction speed may be substantially improved if a vacuum pump is added to generate negative pressure for removal of the liquid from the gap. Furthermore, improved electrode designs and higher electrowetting forces may allow for continuous droplet formation without the need for pneumatic switching.

5.1.3 Droplet Splitting

Droplets may be split by applying voltage to non-adjacent electrodes beneath the droplet. This process is illustrated in Figure 5.6. A droplet with volume sufficient to cover two electrodes is initially relaxed and positioned at a series of three electrodes (Figure 5.6A). The left and center electrodes are energized and the droplet spreads across the area of both electrodes (Figure 5.6B). Next, the center electrode is de-energized at the same time that the right electrode is energized, and the droplet is split into two (Figure 5.6C,D). Finally, the sequence is reversed and the original droplet is reassembled by merging the two smaller droplets back together (Figure 5.6E,F).

During the course of our experiments, we often used this technique to refine the volume of droplets for transport experiments. However, we did not study the dynamics of the droplet splitting and merging processs. Since droplet splitting requires the formation of new fluid-fluid interface, we would expect that reducing the energy per length of the droplet contour would facilitate splitting. Thus, the use of silicone oil and smaller gap heights should be considered for systems in which droplet splitting is a necessary operation. We

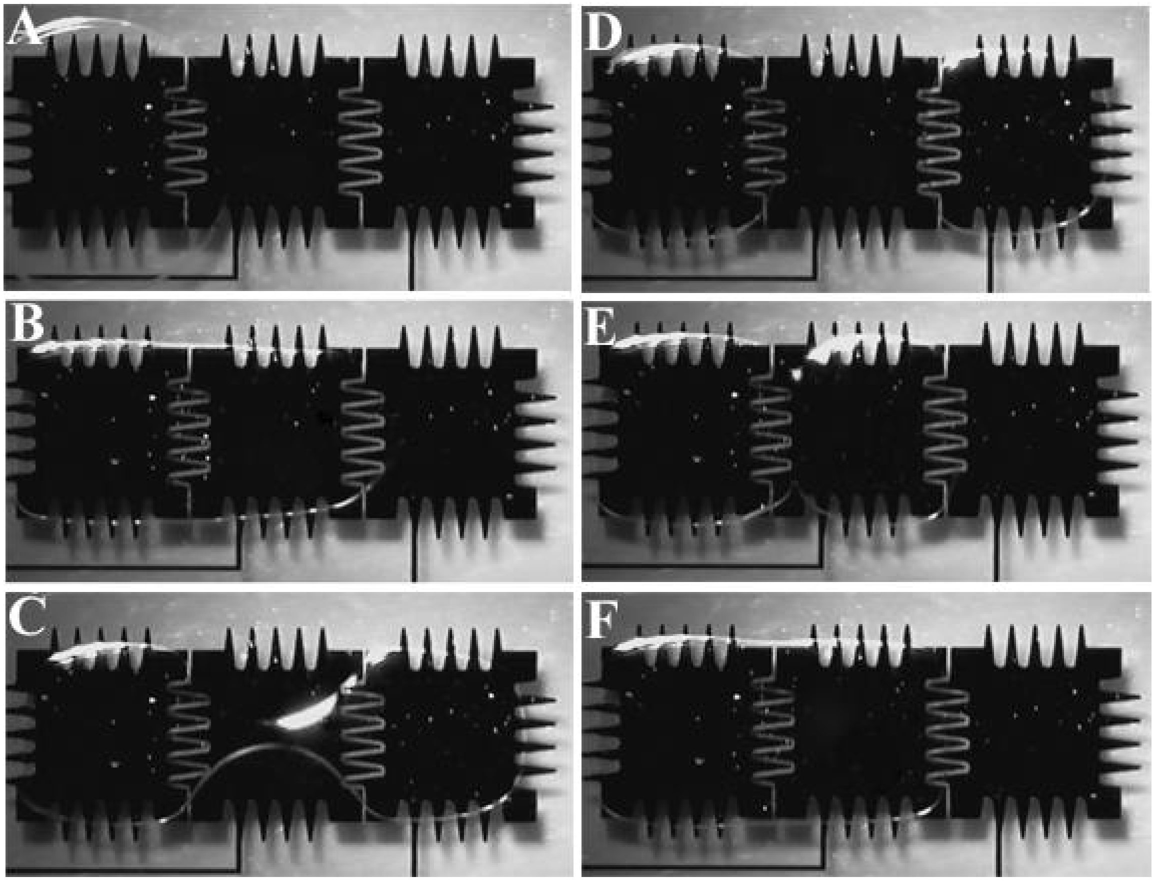

Figure 5.6: Time-lapse series of droplet splitting and merging

also expect that improved electrode designs may increase the speed and repeatibility of these processes.

5.2 Capacitive Droplet Detection

While there are several methods that might be used for droplet detection, capacitive sensing is particularly well-suited for electrowetting-based systems. The capacitive nature of the underlying phenomenon guarantees that large capacitive changes will be associated with the presence or absence of a droplet above a particular electrode. Unlike optical methods, capacitive sensing places no constraints on the position or orientation of the sensor hardware with respect to the chip. The use of control electodes for both actuation and capacitive sensing provides a detection system which is inherently integrated and aligned. Since the strength of the capacitance signal is proportional to the area of overlap between the sensing electrode and droplet, both qualitative and quantitative information concerning the relative position of the droplet are obtained.

Capacitive sensing may be used in several ways to enhance the reliability and performance of digital microfluidic systems. Capacitive sensing may simply give an indication of whether a droplet is present at a particular location or has crossed a particular point in a flow pathway. Alternatively, when each electrode in a flow pathway is monitored, switching rates may be dynamically controlled to maximize droplet flow rates. Quantitative capacitance measurements may be used for control of volume during droplet formation or to monitor the physical integrity of droplets during transport. The use of capacitive feedback during droplet formation and aliquoting not only ensures greater consistency, but allows more redundant use of electrode structures. That is, a range of droplet volumes may be generated using a single set of electrodes. Finally, capacitive sensing is an important tool for fundamental studies of droplet dynamics, providing data on a time-scale not accessible by conventional videomicroscopy. For example, a capacitive method for investigating both static and dynamic electrowetting behavior on solid surfaces was recently demonstrated by Verheijen and Prins [44].

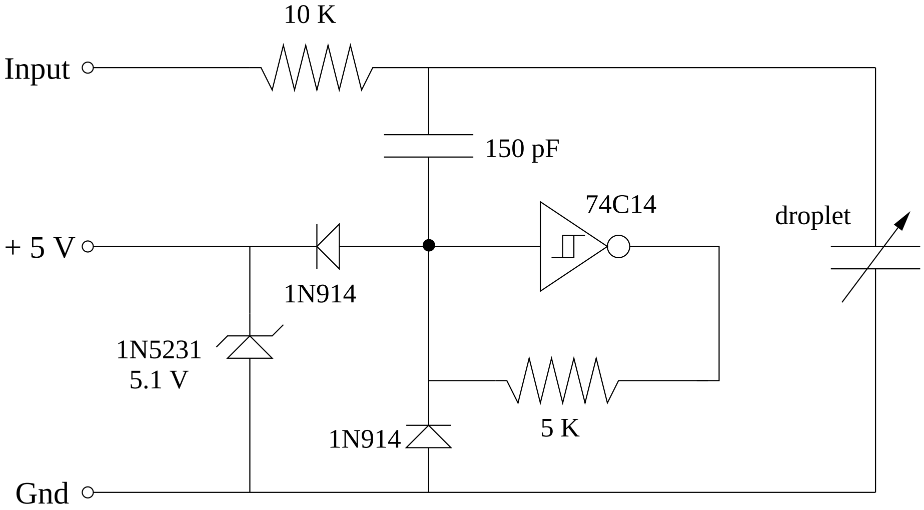

Figure 5.7: Ring-oscillator circuit for capacitance measurements of droplets

A new controller setup was devised for making capacitance measurements of droplets. A multifunction data aquisition and control board (CIO-DAS08, Omega Engineering) was used to digitally control a bank of four switches connected to the 120 V dc power supply. A capacitance controlled oscillator was connected to one of the outputs through a resistor and capacitor as shown in Figure 5.7. The capacitance between the control electrode and the ground plane modulates the frequency of the ring-oscillator. The frequency was measured using a counter on the data acquisition board with provided a maximum capacitance sampling rate of up to 10 KHz. The circuit was calibrated using capacitors of known value and a typical calibration curve is shown in Figure 5.8. The capacitance of the parylene insulation was approximately 3.5 nF/cm^2 and the area of a 1.5 mm pitch interdigitated electrode was 2.04 mm^2, giving a capacitance of 71 pF for a droplet that completely overlaps the electrode (neglecting fringing effects). Thus even this relatively simple oscillator circuit provides more than enough sensitivity for quantitative detection of droplets of this size.

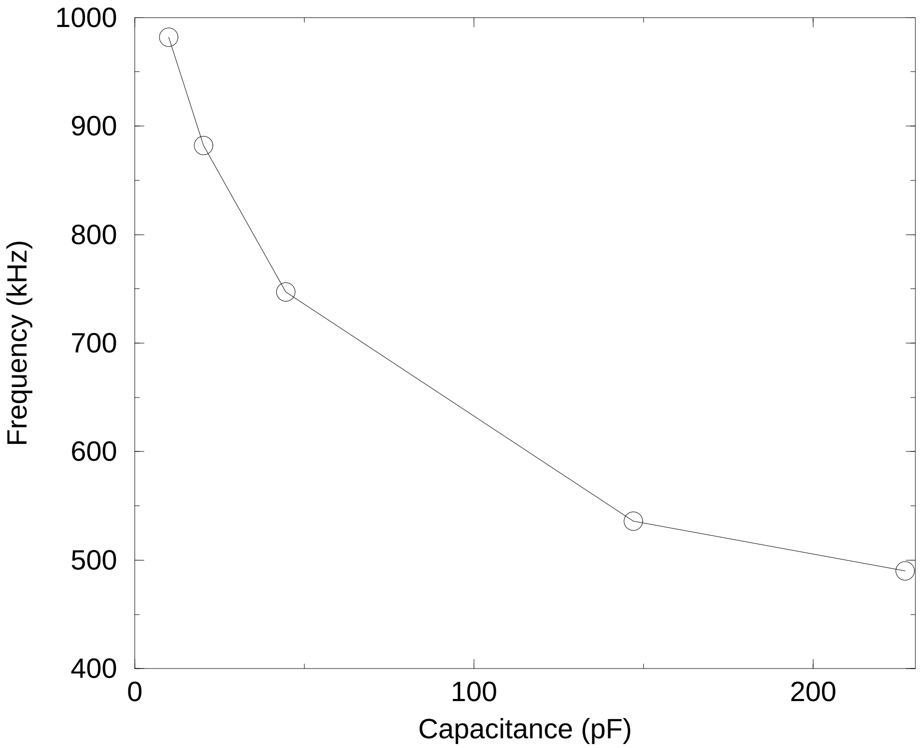

Figure 5.8: Capacitance calibration curve for ring-oscillator circuit

We measured the capacitance of 900 nl droplets of 100 mM KCl solution traveling across 1.5 mm electrodes in silicone oil. The droplet was programmed to oscillate across three electrodes at a switching rate of 2 Hz at various voltages with capacitance measurements being made on the center electrode at a sampling rate of 200 Hz. A portion of the resulting normalized capacitance trace at four voltages is shown in Figure 5.9. Peaks corresponding to the presence of the droplet are easily discernible. At the lowest voltage (top trace), the droplet was incompletely transferred to one of the side electrodes (i.e. it was below voltage threshold) producing pairs of merged peaks in this trace. However, at higher voltages the droplet is completely transferred each time and we observe that the width of the peak decreases with increasing voltage. Although the two peaks corresponding to different directions of transfer have slightly different shapes, these shapes are reproduced almost exactly each time that the electrode receives the droplet.

Peaks for each of the four voltages are superimposed in Figure 5.10. We note several unexpected features in the shape of these peaks. First, the capacitance does not appear to reach a stable maximum after the electrode has received the droplet, rather the capacitance continues to gradually increase until the next transfer cycle. This feature is consistent with other observations of ours that the measured capacitance of static droplets under applied voltage tends to drift over time. We do not observe any such drift when measuring discrete capacitors under voltage bias. Another unexpected feature is the spike seen during the early portion of the cycle when the droplet is initially transferred onto the electrode. The negative slope of the capacitance following this spike would seem to indicate a negative droplet velocity which is not consistent with either visual observations or theory. The spike may be caused by a transient deformation of the droplet of the sort observed during the video analysis experiments. Another possibility is that the spike is related to the dynamics of oil film formation and exclusion. When an oil film is present between the droplet and electrodes, the measured capacitance would be expected to decrease. Further fundamental

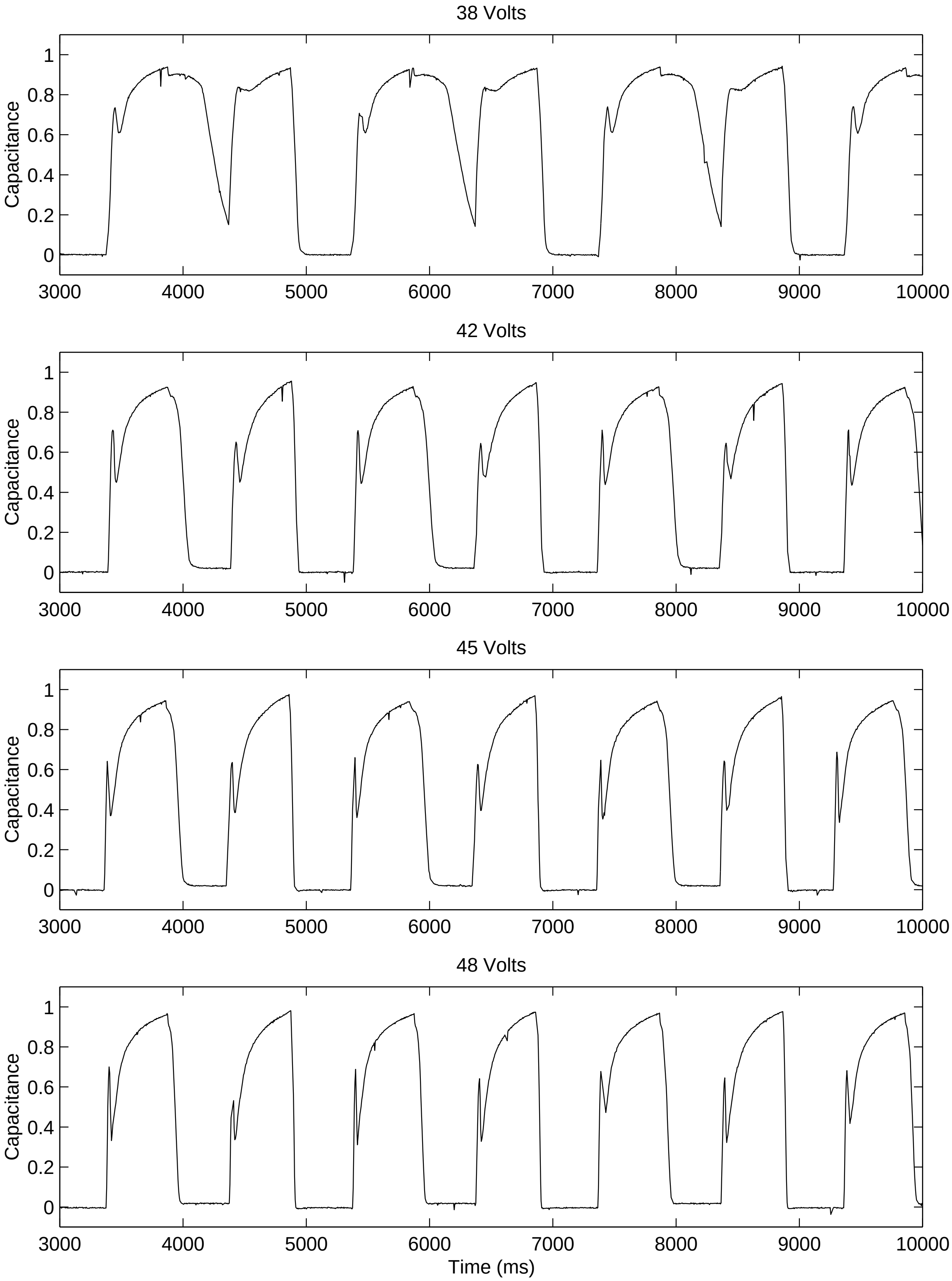

Figure 5.9: Normalized capacitance traces for a droplet moving across an electrode

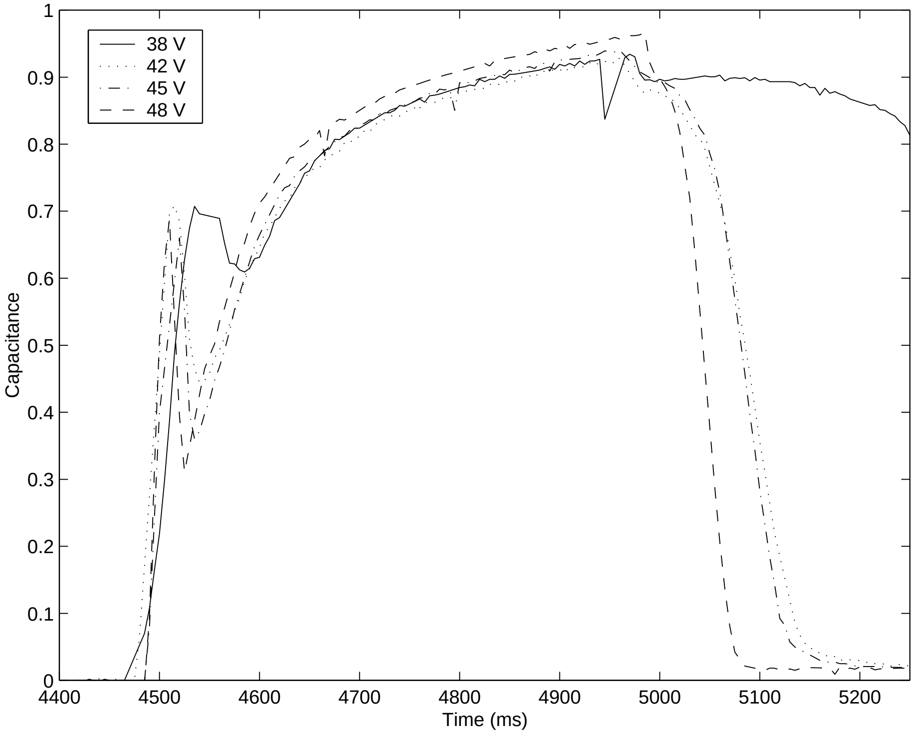

Figure 5.10: Superimposed capacitance peaks for a droplet moving across an electrode

studies are needed to ascertain the significance of each of these features, however, it is clear that capacitive detection provides a straightforward means of droplet detection for these systems.

5.3 Power Dissipation

In considering the design and operation of highly integrated systems, power dissipation may have a significant impact on system performance. For many applications in biology temperature control to 1 °C or better is desirable. Thus thermal dissipation considerations may determine system operating limits. In less sensitive applications, substantial heating or thermal gradients may alter droplet transport characteristics. Finally, an ultimate thermal limit is imposed by the boiling points of the liquids in the system.

To determine the power dissipated in the droplet during a single transfer we consider the energetics of charging the time-varying droplet capacitance. We take as our model system a 1 μl droplet of 100 mM KCl in silicone oil which is transferred between 1.5 mm pitch interdigitated electrodes at 30 V with a transport time of 100 ms. When fully covering the charged electrode the capacitance between the droplet and charged electrode (neglecting fringing fields) is approximately 50 pF. The parallel capacitance formed by the oil-filled gap is neglected since its capacitance is 100 – 1000 times smaller due to the larger plate separation. Additionally, to simplify the calculations, and initial overlap between the droplet and adjacent electrode is ignored so that the initial capacitance is taken to be 0 pF. Three resistances appear in series with the droplet capacitance (Figure 5.11). The largest resistance R_{wire} is due to the thin-film Cr wires between the bond pads and electrodes, while smaller resistances, R_{drop} and R_{ITO} are due to the resistance through the electrolyte and ITO ground plane respectively.

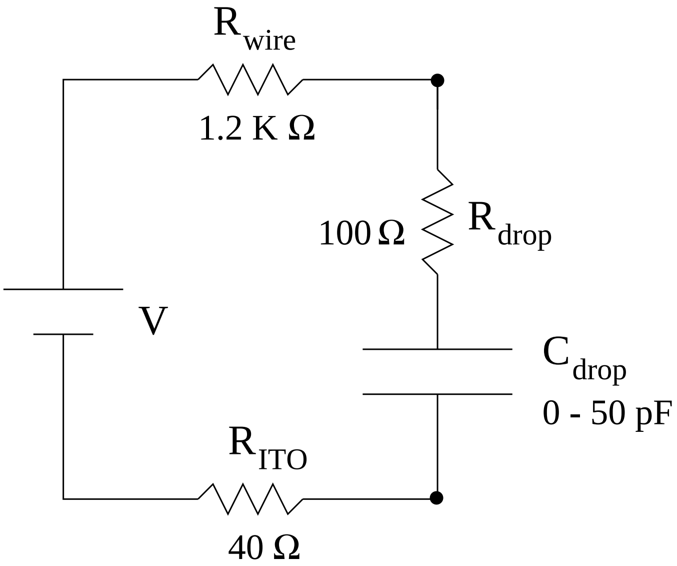

Figure 5.11: Equivalent electrical circuit of the droplet system during a single transfer

The current delivered to the droplet capacitor is given by:

$$i(t) = \frac{dq(t)}{dt} = V(t)\frac{dC(t)}{dt} + C(t)\frac{dV(t)}{dt} \tag{5.1}$$

We consider the component due to charging of the time-varying capacitance. Since the electrical RC time constant is small ($< 1\ \mu$s) compared the time-scale over which C varies, we neglect the voltage time-dependence and find that the instantaneous power delivered to the time-varying capacitance is $P(t) = V_0^2 \frac{dC(t)}{dt}$ where V_0 is the supply voltage. The total work of changing the capacitance is therefore $V_0^2 C_f$, where C_f is the final capacitance, and the average power dissipation is $V_0^2 C_f/T$ where T is the period over which the capacitance changes. This energy constitutes the total mechanical work done to the droplet system and is dissipated through a combination of viscous, inertial and chemical processes in the droplet.

For the model system described above the average power dissipation is approximately 500 nW and the total energy consumption is about 50 nJ per droplet transfer. We note that the kinetic energy of a 1 mg point-mass with velocity 1.5 cm/s is approximately 0.1

nJ. Thus it appears that viscous and physico-chemical processes at the moving contact-line, rather than purely inertial ones are responsible for the bulk of the mechanical energy dissipation. We also note that the gravitational potential energy associated with raising a 1 mg mass a distance of 1.5 mm is approximately 15 nJ which is a significant fraction of the total energy for droplet transfer. Thus there may exist some gravity dependent effects for droplets at this size scale.

In addition to mechanical power dissipation associated with droplet motion some electrical power is dissipated within the droplet due to the resistance of the electrolyte. The total energy resistively dissipated in the droplet is $C_f V_0^2 \frac{R_{drop}}{R_{tot}}$, where R_{tot} is the total series resistance seen by the source. In this example the total energy is 3.4 nJ and the average electrical power dissipation within the droplet is 34 nW. We now consider the effect of total power dissipation on heating of the droplet. We assume for now that all energy dissipated in the droplet is ultimately converted to heat and that no heat is transferred from the droplet to its environment. In this case, approximately 78,000 cycles or over 2 hours of continuous transport would be required to raise the temperature of the droplet by 1 °C. With respect to scaling we find that for the same average linear velocity, the energy dissipated per transfer decreases with the square of the linear scale while the average power dissipation decreases linearly. Since the volume decreases cubically the rate of heating is expected to increase quadratically. However, considering that lower linear velocities may be acceptable at smaller scales and allowing for dissipation of heat to the environment it seems unlikely that significant heating should exist even for droplets of sub-nanoliter volumes. These results demonstrate the high efficiency of electrowetting-based microactuation.

5.4 Droplet Stability

The question of whether the droplet leaves a residual film of material behind as it moves across the solid surface has important implications for the serviceability of droplet-based microfludic systems. Loss of material from the droplet may have at least three adverse consequences on system performance. First, the reduction in volume resulting from the loss of liquid may alter the dynamics of, or even altogether impede, droplet transport. Over thousands of cycles the cumulative effect of losing a small amount of liquid at each step can obviously become significant. Secondly, if the residual film is compositionally different from the bulk liquid, for example more ionic or more surface active, then the composition and dynamics of the droplet may vary over time even if the total change in volume is relatively small. Furthermore, even if the droplet dynamics are unaffected, enrichment or depletion of certain classes of molecules, for example proteins or nucleic acids, may adversely impact system serviceability. Finally, material lost from one droplet may be transmitted to and contaminate other droplets in the system. This transmission could occur through the oil or solid surface, or in gas filled systems, by evaporation and condensation processes. The acceptable limits of contamination are application and system specific, but we do note that in some cases these limits can be quite low.

Quéré [71] studied the residual films left by droplets of alkanes moving within 0.9 mm diameter Teflon tubes in air. The alkanes partially wetted the Teflon with contact angles ranging between 10° and 50°. Two regimes were observed: at low velocity no macroscopic (> 500 Å) film was observed, while above a threshold velocity a macroscopic film (1 – 10 μm) appeared with thickness increasing with velocity. The threshold for the transition was in the range 1 – 20 mm/s and was approximately proportional to θ_R^3. Extrapolation of these results to water with $\theta_R \approx 100^\circ$ would indicate a threshold velocity around 900 mm/s, although it is not clear whether such an extrapolation is valid for large values of θ_R. In any case, Quéré also found that in the apparently "dry" regime a thin film (~ 20 Å) which was independent of the fluid velocity was also present.

If we consider the effects of this dry regime film on a cylindrical droplet with diameter 1.0 mm, height 0.3 mm and volume 236 nl sandwiched between two plates, and assume that a thin residual film of rectangular dimensions 1.0 mm x 1.0 mm x 20 Å is deposited on both plates each time the droplet moves, then the volume loss per transfer is only 4 fl. Even after traveling a distance of over one million droplet diameters, the volume would be diminished by less than 2%. Thus, this regime of loss seems unlikely to result in significant volume reduction. In the course of our experiments we have transferred a single droplet of 100 mM KCl solution over 100,000 times between sets of three or four electrodes without discernible change in volume. Certainly, any residual film on the solid surface in these experiments may simply be recycled as the droplet flows in a small closed loop, however, this observation would at least seem to rule out significant loss of liquid to the oil phase.

We conducted an experiment to determine whether we could detect any loss of material from a moving droplet. Two 900 nl 100 mM KCl droplets were placed on a linear array (1.5 mm pitch) and programmed to flow along intersecting pathways as illustrated in Figure 5.12. Thus, the center electrode in the pathway received each droplet at different times during the cycle. A fluorescent dye (fluorescein) was added to one of the droplets. After 620 complete cycles of intersecting flow, we were not able to detect that any fluorescence had been transferred to the other droplet, or to the oil or surfaces around the droplets (Figure 5.13). Although we did not quantify the fluorescence signal and the number of cycles was relatively low, these results suggest that at least macroscopic residual films are not likely to be present.

Another experiment was performed to determine whether the conductive ions in the droplet could migrate into the insulating oil phase and contaminate it. For each of seven different ionic salts, 100 mM solutions were made and the resistivity was measured using a handheld digital conductometer (Table 5.1). The resistivity of most of the solutions was

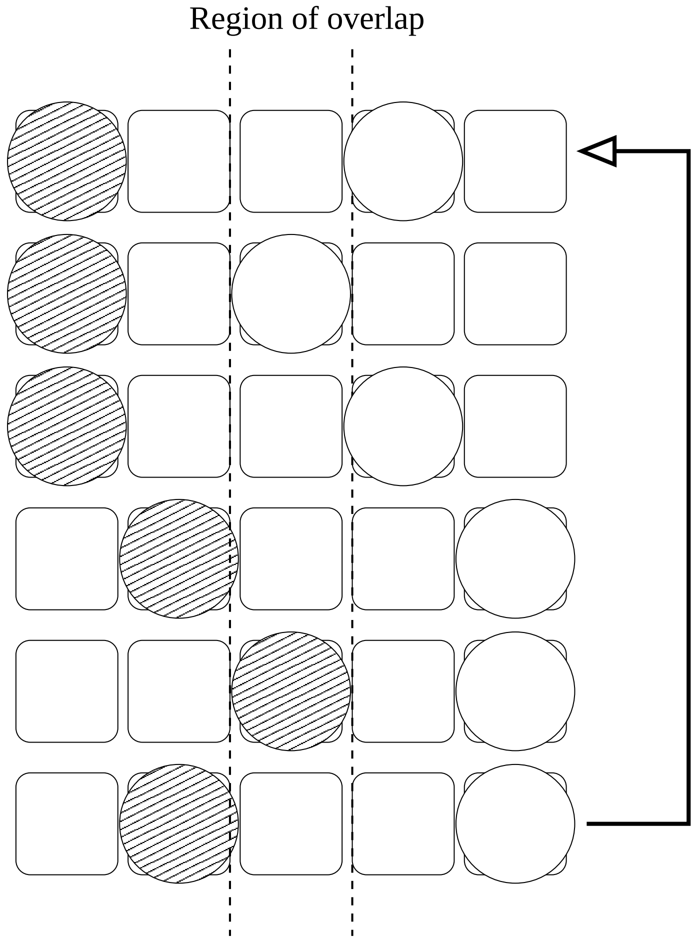

Figure 5.12: Droplet flow pattern for cross-contamination experiment. Each horizontal row shows the position of both droplets during one step of the cycle.

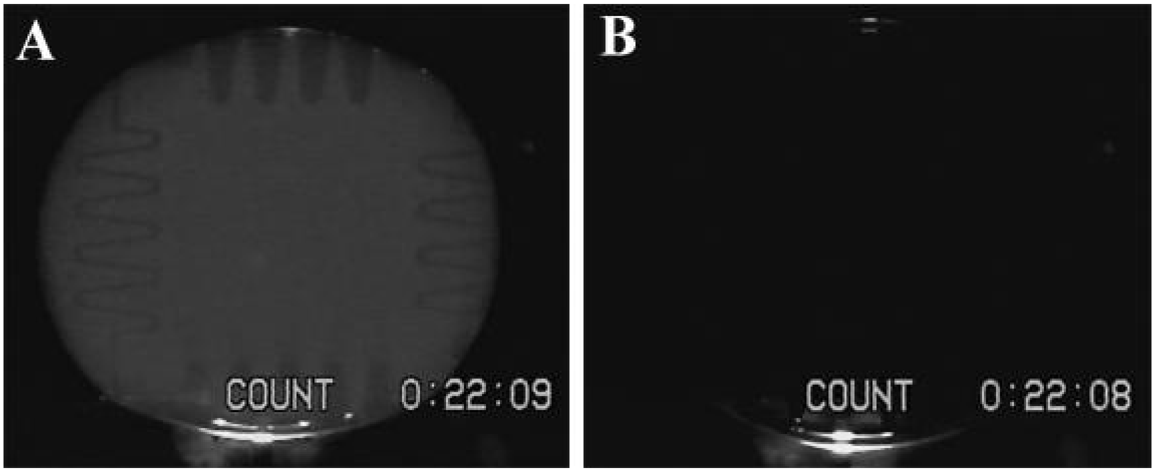

Figure 5.13: Fluorescent (A) and non-fluorescent (B) droplets after 620 cycles of intersecting flow

Salt solution (100 mM)	**Resistivity (Ω·cm)**
Ammonium acetate ($NH_4C_2H_3O_2$)	128.2
Ammonium chloride (NH_4Cl)	93.9
Potassium chloride (KCl)	93.6
Potassium phosphate dibasic (K_2HPO_4)	69.2
Potassium phosphate monobasic (KH_2PO_4)	136.4
Sodium acetate ($NaC_2H_3O_2$)	159.5
Sodium nitrate ($NaNO_2$)	114.7

Table 5.1: Resistivity of 100 mM ionic salt solutions

approximately 100 Ω·cm. Thus, our standard 900 nl 100 mM KCl droplet provides a resistance of about 100 Ω between the ground plate and insulator surface.

The resistivity of the silicone oil was also measured, and found to exceed the detection limit ($>$ 20 MΩ·cm) of the instrument as expected (nominal value: 10^9 MΩ·cm). Equal volumes of oil and each of the salt solutions were then placed in vials and left overnight on a rotary mixer. The resistivity of the oils was then remeasured, and in all cases the resistivity of the oil remained above the detectable limit of the conductometer, indicating that the dielectric properties of the oil were not compromised by mixing with the salt solutions. Thus it appears that at least for the silicone oil/aqueous electrolyte system, the

Solvent	Specific gravity	Surface tension (mN/m)	Evap. rate (BuAc=1)	Visc. (cP)
Acetone (C_3H_6O)	0.79	24.0	7.7	0.30
Acetonitrile (CH_3CN)	0.79	28.7	5.8	0.34
Chloroform ($CHCl_3$)	1.48	27.5	11.6	0.58
Dimethylformamide (C_3H_7NO)	0.95	36.8	0.2	0.92
Ethyl acetate ($CH_3COOC_2H_5$)	0.90	23.4	6.0	0.46
Ethanol (C_2H_5OH)	0.79	22.0	2.7	1.20
Ethyl ether ($C_4H_{10}O$)	0.71	17.1	37.5	0.25
Methanol (CH_3OH)	0.80	22.7	5.9	0.59
Methylene chloride (CH_2Cl_2)	1.33	27.8	27.5	0.40
Tetrahydrofuran (C_4H_8O)	0.88	26.4	8.0	0.55
Toluene (C_7H_8)	0.86	28.4	2.2	0.59
Water (H_2O)	1.00	72.8	0.3	1.00

Table 5.2: Physical properties of solvents tested for electrowetting compatibility. From [72] [73] and manufacturer's MSDS's

droplets are extremely stable throughout the manipulations.

5.5 Solvent Compatibility

As the microliquid handling capabilities of electrowetting-based systems are quite general and flexible, the range of applications may largely be limited by issues of solvent and material compatibility. Eleven commonly used solvents (in addition to water) were investigated to determine their compatibility with electrowetting microactuation. The solvents and their physical properties are listed in Table 5.2. With the exception of the dimethylformamide (DMF) all of the selected solvents evaporate much more rapidly than water. For example, submicroliter quantities of ethyl ether tend to evaporate completely within a fraction of a second. For this practical reason, the solvents were not tested in air, and were only tested with suitable immiscible filler fluids. Thus, the first step was to determine to miscibility of each solvent with the available filler fluids.

Miscibility Testing

The miscibility of each solvent with the inert media was tested by first filling a 0.3 mm gap between Teflon AF coated glass plates with the filler fluid. The solvent was then injected into the gap and the presence or absence of droplets within the fluid was taken to be an indication of the miscibility of the two liquids. No attempt was made to characterize the size or stability of these droplets. In this context, the term "miscibility" should be understood to refer to the result of this specific test only and not to any more general definition.

Conventional low viscosity silicone oil[1] was found to mix with all of the solvents except for water and acetonitrile. A fluorine containing silicone oil[2] was tried next and found to be immiscible only with water. Better results were obtained with an "organic" silicone[3] which was immiscible with half of the solvents tested. The high viscosity of the organosilicone oil (~ 50 cSt.) made it problematic as a filler fluid, but a blend of equal parts 1 cSt. conventional silicone oil and organosilicone oil had similar miscibility properties with reduced viscosity. The alkanes hexane and dodecane were also investigated and found to have miscibility similar to conventional silicone oil. The results of miscibility testing are summarized in Table 5.3.

Of all the fluids investigated, the perfluorinated solvent FC-75 gave the best results, being immiscible with all solvents except for ethyl ether. However, since FC-75 is also a solvent for Teflon AF, its use is incompatible with the present technology. Attempts to render Teflon AF insoluble through extending curing (up to 3 hours at 250 °C) tended to have a modest effect upon the solubility of Teflon AF in FC-75, but severly degraded the parylene layer. Other perfluorinated solvents would be expected to give similar results both in terms of solvent and Teflon AF solubility.

---

[1] Trimethylsiloxy terminated polydimethylsiloxane (DMS-T01, Gelest)

[2] Poly 3,3,3-trifluoropropylmethylsiloxane (FMS-121, Gelest)

[3] 95% decylmethylsiloxane - 5% butylated aryloxypropylmethylsiloxane (ALT-251, Gelest)

	Conv. SO	**Fluor. SO**	**Organ. SO**	**SO blend**	**Dodecane & hexane**	**FC-75**
Acetone	X	X	O	X	X	O
Acetonitrile	O	X	O	O	O	O
Chloroform	X	X	X	X	X	O
DMF	X	X	O	O	O	O
Ethyl acetate	X	X	X	X	X	O
Ethanol	X	X	O	O	X	O
Ethyl ether	X	X	X	X	X	X
Methanol	X	X	O	O	X	O
Methylene Cl	X	X	X	X	X	O
THF	X	X	X	X	X	O
Toluene	X	X	X	X	X	O
Water	O	O	O	O	O	O

Table 5.3: Results of miscibility testing. X=mixing, O=no mixing, SO=silicone oil

Electrowetting Testing

Transport of droplets within the silicone oil blend fluid was tested for each of the five immiscible solvents using the standard system geometry. Solvents were made conductive by the addition of 100 mM ammonium hexafluorophosphate (NH_4PF_6) salt. The non-aqueous solvents could not be transferred between electrodes at any value of dc voltage. Upon application of voltage, these droplets were observed to initially shift slightly towards the energized electrode and then stop or retract. Manual pulsing of the voltage, however, did result in complete transfer of the droplets.

High frequency ac square-wave voltage signals (1 – 40 KHz) were generated by rapid computer-controlled switching of the electrode voltage. It was found that droplets of all five solvents could be smoothly transferred using these ac voltages. However, meniscus instabilities were observed for the non-aqeuous solvents under these conditions. Actuation of droplets of ethanol or methanol resulted in the expulsion of microdroplets from the perimeter of the main droplet. These ejected microdroplets coalesce into progressively larger droplets (Figure 5.14) as they diffuse away from the main droplet. The region around the

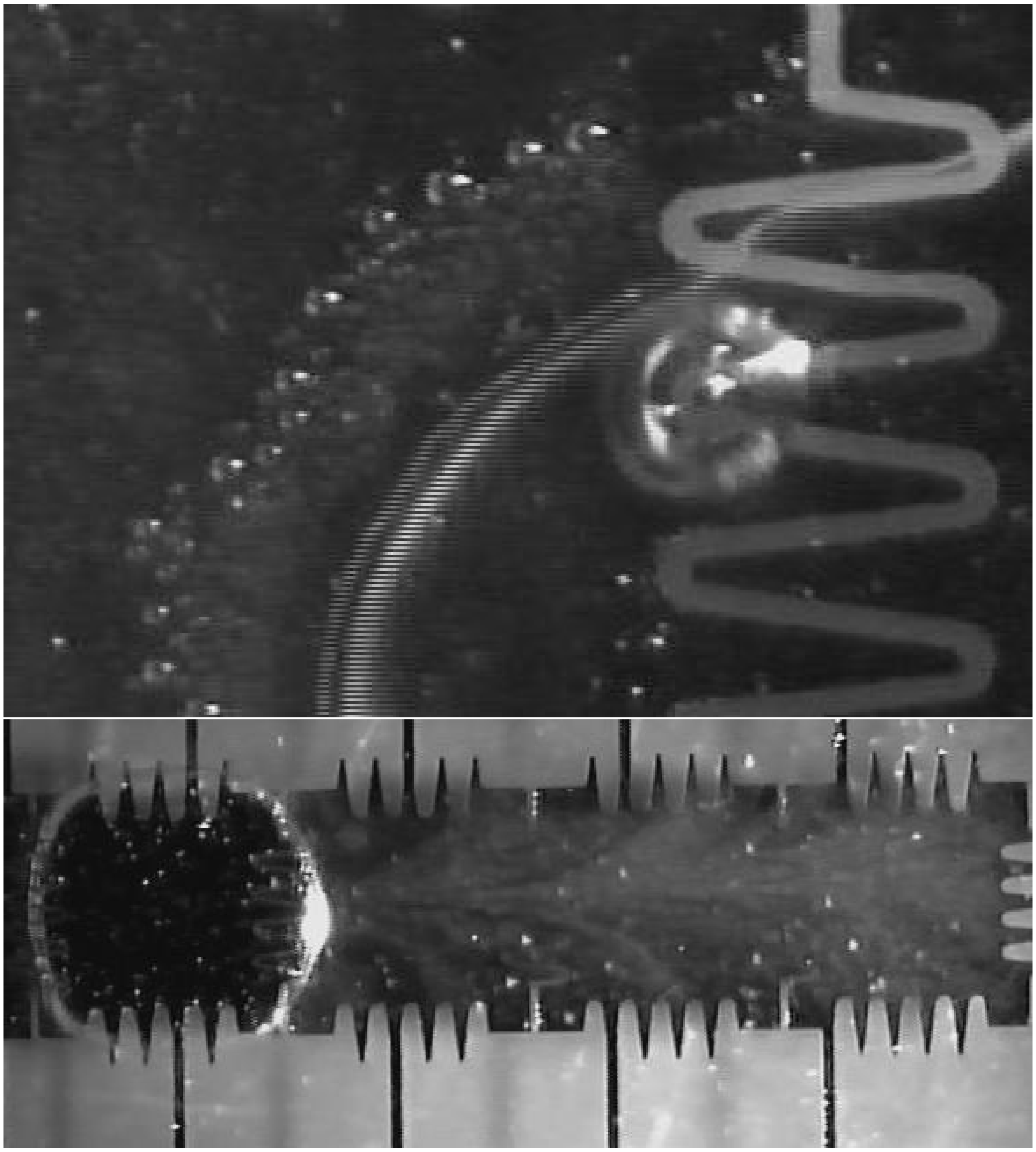

Figure 5.14: Instability of non-aqueous solvent droplets. The top image shows a droplet of ethanol at lower right which is ringed by smaller droplets formed from coalescing ejected microdroplets. The lower image shows a droplet of acetonitrile leaving behind cloudy trails as in moves through viscous oil.

main droplet becomes cloudy with what we presume are suspended microscopic droplets. We did not observe the larger droplets with DMF or acetonitrile, but repeated movement of these solvents left a cloudy residue in the oil (Figure 5.14). When acetonitrile droplets were transported in low viscosity (1 cSt.) conventional silicone oil using 10 KHz ac voltage no cloudiness was observed. Transfer rates for water and acetonitrile under ac voltage are compared in Figure 5.15. Significantly higher rates are obtained for acetonitrile although these droplets are immobile in response to dc voltage.

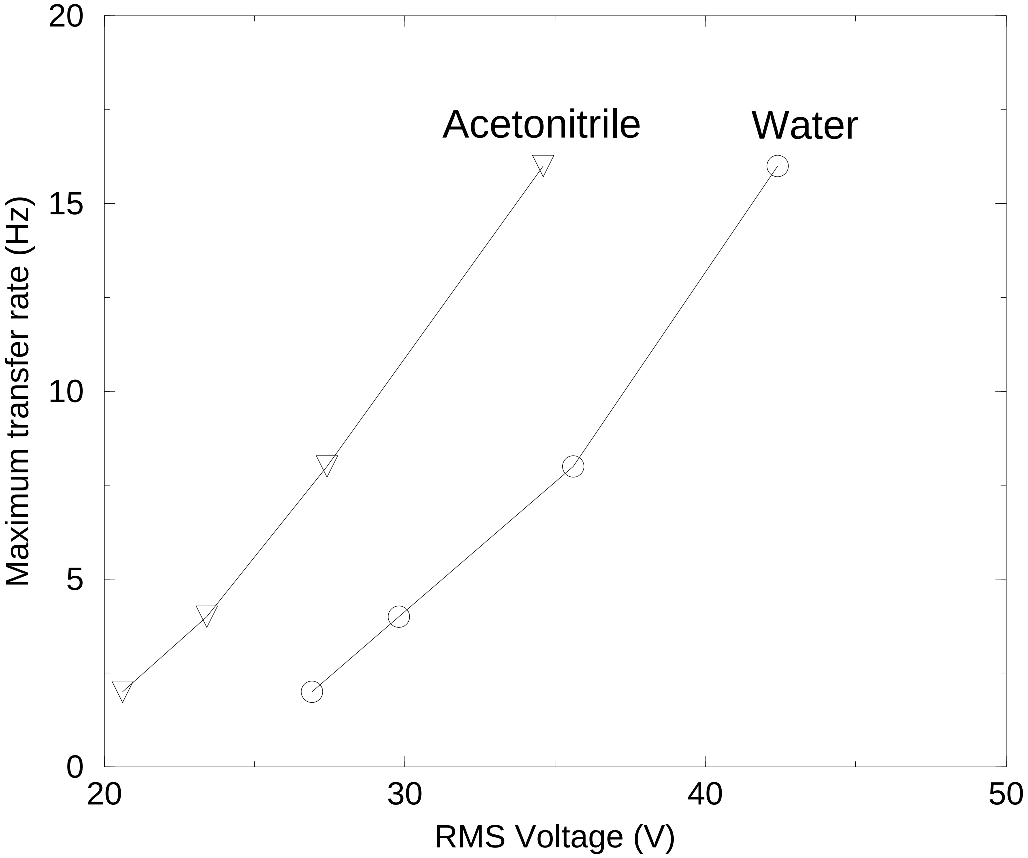

Figure 5.15: Comparison of transfer rates for water and acetonitrile

This droplet expulsion phenomenon has been reported by others for electrowetting of pure water and ethanol droplets on polymer films [39], although addition of small amounts of salt to the pure water was reported to suppress the effect. Vallet *et al.* [48] have performed an stability analysis of the charged contact line in which the electrostatic energy gained by a periodically distorted wetting line is compared to the surface energy cost of the deformation. This analysis, as well as other experimental observations, indicate that the size of the expelled droplets should be on the same order as the insulator thickness. Due to optical limitations, we are not able to determine the size of the expelled droplets in our system, although 1 μm appears to be a reasonable order of magnitude estimate.

5.6 Chapter Summary and Conclusions

This chapter demonstrated the feasibility of several important operations related to the implementation of practical digital microfluidic systems. The formation of transportable microdroplets from a larger liquid reservoir or source was demonstrated. Droplets were formed with some difficulty using only electrowetting forces, but could be generated in a rapid and automated fashion when an external pressure source was coupled to the electrowetting system. In both cases, specific recommendations were made for improving the speed and consistency of this operation. We also studied the use of capacitive sensing as a technique for detecting the motion and position of microdroplets within the array. Fairly sensitive real-time detection was achieved using a simple capacitance-controlled oscillator circuit. The capacitance traces demonstrated certain unexpected dynamic characteristics which warrant further fundamental capacitance studies of the droplet transport process. An analysis of power dissipation illustrates the high efficiency of electrowetting microactuation with less than 50 nJ of energy required per transfer within our model system. The associated average power dissipation of 500 nW is shown to be insufficient to lead to appreciable heating of the droplet.

Issues of droplet stability and contamination were investigated for the aqueous electrolyte/silicone oil system. We were not able to detect any degradation of the droplet, or cross-contamination between separate droplets during these experiments. However, when transport of non-aqueous droplets was attempted, expulsion of microdroplets from the perimeter of the main droplet was observed. The non-aqueous droplets could be transported with ac voltages but not dc voltages. However, based upon results with acetonitrile, the high viscosity of the oil may have contributed to the instability effect by limiting other enegy dissipation channels. Filler fluids which are immiscible with both non-aqueous solvents and Teflon AF need to be identified for future work on solvent compatibility. Alternative hydrophobic coatings may permit the use of perfluorinated liquids, but are likely to provide less chemical resistance than Teflon AF. Thus, issues of solvent compatibility and materials design are closely linked and need to be addressed in concert.

Chapter 6

Future Work and Conclusions

6.1 Future Work

There are many opportunities and directions for future development of this technology. The underlying physics of electrowetting and wetting kinetics are still relatively poorly understood and fundamental physical studies are needed in this area. In particular, non-ideal effects at high electric fields such as contact angle saturation and wetting line instabilities demand further investigation. Meniscus instabilities may impose limits on the types of solvents that can manipulated and thus limit the range of applications for this technology. Further physical studies would also begin to elucidate the processes at the moving contact line, and enable the development of meaningful models for droplet transport.

Materials issues have played a central role in this work and will continue to be an important aspect of future research. Insulator degradation is a serious problem which may ultimately limit the reliability and performance of electrowetting-based microactuators. A better understanding of its origin may allow optimization of materials or voltage protocols to minimize the effect. Electrowetting is a demanding application for insulator materials that requires a special combination of electrical, mechanical and chemical properties. Some applications may have additional surface chemistry requirements and alternative hydrophobic coatings may need to be developed. One limitation of Teflon AF was that it barred the use of perfluorinated liquids as a convenient medium for non-aqueous solvents. An alternative top-coating might allow perfluorinated liquids to be used in place of silicone oil which would permit microactuation of more types of solvents. However, the problem of simultaneously satisfying insulation, electrowetting, solvent and application-specific material demands will continue to be very challenging and trade-offs are inevitable. Alternative insulator materials may also be investigated with the aim of improving the dielectric reliability or reducing the system voltage to lower levels. High dielectric constant materials such as barium-strontium-titanate may ultimately permit system voltages below 5 V.

At the device level, further work on specialized structures and functions is needed, including implementation and characterization of operations such as mixing and optimization of droplet generation and splitting protocols and structures. The use of capacitance sensing methods for studying droplet transport dynamics should provide a more complete picture of the actual time-dependent behavior of moving droplets. The realization of more complex systems will require advances in both physical integration and architectural design. At present, the I/O count imposes a major limitation on the system size and complexity. Physical integration of the electrowetting system with control electronics would provide a means to achieve the next level of complexity and integration, while architectural innovations may reduce the required system size and I/O count. Additionally, integration of the electrowetting system with optical or electrical sensors or other microanalytical components will expand the range of possible applications. As more sophisticated systems are realized, design and simulation tools spanning the range from application design to droplet transfer modeling will be needed.

One of the more exciting areas for future research and development is the design and implementation of practical applications for digital microfluidics by electrowetting. The simple functionality of droplet generation and movement demonstrated here can serve as the basis for a class of useful applications. For example, Nanolytics (Raleigh, NC) is using this functionality to develop a platform for rapid and automated synthesis of oligonucleotide arrays on a chip as well as a microfluidics platform for high-throughput-screening applications. Another promising application is the manipulation of living cells using microdroplets as miniature test-tubes for sorting, fusing, or analyzing single cells. This sort of application has the further advantage that the carrier liquid is an aqueous electrolyte

Method	**Vel. (mm/s)**	**Ref.**
Thermocapillary	20.00	[26]
Electrochemical	2.50	[24]
Electrostatic	0.40	[31]
Electrostatic	0.15	[32]
Photochemical	0.05	[25]
Electrowetting	> 100.00	

Table 6.1: Comparison of surface tension based droplet transport speeds

which has been shown here to work particularly well for electrowetting. As the range and sophistication of electrowetting-based microfluidic systems is expanded, new applications will certainly become possible.

6.2 Conclusions

A new concept to facilitate higher levels of organization and complexity in microfluidic systems was proposed and a novel microactuator based upon electrowetting was designed to enable this concept. This microactuator permits precise and independent handling of droplets using no pumps, valves or fixed channels and imposes only minimal constraints on the liquid being handled. Highly flexible and reconfigurable systems suitable for a wide range of applications may be realized using this technology.

The proposed microactuator was fabricated and tested to evaluate its feasibility for the implementation of digital microfluidic systems. Rapid, reliable and repeatable transport of liquid droplets over 10s or 100s of thousands of cycles in both oil and air media was demonstrated under many different experimental conditions. Maximum velocities of over 10 cm/s were obtained for droplets as small as a few nl and as large as several μl. These droplet velocities far exceed any previously reported values for surface tension driven flow of (non-metallic) droplets as demonstrated in Table 6.1.

Other critical functions including microdroplet generation, splitting and merging were also demonstrated. Thus, multiple classes of fluidic operations may be flexibly performed in a monolithic device using a single microactuator structure. Digital microfluidics by electrowetting, therefore, provides both a physical basis and an organizational principle for the design and implementation of increasingly powerful, complex and flexible microfluidic systems.

Bibliography

[1] M. Elwenspoek, T.S.J. Lammerink, R. Miyake, and J.H.J. Fluitman. Towards integrated microliquid handling systems. *J. Micromech. Microeng,*, 4:227–245, 1994.

[2] S. Shoji and M. Esahi. Microflow devices and systems. *J. Micromech. Microeng.*, 4:157–171, 1994.

[3] P. Gravesen, J. Branebjerg, and O.S. Jensen. Microfluidics - a review. *J. Micromech. Microeng.*, 3:168–182, 1993.

[4] C.H. Mastrangelo, M.A. Burns, and D.T. Burke. Microfabricated devices for genetic diagnostics. *Proc. of IEEE*, 86(8):1769–1787, 1998.

[5] M.A. Burns et al. Microfabricated structures for integrated DNA analysis. *Proc. Natl. Acad. Sci. USA*, 93:5556–5561, May 1996.

[6] D.T. Burke, M.A. Burns, and C. Mastrangelo. Microfabrication technologies for integrated nulceic acid analysis. *Genome Research*, 7:189–197, 1997.

[7] M.A. Burns et al. An integrated nanoliter DNA analysis device. *Science*, 282:484–487, 1998.

[8] D.J. Harrison et al. Capillary electrophoresis and sample injection system integrated on a planar glass chip. *Anal. Chem.*, 64:1926–1932, 1992.

[9] E.M.J. Verpoorte et al. Three-dimensional micro flow manifolds for miniaturized chemical analysis systems. *J. Micromech. Microeng.*, 4:246–256, 1994.

[10] A. Berg and T.S.J. Lammerink. Micro total analysis systems: Microfluidic aspects, integration concepts and applications. In A. Manz and H. Becker, editors, *Microsystem Technology in Chemistry and Life Sciences*, volume 194 of *Topics in Current Chemistry*, pages 21–49. Springer, 1998.

[11] C.G.J. Schabmueller, M. Koch, A.G.R. Evans, and A. Brunnschweiler. Design and fabrication of a microfluidic circuitboard. *J. Micromech. Microeng.*, 9:176–179, 1999.

[12] P.F. Man, D.K. Jones, and C.H. Mastrangelo. Microfluidic plastic interconnects for multi-bioanalysis chip modules. In *Proceedings of SPIE*, volume 3224, pages 196–200, 1997.

[13] C. González, S.D. Collins, and R.L. Smith. Fluidic interconnects for modular assembly of chemical microsystems. *Sensors and Actuators B*, 49:40–45, 1998.

[14] T. Bourouoina, A. Bossebœuf, and J.P. Grandchamp. Design and simulation of an electrostatic micropump for drug-delivery applications. *J. Micromech. Microeng.*, 7:186–188, 1997.

[15] T.K. Jun and C.J. Kim. Valveless pumping using traversing vapor bubbles in microchannels. *J. Appl. Phys.*, 83(11):5658–5664, June 1998.

[16] J. Evans, D. Liepmann, and A.P. Pisano. Planar laminar mixer. In *Proc.of IEEE Micro Electro Mechanical Systems*, pages 96–101, Nagoya, Japan, 1997.

[17] P.F. Man, C.H. Mastrangelo, M.A. Burns, and D.T. Burke. Microfabricated capillarity-driven stop valve and sample injector. In *Proceedings of IEEE Micro Electro Mechanical Systems (MEMS 98)*, pages 45–50, Heidelberg, Germany, 1998.

[18] J. Lee and C.J. Kim. Liquid micromotor driven by continuous electrowetting. In *Proc. of IEEE MEMS '98*, Heidelberg, Germany, pages 538–543, Jan 1998.

[19] M.K. Chaudhury and G.M. Whitesides. How to make water run uphill. *Science*, 256:1539–1541, Jun 1992.

[20] Ronald F. Probstein. *Physicochemical Hydrodynamics*. Butterworth-Heineman, Boston, MA, 1989.

[21] A.W. Adamson and A.P. Gast. *Physical Chemistry of Surfaces*. John Wiley and Sons, Inc., 6th edition, 1997.

[22] E.B. Dussan. On the spreading of liquids on solid surfaces: static and dynamic contact lines. *Ann. Rev. Fluid Mech.*, 11:371–400, 1979.

[23] C. Rosslee and N.L. Abbott. Active control of interfacial properties. *Current Opinion in Colloid and Interface Sciences*, 5:81–87, 2000.

[24] B.S. Gallardo et al. Electrochemical principles for active control of liquids on submillimeter scales. *Science*, 283:57–60, Jan 1999.

[25] K. Ichimura, S. Oh, and M. Nakagawa. Light-driven motion of liquids on a photoresponsive surface. *Science*, 288:1624–1626, 2000.

[26] T.S. Sammarco and M.A. Burns. Thermocapillary pumping of discrete drops in microfabricated analysis devices. *AIChE J.*, 45:350–366, 1999.

[27] T.S. Sammarco and M.A. Burns. Heat-transfer analysis of microfabricated thermocapillary pumping and reaction devices. *J. Micromech. Microeng.*, 10:42–55, 2000.

[28] G. Beni, S. Hackwood, and J.L Jackel. Continuous electrowetting effect. *Appl. Phys. Lett.*, 40(10):912–914, 1982.

[29] J.L. Jackel, S. Hackwood, and G. Beni. Electrowetting optical switch. *Appl. Phys. Lett.*, 40(1):4–6, 1982.

[30] M. Sato. Electrocapillarity optical switch. *IEICE Trans. Commun.*, E77-B(2):197–203, 1994.

[31] M. Washizu. Electrostatic actuation of liquid droplets for microreactor applications. *IEEE Transactions on Industry Applications*, 34(4):732–737, 1998.

[32] O. Sandre et al. Moving droplets on asymmetrically structured surfaces. *Physical Review E*, 60(3):2964–2971, Sept. 1999.

[33] G. Beni and S. Hackwood. Electro-wetting displays. *Appl. Phys. Lett.*, 38(4):207–209, 1981.

[34] G. Beni and M.A. Tenan. Dynamics of electrowetting displays. *J. Appl. Phys.*, 52(10):6011–6015, 1981.

[35] E. Colgate and H. Matsumoto. An investigation of electrowetting-based microactuation. *J. Vac. Sci. Technol. A*, 8(4):3625–2633, 1990.

[36] H. Matsumoto and J.E. Colgate. Preliminary investigation of micropumping based on electrical control of interfacial tension. In *Proc. of IEEE MEMS '90*, Napa Valley, CA, pages 105–110, Feb 1990.

[37] Marc Madou. *Fundamentals of Microfabrication*. CRC Press, Boca Raton, FL, 1997.

[38] C. Quilliet and B. Berge. Electrowetting: a recent outbreak. *Current Opinion in Colloid and Interface Science*, 6:(to be published), 2001.

[39] M. Vallet, B. Berge, and L. Vovelle. Electrowetting of water and aqueous solutions on poly(ethylene terephthalate) insulating films. *Polymer*, 37(12):2465–2470, 1996.

[40] B. Berge. Électrocapillarité et mouillage de films isolants par l'eau. *C. R. Acad. Sci. Paris, Série II*, pages 157–163, 1993.

[41] V. Peykov, A. Quinn, and J. Ralston. Electrowetting: a model for contact-angle saturation. *Colloid Polym. Sci.*, 278:789–793, 2000.

[42] W.J.J. Welters and L.G.J. Fokkink. Fast electrically switchable capillary effects. *Langmuir*, 14:1535–1538, 1998.

[43] H.J.J. Verheijen and M.W.J. Prins. Reversible electrowetting and trapping of charge: Model and experiments. *Langmuir*, 15:6616–6620, 1999.

[44] H.J.J. Verheijen and M.W.J. Prins. Contact angles and wetting velocity measured electrically. *Rev. Sci. Instr.*, 70(9):3688–3673, 1999.

[45] T.D. Blake, A. Clarke, and E.H. Stattersfield. An investigation of electrostatic assist in dynamic wetting. *Langmuir*, 16:2928–2935, 2000.

[46] M. Schneemilch, W.J.J. Welters, R.A. Hayes, and J. Ralston. Electrically induced changes in dynamic wettability. *Langmuir*, 16:2924–2927, 2000.

[47] B. Berge and J. Peseux. Variable focal lens controlled by an external voltage: An application of electrowetting. *Eur. Phys. J. E*, 3:159–163, 2000.

[48] M. Vallet, M. Vallade, and B. Berge. Limiting phenomena for the spreading of water on polymer films by electrowetting. *Eur. Phys. J. B.*, 11:583–591, 1999.

[49] B. Janocha, H. Bauser, C. Oehr, H. Brunner, and W. Göpel. Competitive electrowetting of polymer surfaces by water and decane. *Langmuir*, 16:3349–3354, 2000.

[50] R. Digilov. Charge-induced modification of contact angle: the secondary electrocapillary effect. *Langmuir*, 16:6719–6723, 2000.

[51] C.Y. Chang and S.M. Sze, editors. *ULSI Technology*. McGraw-Hill Co, Inc., 1996.

[52] Filmtronics. *Spin-on dopants - product information*, 1999.

[53] H.S. Nalwa, editor. *Handbook of Low and High Dielectric Constant Materials and Their Applications*. Academic Press, 1999.

[54] Paratronix Inc. http://www.paratronix.com/, Aug. 2000.

[55] P.R. Resnick and W.H. Buck. Teflon AF amorphous fluoropolymers. In J. Scheirs, editor, *Modern Fluoropolymers*, pages 397–419. John Wiley & Sons, 1997.

[56] Specialty Coating Systems. http://www.scscookson.com/parylene/, Oct. 2000.

[57] W.J.J. Welters. Personal Communication, February 2000.

[58] Walter Noll. *Chemistry and Technology of Silicones*. Academic Press Inc., New York, NY, 1968.

[59] B. Arkles. Tailoring surfaces with silanes. *Chemtech*, 7:766–768, 1977.

[60] H.J. Hovel. Transparency of thin metal films on semiconductor substrates. *J. Appl. Phys.*, 47(11):4968–4970, 1976.

[61] H. Klauk, J.R. Huang, J.A. Nichols, and T.N. Jackson. Ion-beam-deposited ultrathin transparent metal contacts. *Thin Solid Films*, 366:272–278, 2000.

[62] M. Stehr, S. Messner, H. Sandmaier, and R. Zengerle. The VAMP - a new device for handling liquids and gases. *Sensors and Actuators A*, 57:153–157, 1996.

[63] T.D. Blake. Dynamic contact angles and wetting kinetics. In J.C Berg, editor, *Wettability*, volume 49 of *Surfactant Science Series*, chapter 5, pages 251–309. Marcel Dekker, Inc., 1993.

[64] Gelest, Inc. *Silicone Fluids: Stable, Inert Media*, 1998.

[65] O.N.M. McCallion and M.J. Patel. Viscosity effects on nebulisation of aqueous solutions. *International Journal of Pharmaceutics*, 130:245–249, 1996.

[66] M.J. de Ruijter, J. De Coninck, and G. Oshanin. Droplet spreading: Partial wetting regime revisited. *Langmuir*, pages 2209–2216, 1999.

[67] M.J. de Ruijter, T.D. Blake, and J. De Coninck. Dynamic wetting studied by molecular modeling simulations of droplet spreading. *Langmuir*, 15:7836–7847, 1999.

[68] M.J. de Ruijter, M. Charlot, M. Voué, and J. De Coninck. Experimental evidence of several time scales in drop spreading. *Langmuir*, 16:2363–2368, 2000.

[69] M. Schneemilch, R.A. Hayes, J.G. Petrov, and J. Ralston. Dynamic wetting and dewetting of a low-energy surface by pure liquids. *Langmuir*, 14:7047–7051, 1998.

[70] T.D. Blake and J.M. Haynes. *J. Colloid Interface Sci.*, 30:421–423, 1969.

[71] D. Quéré and E. Archer. The trail of the drops. *Europhys. Lett.*, 24(9):761–766, 1993.

[72] John A. Dean. *Lange's Handbook of Chemistry*. McGraw-Hill, Inc., New York, NY, 14th edition, 1992.

[73] David R. Lide, editor. *CRC Handbook of Chemistry and Physics*. CRC Press, Boca Raton, FL, 75th edition, 1995.

Biography

Full name: Michael George Pollack
Place of birth: Columbia, South Carolina
Date of birth: February 1, 1973

Schools attended:

- Purdue University, West Lafayette, Indiana, BSEE, May 1994
- Duke University, Durham, North Carolina, MS, December 1998
- Duke University, Durham, North Carolina, PhD, May 2001

Publications:

- M.G. Pollack, R.B. Fair and A.D. Shenderov. Electrowetting-based actuation of liquid droplets for microfluidic applications. *Applied Physics Letters*, 77, pp. 1725–1726, 2000.
- M.G. Pollack. Design, Fabrication and Analysis of a Micromachined Ultrasonic Transducer. Master's Thesis, Duke University, Department of Electrical Engineering, 1998.
- R.B. Fair, M.G. Pollack and V.K. Pamula. MEMS devices for detecting the presence of explosive materials residues in minefields. *Proceedings of SPIE*, 3392, pp. 409-417, 1998.
- R.B. Fair, V.K. Pamula and M.G. Pollack. MEMS trace particle, vapor and ultrasound sensor. *Proceedings of SPIE*, 3079, pp. 671-679, 1997.
- J. Zhang, M.G. Pollack and M. Lieberman. Changes in potassium conductance during hyposmotic swelling of cultured chick heart myocytes. In *Potassium Channels in Normal and Pathological Conditions*. J Vereecke (ed.), Leuven Press, pp. 288–291, 1995.